



UNIVERSITAT POLITÈCNICA
DE CATALUNYA
BARCELONATECH



MASTER THESIS

Atmospheric turbulence profile modeling for satellite-ground laser communication

Lucien Canuet

SUPERVISED BY

Florian Moll, M. Sc.

**Universitat Politècnica de Catalunya
Master in Aerospace Science & Technology**

July 2014

This Page Intentionally Left Blank

Atmospheric turbulence profile modeling for satellite-ground laser communication

BY
Lucien Canuet

DIPLOMA THESIS FOR DEGREE
Master in Aerospace Science and Technology

AT
Universitat Politècnica de Catalunya

SUPERVISED BY:
Florian Moll, M. Sc.
*Deutsches Zentrum für Luft- und Raumfahrt
Institute of Communications and Navigation*

This Page Intentionally Left Blank

ABSTRACT

Profiles of the index of refraction structure parameter (C_n^2), as well as inner and outer scales of turbulence, are of high importance to estimate and predict the channel behavior characterizing satellite to ground optical links. The C_n^2 Hufnagel-Valley model is up to date the most commonly used one due to its simplicity and relative accuracy. However, it can be quite inadequate especially for ground station sites that are situated at important heights above mean sea level. Thus, it seems legitimate to search for a better model that suits the characteristic demands of the satellite to ground link scenario. The work undertaken during this thesis was further motivated by the fact that for the design of a particular communication link, a good understanding of the propagation channel is necessary. Therefore the study presented in this manuscript aimed to identify the status-quo of atmospheric turbulence modeling (structure parameter constant, inner and outer scale profiles) options, by conducting a bibliographic work as extensive as possible and, by assessing with respect to realism, applicability, advantages and drawbacks (especially by the calculation of particular channel parameters) the models referenced.

This Page Intentionally Left Blank

Contents

GENERAL INTRODUCTION	6
1 FREE SPACE OPTICAL COMMUNICATIONS AND THE IMPACT OF THE ATMOSPHERE	8
1.1 Introduction	8
1.2 Optical transmission through the atmosphere	9
1.2.1 The atmosphere	9
1.2.2 Atmospheric Effects	10
1.2.2.1 Absorption	10
1.2.2.2 Scattering	10
1.2.2.3 Refraction	10
1.2.3 Atmospheric Optical Turbulence	11
1.2.3.1 Turbulent energy flow and Kolmogorov theory	11
1.2.3.2 Statistical description of atmospheric turbulence	11
1.2.4 Propagation of optical waves in the atmosphere	14
1.2.4.1 Statistical treatment	14
1.2.4.1.1 Reduced wave equation or Method of analysis	14
1.2.4.1.2 Rytov approximation	14
1.2.4.2 Scintillation Theory	15
1.2.4.3 Application to downlinks (satellite-to-ground)	16
1.2.5 C_n^2 general characteristics	17
1.2.5.1 C_n^2 in the boundary layer	17
1.2.5.2 C_n^2 in the free atmosphere	20
2 INDEX OF REFRACTION STRUCTURE CONSTANT C_n^2 AND CHARACTERISTIC SCALES MODELS	22
2.1 Introduction	22
2.2 Parametric Models	23
2.2.1 Hufnagel-Valley model [1, 2, 3]	23
2.2.2 HAP (Hufnagel/Andrews/Phillips) [4, 5, 6, 7, 8]	26
2.2.3 ARL (US Army Research Lab) Model [4]	30
2.2.3.1 Surface Layer	31
2.2.3.2 Boundary Layer	34
2.2.3.3 Troposphere	35
2.2.3.4 Nighttime conditions	36
2.2.3.5 Final profile	37

2.2.4	Aeronomy Laboratory Model (NOAA) [9, 10]	38
2.2.5	AFGL Radiosonde Model [11]	40
2.2.6	PAMELA [12, 13, 14].....	42
2.2.7	Sadot and Kopeika Model [15, 16].....	43
2.3	Non-Parametric Models	46
2.3.1	H-V 5/7.....	46
2.3.2	H-V Night [17]	46
2.3.3	Greenwood [18]	47
2.3.4	Gurvich [19, 20]	47
2.3.5	Submarine Laser Communications Day [21]	48
2.3.6	AFGL AMOS (Air Force's Maui Optical Station) model [21].....	48
2.3.7	CLEAR (Critical Laser Enhancing Atmospheric Research) model [22]	49
2.4	Characteristic Scales Models	53
2.4.1	Inner-scale Models	53
2.4.2	Outer-scale Models.....	55
2.4.3	Characteristic scales determined from scintillation measurements (using the HAP model).....	58
2.5	Conclusion - Selected Models	59
3	SELECTED MODELS - TESTS AND DISCUSSION	61
3.1	HAP computations	61
3.2	ARL computations	65
3.3	Comparison to Radiosondes Data - Izana Observatory	70
3.4	Comparison to the Results of the Optical Downlink Experiment KIODO ..	73
3.5	HAP Model - A functional implementation.....	75
3.5.1	Overview	75
3.5.2	Ground-level C_n^2 Estimation	76
3.5.3	Random background turbulence estimation (HAP).....	76
	CONCLUSION	79
	BIBLIOGRAPHY	80

This Page Intentionally Left Blank

List of Figures

1.1	Characteristic temperature profile in the atmosphere	9
1.2	Spectral models of refractive-index fluctuations. Taken from [23]	13
1.3	Canonical development of the boundary layer over a diurnal period	18
1.4	Fifteen-minute average C_n^2 measurements and standard deviations plotted for a 24-h period. The data derive from measurements on a tower 9 m above the desert floor under cloudless conditions. Taken from [24]	19
1.5	Thermosonde profiles of C_n^2 and wind speed measured at night during a jet-stream passage in New Mexico. Taken from [21]	20
2.1	Hufnagel-Valley profiles-Influence of input parameters	25
2.2	Power-law parameter p evolution as a function of temporal hours	27
2.3	Three HAP profiles at different time of the day (a); Three HAP profiles with different reference heights of the ground ASL	28
2.4	HV and HAP models comparison	30
2.5	Block diagram - L_{Ob} iterative process	33
2.6	Depth of the daytime boundary layer (convective mixed layer)	35
2.7	ARL profiles for daytime (blue) and nighttime (green) conditions	37
2.8	(a) NOAA (or VanZandt) model and data comparison; (b) Hufnagel model and data comparison. Taken from [11]	39
2.9	Taken from [11]. Method for assigning S_{raw} to $\langle L^{4/3} \rangle$. Uses weighted average Eq. 2.43	40
2.10	AFGL Radiosonde model and data comparison. Taken from [11]	42
2.11	Non-parametric C_n^2 profiles	50
2.12	L_0 profile determined by Beland and Brown	55
2.13	L_0 profiles determined by Coulman et. al. from measurements performed in France-USA and Chile	57
3.1	Effect of the background random turbulence parameter M on the HAP profile; Three HAP profiles at different time of the day (b)	62
3.2	Fried parameters computed using the HAP profiles corresponding to different cases of (a) input parameter M and (b) input parameter p	63
3.3	Scintillation indices computed using the HAP profiles corresponding to different cases of (a) input parameter M and (b) input parameter p	64
3.4	Effect on the ARL profile of the variation of its input parameter; (a) Ground $C_n^2(h_r)$ variations; (b) Air temperature at h_r variations; (c) Average wind velocity at h_r variations	66

3.5	Fried parameters computed using the ARL profiles corresponding to different cases of: (a) Different Ground $C_n^2(h_r)$ values; (b) Different air temperature at h_r values ;(c) Different average wind velocity at h_r values	68
3.6	Scintillation indices computed using the ARL profiles corresponding to different cases of: (a) Different Ground $C_n^2(h_r)$ values; (b) Different air temperature at h_r values ;(c) Different average wind velocity at h_r values	69
3.7	Comparison of the HAP profile (in blue) and HV profile (in green) to the experimental data obtained from radiosonde measurements at Izana in 1975 (in red)	71
3.8	Fried parameters (a) and scintillation indices (b) computed using the HAP and HV profile corresponding to figure 3.7 and compared to that of the Izana experimental profile	72
3.9	Fried parameters (a) and scintillation indices (b) measured during the four trials (KT2, KT3, KT4, KT7) of the KIODO campaign and compared to the ones obtained from the HAP (in blue) and the HV (in green) models	74
3.10	Overview diagram of potential practical implementation of the HAP model .	75
3.11	Monthly distribution of the random background turbulence parameter M obtained from a LMS fit of the HAP model to radiosonde data gathered over one year. Daytime data (12Z launches).	77

This Page Intentionally Left Blank

List of Tables

2.1	Temporal hour weight function (S-K model)	45
2.2	Regression coefficient values (S-K model)	45
2.3	Regression coefficient values (AFGL AMOS model)	49
2.4	C_n^2 profile models synthesis	52
2.5	Inner-scale expressions for spherical and plane waves	54
3.1	Overview of the downlink parameters of the KIODO campaign	73

This Page Intentionally Left Blank

GENERAL INTRODUCTION

The major limitation of free-space laser communications' performances is due to atmospheric turbulences. Free-space optical channels are characterized by a set of different parameters such as the scintillation index, the Rytov variance, the Fried parameter etc. These parameters stem from the particular atmospheric turbulences model chosen. These latter produce random temperature variations of the air which in turn induce random fluctuations of its refractive index. In order to design reliable ground-to-satellite optical communications links, vertical profiles modelings of the strength of refractive turbulences, i.e. the so-called C_n^2 (in $m^{-\frac{2}{3}}$) structure parameter are needed.

Several of these models yet exist and depend on several factors and approximations (average profile, site dependant profile, night or daytime etc.). In the framework of this thesis, a bibliographic study identified the status-quo of atmospheric turbulence modeling (structure parameter and inner and outer scale profiles) options. The models were tested and assessed with respect to realism, applicability, advantages and drawbacks by calculation of particular channel parameters (scintillation index and Fried parameter).

Experimental data obtained from measurments campaigns at DLR in Oberpfaffenhofen (channel parameters measurements) and at Izana's Observatory (radiosonde data) were used to infer the permformance of models selected during the literature research. The discussion that stemed from this assesment highlighted one particlar model.

The first chapter of this manuscript sets the mathematical basis and tools needed to comprehend the importance of selecting the best suited profiles of refractive index structure constant. After a short description of some general qualitative effects encountered by a beam propagating through the atmosphere, optical turbulence theory is introduced. More precisely, the statistical derivation of two channel parameters of interest that are the Fried parameter and the scintillation index is presented. Finally, the description of general features in the behavior of C_n^2 profiles, identified thanks to past studies and measurements, is given at the end of this chapter.

The second chapter deals with the C_n^2 profiles models strictly speaking. It presents the

results obtained from the bibliographic work. It contains as well the description of the characteristics scales of turbulence (inner scale l_0 and outer scale L_0) profiles models and measurements methods currently available. In the conclusion of this chapter, a first assessment is made concerning the usefulness of all the models referenced. On the basis of this discussion, two models are pre-selected for further assesment and testings.

The third chapter presents the results of said testings. In a first step, the input parameters of both models are varied with the aim to determine their advantages, drawbacks and limitations in light of their realism and practical applicability. The channel parameters aforementioned are computed and compared to experimental data. A single model arised from these tests and discussion as the most relevant one to be used in the framework of satellite to ground optical links. Fianlly, a the end of this chapter, a description of its functional implementation options is given.

Chapter 1

FREE SPACE OPTICAL COMMUNICATIONS AND THE IMPACT OF THE ATMOSPHERE

1.1 Introduction

Optical turbulence, induced by random variations in the refractive index of the Earth's atmosphere, are responsible for random fluctuations in the signal carrying laser beam intensity (irradiance) called scintillations. It causes other effects as well, such as beam spreading beyond the spreading predicted by diffraction and random motion of the beam centroid about the receiver, that result in random signal losses at the receiver and thus increases the system bit error rates due to signal fading. It is therefore of primary importance for who intends to correctly estimate the real performances of a ground-to-satellite optical communication system to work with the most appropriate model of optical turbulence.

Turbulent winds in the Earth's atmosphere mix the always present vertical moisture and temperature gradients caused by the Sun's heating of the Earth's surface. This creates irregularities in the refractive index of the atmosphere in the form of eddies, or cells, called optical turbules. A way to characterize such fluctuations of the atmosphere's refractive index is done through the modeling of the index of refraction structure constant C_n^2 . For ground-to-satellite channels, vertical profiles of C_n^2 must be determined to characterize various "regimes" of turbulence in a seamless manner, starting at the ground and continuing into the upper troposphere. While various standard profiles exist nowadays, most of these were developed with particular goals in mind and most of the time for particular geographical sites and atmospheric conditions and can therefore create problems if one applies the model to new areas.

This chapter constitutes an introduction to optical transmission through the atmosphere. After a qualitative description of the atmosphere and its effects on the propagation of electromagnetic radiation, the mathematical basis for the derivation of the channel parameters relevant to the characterisation of an optical downlink are set. General characteristics of the refractive index structure constant, taken into account in the selection of the most suitable C_n^2 profile model in the following chapter, are exposed as well.

1.2 Optical transmission through the atmosphere

1.2.1 The atmosphere

The atmosphere extends to several hundred kilometers above Earth's surface. Four primary subdivisions of the atmosphere are usually done based on the average temperature variations with altitude. The troposphere extends from ground to roughly 11 km. It contains 75% of earth's atmospheric mass. Maximum air temperature occurs near the surface of the earth, but decreases with altitude to 55°C at its top. In the stratosphere the air temperature increases with altitude because the ozone gas absorbs ultraviolet sunlight, thereby creating heat energy. Thus this layer protects life from harmful radiations. The mesosphere constitutes the layer where temperature decreases down to 90°C, the coldest in the atmosphere. Finally, above 90km, in the thermosphere which is the outermost region of the atmosphere, air temperature increases quite strongly. Moreover, these layers are separated by three isothermal boundaries that are the tropopause, the stratopause and mesopause.

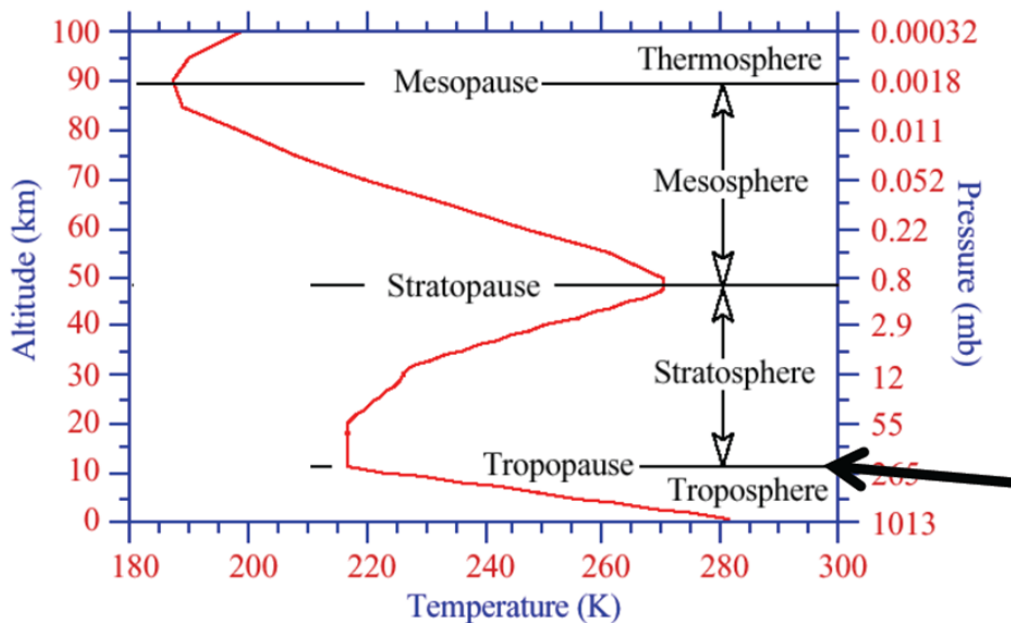


Figure 1.1: Characteristic temperature profile in the atmosphere

Because of the mass of the atmosphere is concentrated in the lower layers, atmospheric refractive index profiles relevant to optical communication from a satellite to the ground do not extend at heights greater than roughly 25-30km. Therefore the common features found among these models are the effects related to the decreasing temperature in the troposphere and the strong wind shears found at the level of the tropopause.

1.2.2 Atmospheric Effects

The propagation of electromagnetic radiation through the atmosphere is affected by several atmospheric factors such as rain, snow, fog, haze or pollution for instance. More precisely, three primary phenomena affect optical wave propagation: absorption, scattering and refraction. Absorption and scattering by the constituent gases and particulates of the atmosphere are wavelength dependent and give rise primarily to attenuation of an optical wave. Refraction effects, i.e. fluctuations in the index of refraction, lead to irradiance fluctuations, beam spreading, and loss of spatial coherence of the optical wave propagated.

1.2.2.1 Absorption

Absorption occurs when a photon of radiation is absorbed by a gaseous molecule of the atmosphere that converts the photon into the molecule's kinetic energy. Therefore this process depends strongly on the wavelength of the incoming photons. For example, absorption by O_2 and O_3 molecules eliminates propagation of radiation at wavelengths below $0.2 \mu m$, but there is very little absorption at the visible wavelengths (0.4 to $0.7 \mu m$). Water vapor carbon dioxide present in the atmosphere affects greatly as well the propagation of radiation and determine for instance the well-known infrared atmospheric window.

1.2.2.2 Scattering

Scattering of electromagnetic waves in the visible and IR wavelengths occurs when the radiation propagates through certain air molecules and particles. Light scattering is strongly wavelength dependent, but there is no loss of energy like in absorption. Two types of scattering processes exist, determined by the physical size of the scatterers. Namely, Rayleigh scattering (or molecular scattering) caused by air molecules and haze that are small in comparison with the wavelength of the radiation. It applies only to very clear atmosphere and is negligible at wavelengths greater than roughly $3 \mu m$. Mie scattering (or aerosol scattering) by particles comparable in size to the radiation wavelength. Scattering losses decrease rapidly with increasing wavelength, eventually approaching the Rayleigh scattering case.

1.2.2.3 Refraction

The atmospheric index of refraction is a function of pressure, temperature, and frequency. Its random variations, created by wind shears in the presence of a temperature gradient, induce optical atmospheric turbulence that will greatly affect the propagation of an optical wave. These deleterious effects have important consequences on applications such as astronomical imaging, optical communications, remote sensing, and laser radar for example, and need to be characterized in order to correctly assess system performance. The next sections intend to introduce the fundamental concepts and parameters characterizing

the behavior of optical turbulence and the basis of most propagation theories in a random medium.

1.2.3 Atmospheric Optical Turbulence

1.2.3.1 Turbulent energy flow and Kolmogorov theory

Atmospheric turbulence is produced by the kinetic energy induced by the movement of air masses, a purely meteorological phenomenon (convection or wind shear). This energy, in a first step, allows for the creation of eddies with characteristic sizes ranging from a few hundreds of meters to a few tens of meters (called the turbulence outer scale or L_0). It is then transmitted to eddies of decreasing sizes until it is dissipated when reaching the viscosity regime i.e. when reaching characteristic sizes of the order of the millimeter (called the turbulence inner scale or l_0). This process is known in the literature as the energy cascade theory (due to Richardson [25]). The domain lying between these two characteristic scales is called the inertial domain or sub-range of turbulence and corresponds to the regime where the turbulence is said to be fully developed.

Kolmogorov hypothesis states that during this cascade process the direct influence of larger eddies is lost and smaller eddies tend to have independent properties. In other words the energy cascade process consists of an energy input region, inertial sub-range, and energy dissipation region. Furthermore, in the inertial range the fluctuations are assumed to be spatially homogeneous and isotropic

It should be noted that in general, turbulent flows in the atmosphere are neither homogeneous nor isotropic but can rather be considered locally as so in small sub-regions of the atmosphere.

1.2.3.2 Statistical description of atmospheric turbulence

The mathematical description of turbulence is approached with the help of statistics. In this regard, for a statistically homogenous medium, the structure function of wind velocity between two observation points, \mathbf{r}_1 and \mathbf{r}_2 , is given in the inertial subrange by:

$$\begin{aligned} D_V(r) &= \langle [V(r_1) - V(r_2)]^2 \rangle \\ &= \langle [V(\mathbf{r}_1 + \mathbf{r}) - V(\mathbf{r}_1)]^2 \rangle = C_V^2 r^{2/3}, \quad l_0 < r < L_0 \end{aligned} \quad (1.1)$$

where $\langle \rangle$ is the mean operator, C_V^2 is defined as the structure constant of wind velocity which indicates the strength level of the turbulence. This statistical treatment of velocity fluctuations have also been applied to temperature and atmospheric refractive index fluctuations. First, the refractive index, n , has to be described in terms of observable atmospheric variables that are the corresponding temperature and pressure. In the optical domain, where the small dependence on optical wavelength can be neglected, it is described by the following relationship:

$$n - 1 \simeq 79 \times 10^{-6} \frac{P}{T} \quad (1.2)$$

where P is the atmospheric pressure in millibars and T is the temperature in Kelvins. Because the statistical description of the random field of turbulence-induced fluctuations in the atmospheric refractive index is similar to that for the related random field of turbulent velocities, an inertial subrange exists bounded above by an outer scale L_0 and below by an inner scale l_0 . Therefore, under the hypothesis of statistically homogenous medium, one can derive the structure function of the refractive index and obtain:

$$D_n(n(\mathbf{r})) = \langle [n(\mathbf{r}_1) - n(\mathbf{r}_1 + \mathbf{r})]^2 \rangle = C_n^2 r^{2/3}, \quad l_0 < r < L_0 \quad (1.3)$$

where the term C_n^2 is the so called index of refraction structure parameter which indicates the strength of the turbulence. Its dimensions are measured in $m^{-2/3}$.

The mathematical tool used in the characterisation of random and ergodic processes is the power spectrum. It is a frequency domain representation, or spectral decomposition, of the temporal correlations of a given random process or field. If one neglects variations in humidity and pressure, the functional form of the spatial power spectrum of refractive-index fluctuations is the same as that for temperature and, further, that temperature fluctuations obey the same spectral laws as velocity fluctuations. The associated power spectral density for refractive-index fluctuations over the inertial subrange is defined by

$$\Phi_n(\kappa) = 0.033 C_n^2 \kappa^{-11/3}, \quad 1/L_0 \ll \kappa \ll 1/l_0 \quad (1.4)$$

This equation defines the Kolmogorov power-law spectrum. It is theoretically valid only over the inertial subrange but can be extended to all wave numbers if one assumes an infinite outer scale ($L_0 = \infty$) and a negligibly small inner scale ($l_0 = 0$). Therefore other models of the spectrum for refractive-index fluctuations are required in some calculations where the effects associated with realistic inner and outer scales cannot be neglected. For instance, when extending the power law spectrum in Eq. 1.4 into the dissipation range $\kappa > 1/l_0$, one needs to introduce a function that essentially truncates the spectrum at high wave numbers. The resulting, spectrum known as the Tatarskii spectrum is written as:

$$\Phi_n(\kappa) = 0.033 C_n^2 \kappa^{-11/3} \exp\left(-\frac{\kappa^2}{\kappa_m^2}\right), \quad \kappa \gg 1/L_0, \quad \kappa_m = 5.92/l_0 \quad (1.5)$$

As for the Kolmogorov spectrum, this model is still limited by a singularity at $\kappa = 0$ and it is anisotropic for $\kappa < 1/L_0$ where its form is unknown. Modifications are usually considered in practice so that both spectrums are also finite and isotropic for wave numbers $\kappa < 1/L_0$. These modifications lead to the definitions of the Karman spectrum, the modified von Karman spectrum and the exponential spectrum. Because the derivation in the next sections of the channel parameters of interest are done in the literature considering the simplest case of a Kolmogorov spectrum without lack of generality, it seems superfluous to give here a detailed description of each one of the spectra. Figure 1.2 presents the evolution of three different spectra over a range of wave numbers showing the outer scale and inner scale wave numbers that identify the boundaries of the inertial subrange. The Kolmogorov spectrum, the von Karman spectrum and the modified atmospheric spectrum are illustrated. The later one, was developed by Andrews [26] and includes an outer scale parameter. It is introduced here as it will be used in section 2.4.3 of chapter 2 as part of a method to determine characteristic scales using scintillation measurements. Its

main enhancement resides in the modeling of the rise (or "bump") at high wave numbers near $1/l_0$ that appears in temperature spectral data (followed in reality by the refractive index spectral law since it obeys the same law) as shown in [27, 28]. This bump can have important consequences on various aspects of optical wave propagation through the atmosphere, particularly in regards to scintillation.

$$\Phi_n(\kappa) = 0.33C_n^2\kappa^{-11/3} \left[1 + 1.802 \left(\frac{\kappa}{\kappa_l} \right) - 0.254 \left(\frac{\kappa}{\kappa_l} \right)^{7/6} \right] \left[1 - e^{-\frac{\kappa^2}{\kappa_0^2}} \right] e^{-\frac{\kappa^2}{\kappa_l^2}} \quad (1.6)$$

with

$$0 \leq \kappa < \infty, \quad \kappa_l = \frac{3.3}{l_0}, \quad \kappa_0 = \frac{8\pi}{L_0} \text{ or } \frac{2\pi}{L_0}$$

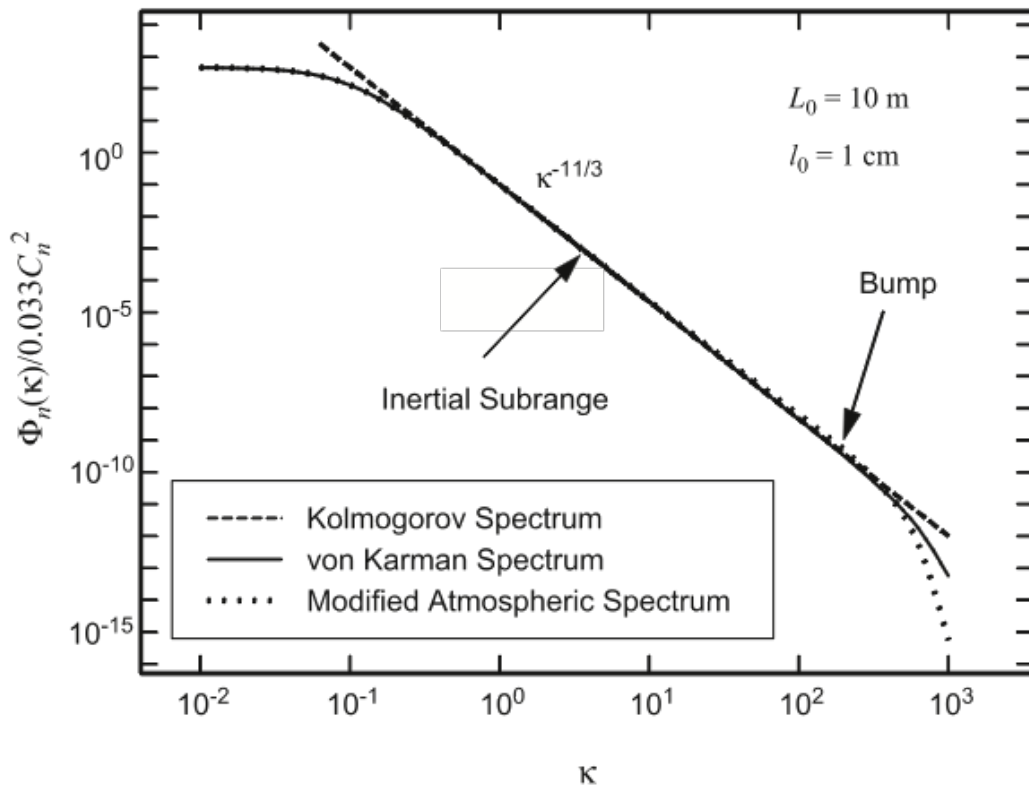


Figure 1.2: Spectral models of refractive-index fluctuations. Taken from [23]

One can notice that a nonzero inner scale reduces values of the spectrum at high wave numbers ($\kappa > l_0$) over that predicted by the Kolmogorov spectrum. At low wave numbers ($\kappa < 1/L_0$), a similar reduction in values of the spectrum are caused by the presence of a finite outer scale.

1.2.4 Propagation of optical waves in the atmosphere

1.2.4.1 Statistical treatment

1.2.4.1.1 Reduced wave equation or Method of analysis

Optical wave propagation through a random medium characterized by small fluctuations in the refractive index has been the subject of extensive theoretical investigations for many years. Random fluctuations in the index of refraction cause spreading of the beam beyond that due to pure diffraction, random wandering of the instantaneous beam center (beam wander), loss of spatial coherence, and random fluctuations in the irradiance and phase. Scale sizes larger than the beam diameter cause beam wander, whereas scale sizes on the order of the first Fresnel zone are the primary cause of irradiance fluctuations (scintillations).

In most applications related to free space optical propagation, one characterizes the received wave in terms of statistical moments of the random optical field $U(\mathbf{r}, L)$, where L is the propagation distance along the positive z-axis from the emitting aperture of the transmitter to the receiver and \mathbf{r} is a vector in the receiver plane transverse to the propagation axis. When neglecting polarization effects, one can show that the propagation of this random optical field obeys the following reduced wave equation:

$$\nabla^2 U(\mathbf{r}) + k^2 n \mathbf{r}^2 U \mathbf{r} = 0 \quad (1.7)$$

where n denotes the random index of refraction. One of the most common and simple way to solve this equation is to consider the Rytov approximation (a classical perturbation method). More complex and sophisticated methods exist but are in general more mathematically challenging. Moreover in the case of a satellite-to-ground downlink considered in the present work, the optical wave can be described as a plane wave. This assumption further simplifies the propagation modeling.

1.2.4.1.2 Rytov approximation

The Rytov approximation consists in writing the field propagated at a distance L from the transmitter as:

$$U(\mathbf{r}, L) = U_0(\mathbf{r}, L) e^{\Psi_1(\mathbf{r}, L) + \Psi_2(\mathbf{r}, L) + \dots} \quad (1.8)$$

where $U_0(\mathbf{r}, L)$ is the wave at the receiver and $\Psi(\mathbf{r}, L)$ is the total complex phase perturbation of the field due to random inhomogeneties along the propagation path. Then its first statistical moment corresponds to the mean field which describes the coherent part of the optical signal:

$$\langle U(\mathbf{r}, L) \rangle = U_0(\mathbf{r}, L) \langle e^{\Psi(\mathbf{r}, L)} \rangle \quad (1.9)$$

The second-order moment, also called the mutual coherence function (MCF), is defined by the average:

$$\Gamma_2(\mathbf{r}_1, \mathbf{r}_2, L) = \langle U(\mathbf{r}_1, L) U^*(\mathbf{r}_2, L) \rangle \quad (1.10)$$

Under the assumption of weak fluctuations and considering an incident plane wave (i.e. an infinite wave model with no phase curvature), one can show that Eq. 1.10 yields:

$$\Gamma_2(\rho, L) = \exp \left\{ -4\pi^2 k^2 L \int_0^\infty \kappa \Phi_n(\kappa) [1 - J_0(\kappa \rho)] d\kappa \right\} \quad (1.11)$$

Moreover, if a simple Kolmogorov turbulence spectrum model is considered the MCF is given by:

$$\begin{aligned}\Gamma_2(\rho, L) &= \exp \left[- \left(\frac{1.22(\sigma_R^2)^{6/5} k \rho^2}{L} \right)^{5/6} \right] \\ &= \exp(-1.46 C_n^2 k^2 L \rho^{5/3}), \quad l_0 \ll \rho \ll L_0\end{aligned}\quad (1.12)$$

The MCF usefulness resides in its ability to predict atmospherically induced beam spreading through the mean irradiance. However, it can also be used to predict the spatial coherence radius at the receiver plane since that

$$\Gamma_2(\rho, L) = \exp \left[-\frac{1}{2} D(\rho, L) \right] \quad (1.13)$$

where $D(\rho, L)$, the wave structure function (WSF) is given by:

$$D(\rho, L) = 2.91 k^2 \rho^{5/3} \int_0^L C_n^2(h) dh, \quad l_0 \ll \rho_0 \ll L_0 \quad (1.14)$$

The spatial coherence radius, noted ρ_0 , is defined as that separation distance at which the normalized MCF reduces to 1/e:

$$\rho_0 = \left[1.46 k^2 \int_0^L C_n^2(h) dh \right]^{-3/5}, \quad l_0 \ll \rho_0 \ll L_0 \quad (1.15)$$

The parameter that is more frequently used in the astronomical community than the spatial coherence radius is the so called Fried parameter simply written as:

$$r_0 = 2.1 \rho_0 \quad (1.16)$$

It describes the largest effective telescope diameter for image resolution i.e. the imaging resolution of telescopes with apertures much larger than r_0 will be limited by the effects induced by the turbulent atmosphere, preventing the instruments from approaching the diffraction limit. In the framework of an optical communication system, the Fried parameter defines also an upper bound for aperture diameter in maximizing the normalized signal-to-noise ratio in a coherent detection system for which phase fluctuations play a more important role than in direct detection systems which are more sensitive to scintillation effects (i.e. amplitude fluctuations of the incoming beam).

1.2.4.2 Scintillation Theory

To derive expressions for the scintillation index one needs to consider fourth-order statistical quantities of the field. A general expression of the fourth-order cross-coherence function for a beam that has propagated a distance L is given by:

$$\Gamma_4(\mathbf{r}_1, \mathbf{r}_2, \mathbf{r}_3, \mathbf{r}_4, L) = \langle U(\mathbf{r}_1, L) U^*(\mathbf{r}_2, L) U(\mathbf{r}_3, L) U^*(\mathbf{r}_4, L) \rangle \quad (1.17)$$

This expression allows one to access to the fourth-order coherence function and thus the second moment of the irradiance by setting $\mathbf{r}_1 = \mathbf{r}_2 = \mathbf{r}_3 = \mathbf{r}_4 = \mathbf{r}$:

$$\langle I^2(\mathbf{r}, L) \rangle = \Gamma_4(\mathbf{r}, \mathbf{r}, \mathbf{r}, \mathbf{r}, L) \quad (1.18)$$

To compute the scintillation index one needs first to evaluate the covariance function of irradiance, a two-point statistic depending on Γ_4 and Γ_2 , defined as:

$$B_I(\mathbf{r}_1, \mathbf{r}_2, L) = \frac{\Gamma_4(\mathbf{r}_1, \mathbf{r}_1, \mathbf{r}_2, \mathbf{r}_2, L)}{\Gamma_2(\mathbf{r}_1, \mathbf{r}_1, L)\Gamma_2(\mathbf{r}_2, \mathbf{r}_2, L)} - 1 \quad (1.19)$$

The scintillation index is simply the covariance function of irradiance when $\mathbf{r}_1 = \mathbf{r}_2 = \mathbf{r}$:

$$\sigma_I^2(\mathbf{r}, L) = \frac{\langle I^2(\mathbf{r}, L) \rangle}{\langle I(\mathbf{r}, L) \rangle^2} - 1 \quad (1.20)$$

One can show that in the case of isotropic and homogeneous turbulence, the scintillation index of an infinite plane wave propagating along a slant path (i.e. considering a varying index-of-refraction structure parameter) is given by:

$$\begin{aligned} \sigma_I^2(L) &= 8\pi^2 k^2 \int_0^L \int_0^\infty \kappa \Phi_n(\kappa, h) \left[1 - \cos \frac{L\kappa^2(1-h/L)}{k} \right] d\kappa dh \\ &= 2.25k^{7/6} L^{5/6} \int_0^L C_n^2(h)(1-h/L)^{5/6} dh \end{aligned} \quad (1.21)$$

1.2.4.3 Application to downlinks (satellite-to-ground)

In the case of weak irradiance fluctuation regimes (for which the Rytov method can be used) and a plane wave, the scintillation index can be deduced from Eq. 1.21:

$$\sigma_I^2(L) = \sigma_r^2 = 2.25k^{7/6} \sec^{11/6}(\eta) \int_{h_0}^H C_n^2(h)(h-h_0)^{5/6} dh \quad (1.22)$$

where h_0 is the height above ground level of the downlink receiver, $H = h_0 + L \cos(\eta)$ is the satellite altitude, and η is the zenith angle. For larger zenith angles the downlink scintillation index can exceed the limitations of weak fluctuation theory because the propagation path of the beam through the atmosphere is increased. In that case, the scintillation index is given by:

$$\sigma_I^2(L) = \exp \left[\frac{0.49\sigma_R^2}{(1 + 1.11\sigma_R^{12/5})^{7/6}} + \frac{0.51\sigma_R^2}{(1 + 0.69\sigma_r^{12/5})^{5/6}} \right] - 1 \quad (1.23)$$

where σ_R^2 is given by Eq. 1.22

Because of the different weighting functions involved, $r_0(h)$ will tend to be affected by the turbulence closest to it. On the other hand, systems affected most by scintillation will be most impacted by turbulence near the center of the path.

1.2.5 C_n^2 general characteristics

When discussing the behavior of C_n^2 evolution with altitude it is convenient to make the distinction between the atmospheric boundary layer (ABL) and the free atmosphere. The former is the region where the atmospheric dynamics are dominated by the interaction and heat exchange with the earth's surface. In the latter the dynamics are more complicated and turbulence depends on synoptic meteorology, wind shear, and gravity waves. The existing models of C_n^2 profile can describe either layer or include both.

1.2.5.1 C_n^2 in the boundary layer

The boundary layer C_n^2 profiles show a strong temporal dependence. In the daytime, the heating of the surface results in convective instability and gives rise to thermal plumes and strong optical turbulence. The daytime boundary layer extends to a capping inversion layer in temperature [21, 29], typically 1 or 2 km above the surface by mid-afternoon in mid-latitudes regions and over land. It can be further partitioned, into the surface layer (10-20m), the mixed layer (often used synonymously with the boundary layer itself in most of the literature), and the interfacial layer. The surface layer consists of the first few meters above the ground and its properties are determined by the air-to-ground differences in atmospheric parameters. The mixed layer consists of the region from the surface layer up to the inter-facial layer where strong vertical mixing is produced by convection. The inter-facial layer is the vicinity of the capping inversion that separates the boundary layer from the free atmosphere. The evolution of the C_n^2 parameter in the boundary layer is the most difficult to model as the behavior of this layer is extremely site and time dependant. Nevertheless a canonical development of the boundary layer over a diurnal period that includes the general characteristics described so far can be derived. It is represented in figure 1.3.

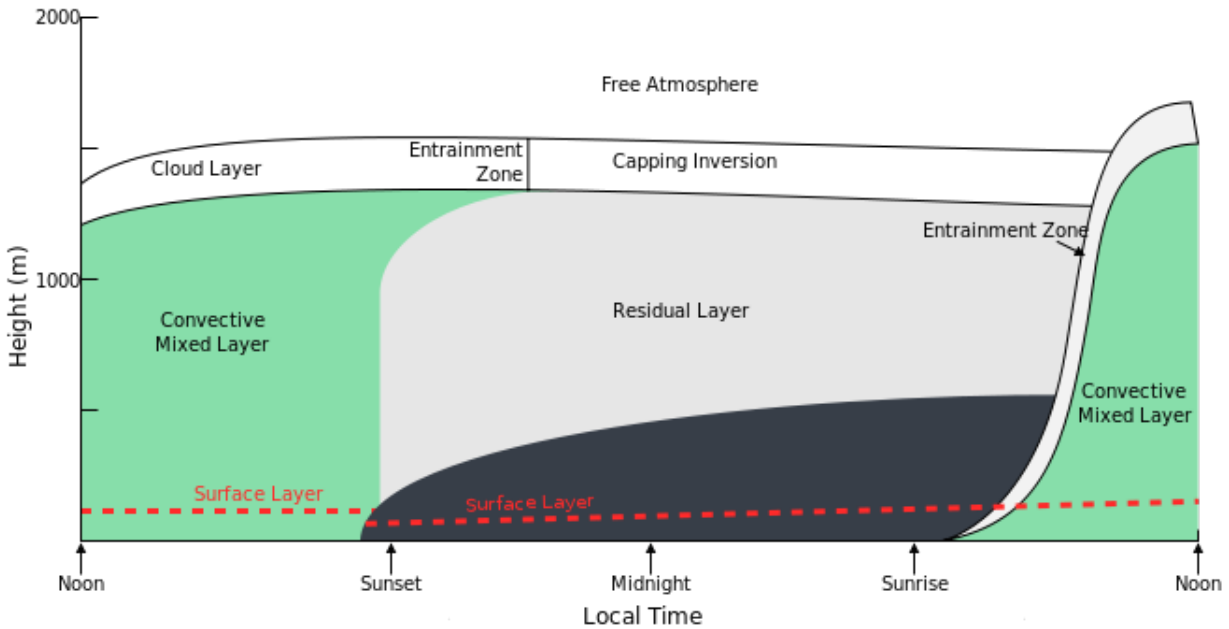


Figure 1.3: Canonical development of the boundary layer over a diurnal period

Figure 1.4 shows an example of the C_n^2 temporal dependence in the surface layer (near the ground). The fifteen-minute average values of C_n^2 are shown for a cloudless day over dry soil at a height of 9 m. The data show a well-established diurnal cycle, with a well-behaved peak in the daytime, near constant on average at night, and minima near sunrise and sunset. These features are characteristic of many measurements made in moderate climatic conditions. Solar irradiance is responsible for the daytime behavior: the dominance of convection is highlighted, rising and falling along with the solar flux through the day. The neutral events correspond to the most stable atmospheric conditions i.e. when the soil and air temperature are the same. They occur approximately one-and-a-half hours after sunrise and one hour before sunset. The residual optical turbulence during these events is due to mechanical turbulence and incomplete mixing. The nighttime fluctuations of C_n^2 occur around a mean value. They are much more variable and more difficult to characterize from site to site.

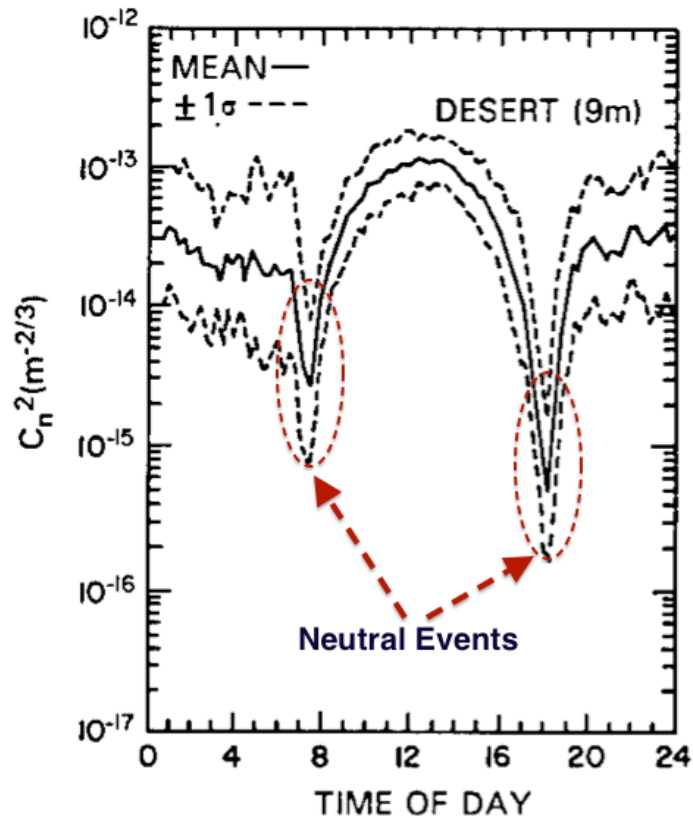


Figure 1.4: Fifteen-minute average C_n^2 measurements and standard deviations plotted for a 24-h period. The data derive from measurements on a tower 9 m above the desert floor under cloudless conditions. Taken from [24]

In the daytime, optical turbulence is strongest near the ground. Typical values of C_n^2 are found to be around $10^{-13} m^{-2/3}$. It decays in average with altitude with a $-4/3$ exponent up to the capping inversion layer (few km height) where an abrupt increase can be measured since it is a region of strong temperature gradients. This general behavior depicts an evolution that occurs when atmospheric conditions lead to situations where convection dominates the boundary layer dynamics. When there are strong winds or clouds or in early morning or late afternoon, optical turbulence profiles deviate from this pattern.

At night, the surface cools by radiation and is colder than the air, and this is usually denoted by the presence of a strong surface temperature inversion. This inversion can range from tens to hundreds of meters thick. Therefore nighttime data are more variable. There is usually no discernible falloff rate and the most dominant characteristic above the surface is the stratification of the optical turbulence.

Moreover, the atmospheric boundary layer depends dramatically on various factors such as the orography of a given site, solar insolation, vegetation, winds, etc. For instance, the boundary layer over a desert can extend to as much 3km above the ground whereas mountaintop locations rise above the boundary layer of the surrounding terrain. Therefore, due to the extreme variability of the atmospheric conditions in the boundary layer (temporal as well as orographic), a generic C_n^2 profile model cannot be developed or ap-

plied without considering specific application cases.

1.2.5.2 C_n^2 in the free atmosphere

The free atmosphere is constituted by the troposphere, the tropopause and the stratosphere. The general feature characterizing the C_n^2 evolution in this layer is the formation of a stratification superimposed on an exponential fall-off with altitude. This stratification induces the fact that large values of C_n^2 occur in narrow layers, of the order of hundreds of meters in thickness. The magnitude of C_n^2 variations in these layers exceeds that of the "background" by more than an order of magnitude. The horizontal extent of these layers and their temporal duration are not well understood. However numerous measurements have been done using mainly balloon-borne instruments. An example of such measurements is given on figure 1.5.

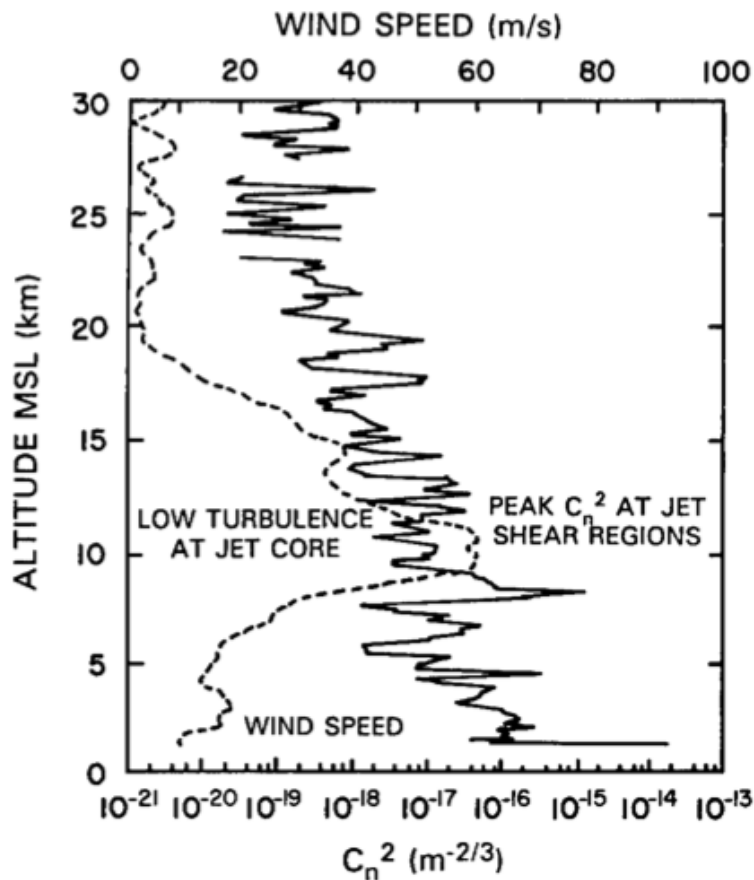


Figure 1.5: Thermosonde profiles of C_n^2 and wind speed measured at night during a jet-stream passage in New Mexico. Taken from [21]

The C_n^2 profiles in this region of the atmosphere are primarily influenced by the synoptic

meteorological conditions. Mainly, strong wind conditions along certain given layers in the free atmosphere can induce strong layers of optical turbulence. For instance, in figure 1.5, the measurements were performed during the passage of a polar-front jet stream. At altitudes corresponding to the edge of the jet stream, peak values of C_n^2 can be observed. Several jet stream measurements have been performed and analysed in [30]. The authors concluded that the jet-stream enhancement may occur in two forms. Either an overall increase of the C_n^2 profile is observed or thick layers of enhanced turbulence can appear. Another characteristic feature of optical turbulence in the free atmosphere layer is the presence of a bulge in the C_n^2 profile at the tropopause level. The temperature lapse rate of the troposphere and stratosphere are different (see figure 1.1). The tropopause is therefore a region of sharp temperature gradients. Hence, an inflection point in trend of the C_n^2 profile is generally present, but can be indiscernible given "extraordinary" conditions such as the passage of jet streams.

Chapter 2

INDEX OF REFRACTION STRUCTURE CONSTANT C_N^2 AND CHARACTERISTIC SCALES MODELS

2.1 Introduction

The refractive index structure parameter C_n^2 is a measure of the intensity of optical turbulence. Models of this parameter exist at many levels of complexity. They can be based upon empirical and/or theoretical developments and be presented under a purely analytical form (closed or not) or a numerical one requiring input parameters.

The refractive index structure parameter depends (among different meteorological variables) on the geographical location, altitude, and time of day. Different locations can have different characteristics of temperature distribution that are reflected on the values assumed by C_n^2 . Below the tropopause, the largest gradients of temperature, associated with the largest values of atmospheric pressure and air density are close to ground, at sea level, where therefore one should expect the largest values of C_n^2 . As the altitude increases the temperature gradient as well as the atmospheric pressure and air density decrease resulting in smaller values of C_n^2 until the tropopause where strong wind shear occur producing an in C_n^2 anew.

Moreover, considering the temperature dynamics during the day closer to the ground, one should expect turbulence to be stronger around noon. Conversely, at sunset and dawn, due to a form of thermal equilibrium along the atmosphere vertical profile, one should expect C_n^2 to have lower values [22, 21, 12, 24].

Whereas C_n^2 along a horizontal path can be considered "constant", slant path implies that it varies due to the different temperature gradient, air pressure, and density along the altitude. Determining the profile of C_n^2 with altitude is a difficult task in the sense that generally, experimental data are not readily available and it is not easy to capture properly its variations measured usually with radiosondes, SCIDAR (SCIntillation Detection And Ranging), SLODAR (SLOpe Detection And Ranging) and SODAR (SONic Detection And Ranging). However, a number of models have been formulated to describe such profiles since the 70s. Most of these initial models (SLC, AFGL CLEAR(s) and AFGL AMOS) [21, 4] were developed for specific places or (micro-)climates complicating their generalisation [21]. They are usually referred as nonparametric models i.e. they depend only on the altitude and represent average profiles (without stratification) that are usually highly site-dependant. Parametric models have been developed in an attempt to include the depen-

dance on site, the stratification (typical profiles show C_n^2 varying in layers of thickness of hundred of meters) as well as meteorological parameters. Moreover, due to different atmospheric dynamical regimes, C_n^2 ranges from $10^{-13}m^{-2/3}$ near the surface to $10^{-20}m^{-2/3}$ in the upper atmosphere. Therefore most of the models developed so far describe either the boundary layer or the free atmosphere, the former being the most difficult to model since its depth is constantly varying and is highly site-dependant (humidity, soil roughness, solar radiation, peculiar wind profile etc.).

This chapter summarizes the bibliographic work related to C_n^2 profiles modeling undertaken during this thesis. The referencing process of most of the existing models, in the best of my knowledge, has been done as extensively as possible. Among them are the most known and common ones such as the famous Hufnagel-Valley model (and its derivatives)[1, 2, 17], the Submarine Laser Communications (SLC) Day model[21] or the Greenwood model[18]. Moreover, less known and more recent models such as for instance the HAP[4, 5, 6, 7, 8] or the PAMELA[13, 14] models are also described.

The first section of this chapter is devoted to parametric models. An application case summary is written for each one of them. The second section describes the non-parametric profiles. The table 2.4 summarizes this bibliographic work by presenting the modeling equations for each profile and the input parameters for the parametric models.

Furthermore, C_n^2 is not the only fundamental parameter of interest when one seeks to adequately evaluate the performances of a ground-to-satellite optical communication system. Characteristic scales of turbulence (inner scale l_0 and outer scale L_0) are also of primary relevance when for instance, evaluating adaptive optics performance and focal-plane statistics since they constitute key parameters for the evaluation of the turbulence spectrum to be used. Therefore the second part of this report is dedicated to provide a synthesis of the models and means of measurement currently available of l_0 and L_0 .

2.2 Parametric Models

Parametric models depend on more than only altitude to describe the evolution of C_n^2 . Of those detailed in the present section, only the Hufnagel-Valley and the HAP models present profiles ranging from ground to the upper atmosphere. The NOAA and AFGL radiosonde models apply to the free atmosphere only but present "high-resolution" profiles since that they are based on thermosonde measurements. The PAMELA and Sado-Kopeika models potentially describe the C_n^2 parameter in the boundary layer only but very accurately. They both rely on a large set of meteorological input data such as air temperature, relative humidity, solar flux, wind speed and direction etc.

2.2.1 Hufnagel-Valley model [1, 2, 3]

Hufnagel proposed in 1974 [2] a heuristic model of the C_n^2 profile based on measurements made by many observers. He found that stellar scintillation measurements were well

correlated with the following factor:

$$v^2 = \left(\frac{1}{15 \times 10^3} \right) \int_{5 \times 10^3}^{20 \times 10^3} v_{wind}^2(h) dh \quad (2.1)$$

where $v_{wind}(h)$ is the wind speed in meters per second at altitude h above sea level. Therefore the physical implication of the Hufnagel model is that the wind velocity controls the strength of the turbulence at high altitude as well as its temporal spectrum through the factor v^2 . Two components constitute the original Hufnagel model. An exponentially decreasing value of C_n^2 through the troposphere with a $1/e$ scale height of 1500m and a peak at the tropopause around 10km, scaled by v^2 . The model has the following form:

$$C_n^2(h) = A \left[2.2 \times 10^{-53} h^{10} \left(\frac{v}{27} \right)^2 e^{-\frac{h}{1000}} + 1 \times 10^{-16} e^{-\frac{h}{1500}} \right] \quad (2.2)$$

The parameter A models the fine structure of the turbulence as a function of height and time and is defined as:

$$A = e^{r(h,t)} \quad (2.3)$$

where r is a Gaussian random variable with zero mean, t is time. Although, turbulence profiles measured by temperature probes show local variations in turbulence strength with a vertical scale size of about 100m, and optical measurements show variations over a time scale of minutes, this fine structure is generally ignored in most of the models. Instead, an average turbulence profile is obtained by setting $A = e \simeq 2.7$.

The Hufnagel model, initially suitable for an altitude ranging from 3 to 24 km, has been augmented by a boundary layer term by Ulrich in 1988. Indeed, below 3km there are large local and diurnal variations of turbulence produced mainly by convection from solar heating. Valley suggested (in 1980) the addition of the term describing such a layer originally in order to satisfy the needs of the defense community for the design of adaptive optics systems that must be able to operate under any conditions. The resulting Hufnagel-Valley (HV) model is described by the following expression where the last exponential term accounts for the boundary layer correction. One might expect an exponential decrease due to the exponential decrease of temperature with height, however this is strictly true only by assuming an isothermal atmosphere.

$$C_n^2(h) = 0.00594(v/27)^2(10^{-5}h)^{10}e^{-\frac{h}{1000}} + 2.7 \times 10^{-16}e^{-\frac{h}{1500}} + Ae^{-\frac{h}{100}} \quad (2.4)$$

where h is in meters, $A = C_n^2(0)$ is a nominal ground-level value of C_n^2 and v is the high altitude rms wind speed (although v is usually taken to be $21m/s$ or $57m/s$ in stronger wind conditions, it can be determined by the following model or other wind profile models)

$$v = \left[\frac{1}{15 \times 10^3} \int_{5 \times 10^3}^{20 \times 10^3} \left(v_s h + v_g + v_T e^{-\left(\frac{h \sin(\alpha) - H_T}{L_T} \right)^2} \right)^2 dh \right]^{1/2} \quad (2.5)$$

where v_s is the beam slew rate, v_g is the ground wind speed, v_T is the wind velocity at the tropopause, α is the zenith angle of observation, H_T is the tropopause height and

L_T is the thickness of the tropopause layer. The popularity of such a model lies on the potential choosing of the two parameters that are v and A thus allowing for variations in high-altitude wind speed and local near-ground turbulence conditions. Therefore it is an attractive model for studies over a large range of geographic locations although it should be kept in mind that the HV model is an empirical fit to observed dependences of $C_n^2(h)$ in a mid-latitude climate (it assumes a low tropopause). Figure 2.1 shows the influence of the nominal ground values of C_n^2 and the high altitude wind parameter on respectively the boundary layer and free atmosphere part of the profile.

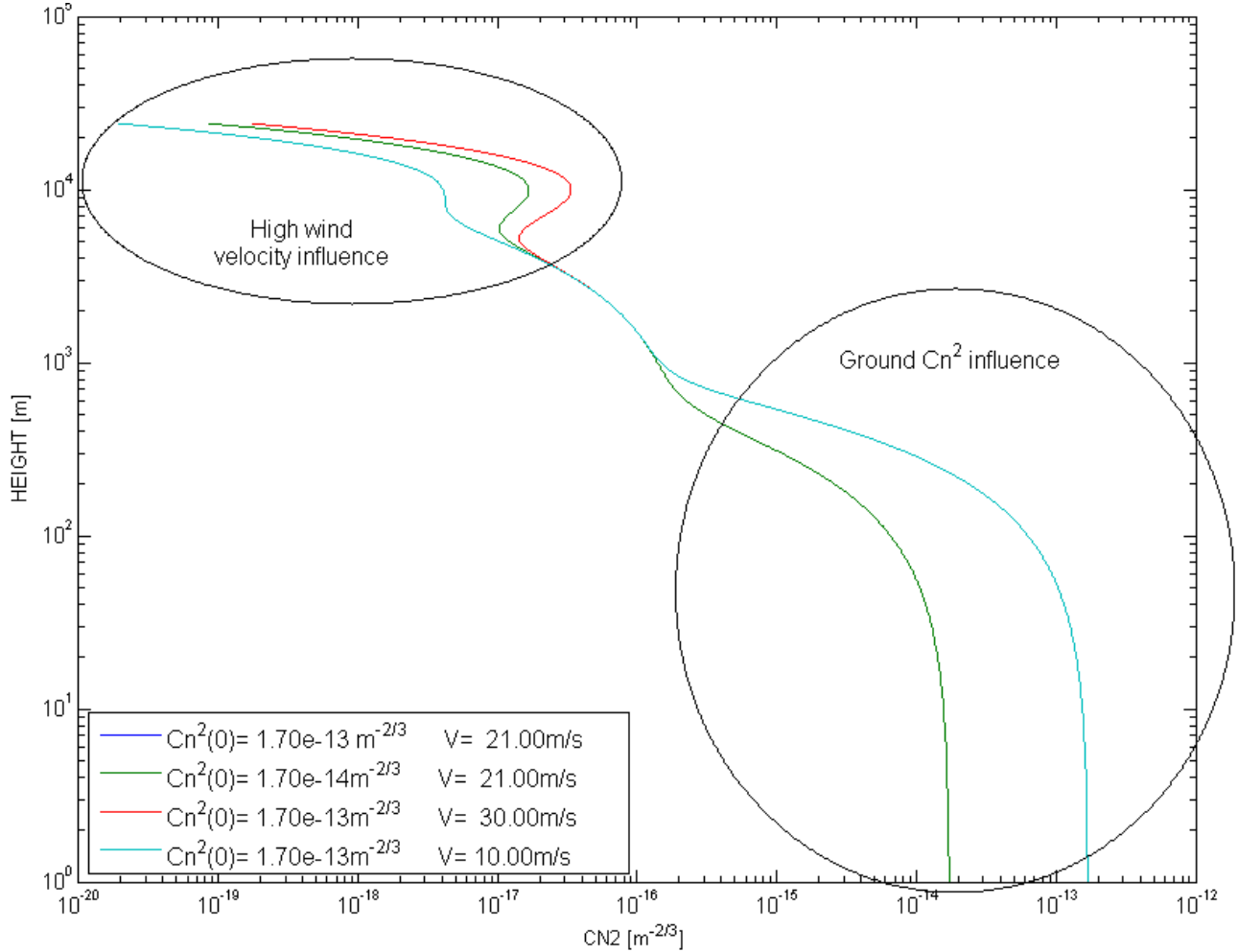


Figure 2.1: Hufnagel-Valley profiles-Influence of input parameters

Moreover, at many sites additional layers have been detected at low- to mid-troposphere altitudes. Therefore a generic HV model, capable of representing any C_n^2 profile as a sum of exponential terms is given in [31]:

$$C_n^2(h) = Ae^{-\frac{h}{H_A}} + Be^{-\frac{h}{H_B}} + Ch^{10}e^{-\frac{h}{H_C}} + De^{-\frac{(h-H_D)^2}{2d^2}} \quad (2.6)$$

where A is the coefficient for the surface (boundary layer) turbulence strength and H_A is the height for its $1/e$ decay, B and H_B similarly define the turbulence in the troposphere, C and H_C define the tropopause peak, and D and H_D define one or more isolated layers of turbulence, with d being the layer thickness.

Application case: The HV model applies to the whole atmosphere; however the boundary layer extension (last exponential term in Eq. 2.4) does not provide a "good" description of near-ground turbulence. Therefore the model should not be used for application depending heavily on a correct modeling of turbulences in the lowest layers of the atmosphere. Furthermore the HV model is better suited for mid-latitude regions.

2.2.2 HAP (Hufnagel/Andrews/Phillips) [4, 5, 6, 7, 8]

It has been shown that for daytime conditions the HV model is not the best suited one as it does not correctly describe the turbulences' behaviour of the lowest layers of the atmosphere. The last exponential term in Eq.2.4 that describes near-ground turbulence conditions predicts a slow decrease in C_n^2 with altitude up to around 1 km. However a number of measurements, among which the experiment of Kaimal et al [29], support the fact that C_n^2 follows a different behavior up to around 1-2 km above ground level during daytime: when there is general mixing (daytime), then on average the turbulence decreases with height above the surface as $h^{-4/3}$. Therefore a more realistic model has been developed, on the basis of the Hufnagel model and by considering Kaimal's model of the boundary layer inversion impact on C_n^2 , by Andrews and Phillips: the HAP model (2009) [6]:

$$C_n^2(h) = 0.00594(v/27)^2(10^{-5}h)^{10}e^{\frac{-h}{1000}} + 2.7 \times 10^{-16}e^{\frac{-h}{1500}} + C_n^2(h_0) \left(\frac{h_0}{h}\right)^{4/3} \quad (2.7)$$

with $h > h_0$, h_0 is the height of the instrument above ground.

Boundary layer turbulence modeling is based on a very detailed theory namely the similitary theory, shortly introduced in this report in section 2.2.3.1 that treats the ARL model which makes direct use of it. With respect to altitude dependence of C_n^2 it presents the following key results: for unstable, free convection, C_n^2 scales with a $-\frac{4}{3}$ exponent in altitude dependence (behaviour included in HAP 2009); for neutral conditions (i.e near sunrise and sunset), the altitude exponent is $-\frac{2}{3}$ and for stable conditions (i.e nighttime) the exponent is $-\frac{2}{3}$ as well. Moreover it should be noted that stable conditions can also occur during day: when there is warm air over cold ground (as for instance snow covered terrain). The latest HAP model (2012) given by Eq. 2.8 [5, 7] follows these results by including a power law behavior as a function of altitude changes that transitions from the $h^{-4/3}$ trend to the $h^{-2/3}$ trend.

$$C_n^2(h) = M \left[0.00594(v/27)^2(10^{-5}(h + h_s))^{10}e^{\frac{-(h+h_s)}{1000}} + 2.7 \times 10^{-16}e^{\frac{-(h+h_s)}{1500}} \right] + C_n^2(h_0) \left(\frac{h_0}{h}\right)^p \quad (2.8)$$

where h_s is the height of ground above sea level. $C_n^2(h_0)$ is the average refractive index structure parameter at h_0 . The parameters M and p , respectively represent the random

background turbulence (at altitudes generally above 1 km) and the power-law parameter depending on the temporal hour of the day. The latter is computed as follows

$$p = \begin{cases} -0.11(12 - TH)^2 + 1.83(12 - TH) - 6.22, & 0.75 < TH < 3.5 \\ 1.45 - 0.02(TH - 6)^2, & 3.5 < TH < 8.5 \\ -0.048TH^2 + 0.68TH - 1.06, & 8.5 < TH < 11.25 \end{cases} \quad (2.9)$$

Computing temporal hours requires knowledge of the local times at which sunrise and sunset occur. The time between sunrise and sunset is equally divided into 12 temporal hours (TH) by the relationship

$$TH = \frac{TIME - SUNRISE}{TP}; \quad TP = \frac{SUNSET - SUNRISE}{12}; \quad (2.10)$$

Figure 2.2 represents the power-law parameter p evolution between the time of sunrise and sunset;

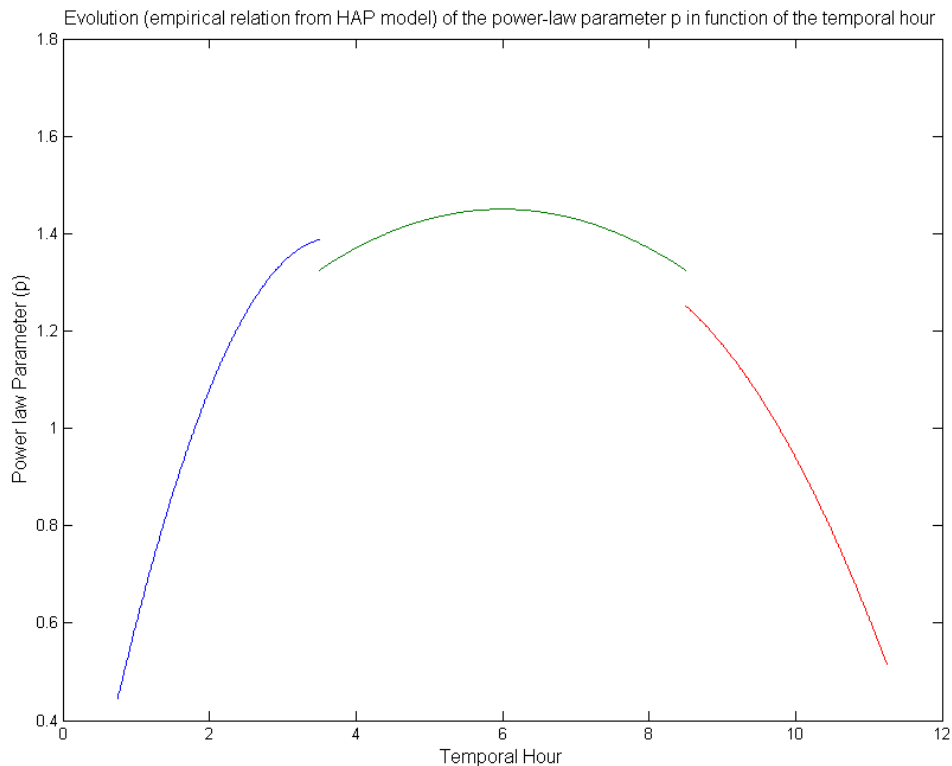


Figure 2.2: Power-law parameter p evolution as a function of temporal hours

Figure 2.3 (a) represents three HAP profiles corresponding to different times of the day i.e. different power law parameters (notice that, according to the time of the day, not only the power law behavior as a function of altitude changes varies but as well does the ground value of C_n^2). Figure 2.3 (b) represents the modifications in the profile if one chooses

different ground heights above sea level (with the same atmospheric conditions for each case, which in reality could be considered senseless).

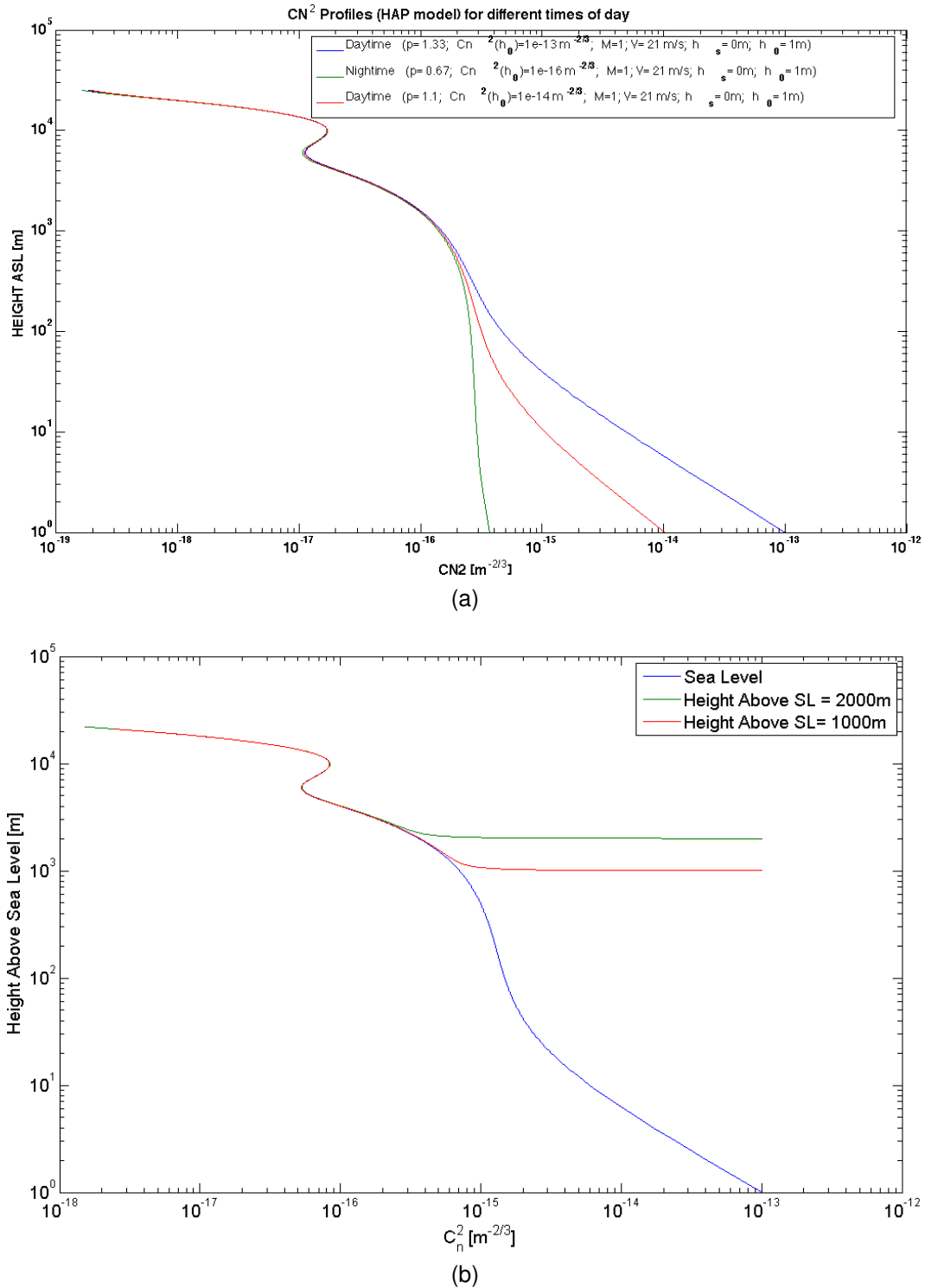


Figure 2.3: Three HAP profiles at different time of the day (a); Three HAP profiles with different reference heights of the ground ASL

Determining the parameters M and $C_n^2(h_0)$ is done by comparing the measured aperture-averaged scintillation index from several distinct aperture diameters (in fact three, necessary because inner and outer-scales are also intended to be determined [5, 7, 8]) with the calculation of the aperture-averaged weak turbulence scintillation index as derived from the Kolmogorov spectrum [23]. This result in a system of three nonlinear equations with three unknowns which had to be solved numerically (using a minimization method more precisely). This model therefore makes use only of scintillation measurements (weighted path-averaged values of C_n^2) taken along a slant path in order to be used as an intermediate result for determining its parameters. However the rule on which the power-law parameter p has been determined is not clearly explained and may not be universal according to the authors. The results of the implementation of this procedure can be found in extensive details in [5, 7]. Figure 2.4 shows the comparison between a typical H-V profile (mid-day turbulence i.e. high ground turbulence: $C_n^2 = 1.7e^{-13}m^{-2/3}$; and average wind speed typical value of 21m/s) and the HAP profile for the same conditions with $p = 4/3$ and the reference level (height above sea level) set to 0m for the sake of comparison. As expected the difference between the two models appears within the first kilometer: the HV model shows an almost constant C_n^2 profile up to about 100m and then decreases steeply. This behavior cannot be realistic.

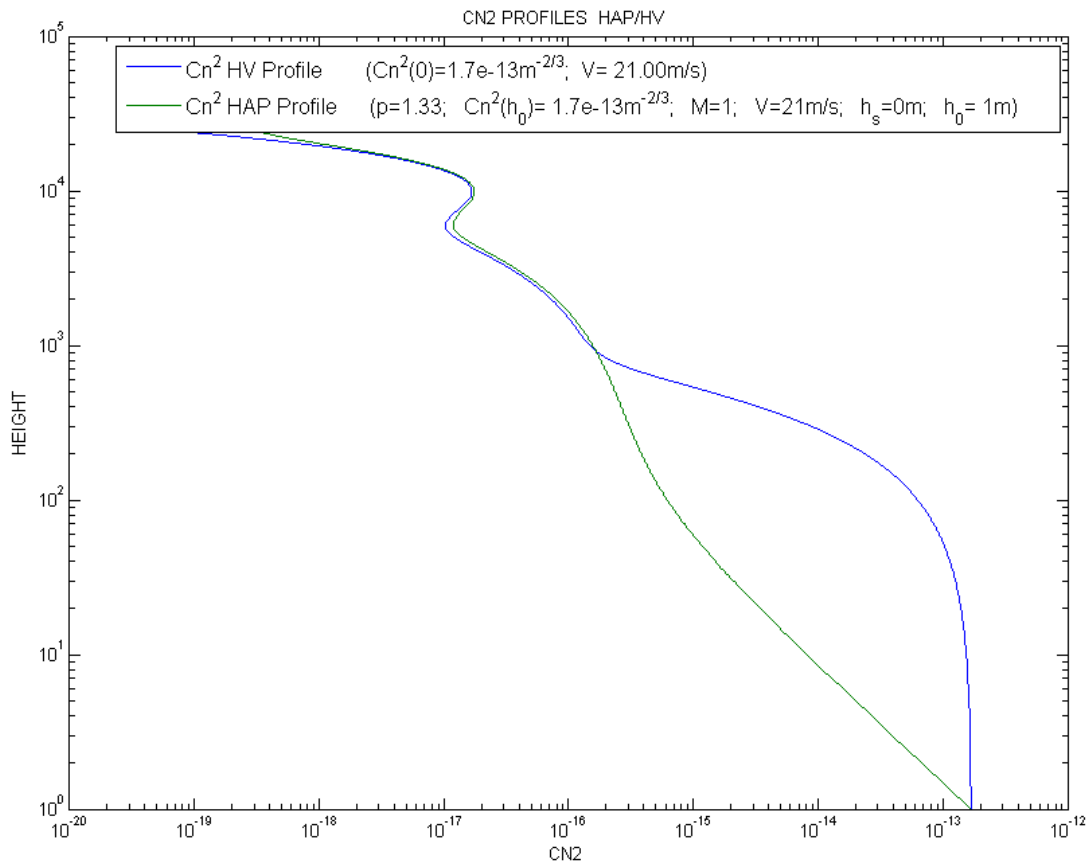


Figure 2.4: HV and HAP models comparison

Application case: As an highly enhanced version of the HV model, the HAP model can be applied to the whole atmosphere. However, since the work published by Phillips et al. is quite recent it is not clear in what extent the model could be used in other regions/sites (the experiments were conducted in California, at the Hollister Air Force Range and at the Naval Air Weapons Test Range in China Lake). More particularly, the derivation of the power-law parameter for the boundary layer modeling is not clearly detailed and it may not be an "universal result". However, a personal correspondance with L.C. Andrews set that the model (particularly the daytime dependant treatment of the boundary layer profile) should be accurate for comun sites in mid-latitudes regions.

2.2.3 ARL (US Army Research Lab) Model [4]

This recent model (2006) developed by Tostfed consist of a single equation combining the effects of each layer of the atmosphere from ground to the upper troposphere. Disparate models covering these different portions of the atmosphere (surface layer, boundary layer,

upper troposphere) were blended together into a single model. Therefore the distinguishing feature of the final model does not reside in the derivation of a new profile based on new measurements or theoretical analysis but "only" in the coupling of the different models of height dependence in different altitude regions of the atmosphere into a single profile. Inputs to the model include the time of day and month of year, cloud cover fraction, and surface meteorological measurements of wind speed, temperature, and an estimate of the current C_n^2 strength. It also requires information concerning the log-normal distribution of turbulence strength. This is because log-mean C_n^2 is not the same as the average C_n^2 . The two are related through the form of the log-normal distribution. The variance of this distribution is required to determine the mean C_n^2 based on log-mean statistics that arises from parametric models such as CLEAR I and AFGL AMOS described later in the present report.

The final profile model includes features that adjust for arbitrary surface measured turbulence levels and stability. The surface layer model is integrated into a boundary layer model described in [29]. To link the boundary layer interface to the upper troposphere, a similarity theory was used consistently with the (modified) CLEAR I model.

2.2.3.1 Surface Layer

The modeling in the surface layer makes a direct use of the fundamental results of the Monin-Obhukov similarity theory (MOST). It seems unnecessary to describe all the fundamental results of the MOST in this report however a concise remark about such findings relies on the following equations provided by Wyngaard [32]:

$$\begin{aligned} C_n^2 &\propto h^{-2/3} \left[1 - 7 \frac{h}{L_{Ob}} \right]^{-2/3} && \text{in unstable conditions } (L_{Ob} < 0) \\ C_n^2 &\propto h^{-2/3} \left[1 + 2.4 \left(\frac{h}{L_{Ob}} \right)^{2/3} \right] && \text{in stable conditions } (L_{Ob} > 0) \end{aligned} \quad (2.11)$$

As similarity theory utilizes dimensional analysis and physical modeling to determine dominant length scales it naturally yields a characteristic scaling length in the surface layer, i.e. L_{Ob} , Monin-Obhukov length, which describes the heat and momentum transfer between the surface and the atmosphere. In theory, above L_{Ob} , one should expect C_n^2 to follow the $h^{-4/3}$ power law described earlier. Under neutral atmospheric conditions and at night an $h^{-2/3}$ height dependence is expected. The main problem in the surface layer is not to determine the height dependence provided for instance by Eq. 2.11 but rather the Monin-Obukhov length L_{Ob} . To do so, similarity theory was used i.e. wind and temperature profiles near the surface are assumed similar under comparable stability conditions. Three stability-dependent quantities are therefore of interest since that they parameterize the vertical structures of temperature and wind speed in the surface layer: the scaling potential temperature θ_* , the friction velocity u_* , and L_{Ob} itself. They are related by the following expression:

$$L_{Ob} = \frac{u_*^2 \theta}{k^2 g \theta_*} \quad (2.12)$$

where k is the dimensionless von Karman's constant ($=0.4$), g is the gravity acceleration, and θ is the potential temperature at a reference height h_r . The friction velocity is defined by

$$u_* = \frac{ku}{\ln(h_r/h_0) - \Psi(L_{Ob})} \quad (2.13)$$

where u is the wind speed at h_r , h_0 is the surface roughness height, and Ψ is the stability-dependent diabatic influence function of wind velocity given by

$$\Psi = \Psi_m\left(\frac{h_r}{L_{Ob}}\right) + \Psi_m\left(\frac{h_0}{L_{Ob}}\right) \quad (2.14)$$

where for unstable conditions

$$\Psi_m\left(\frac{h}{L_{Ob}}\right) = 2 \ln\left(\frac{1+x}{2}\right) + \ln\left(\frac{1+x^2}{2}\right) - 2\arctan(x) + \frac{\pi}{2} \quad (2.15)$$

with

$$x = \left(1 - \frac{16h}{L_{Ob}}\right)^{\frac{1}{4}} \quad (2.16)$$

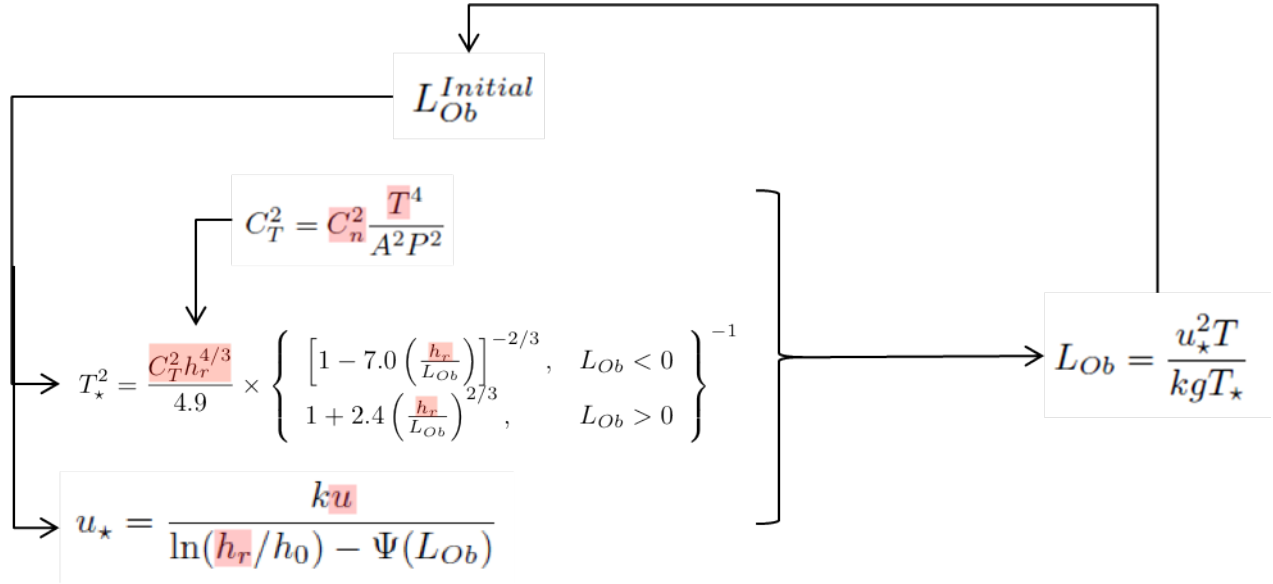
and where in the stable case

$$\Psi_m\left(\frac{h}{L_{Ob}}\right) = -17 \left(1 - \exp\left(-0.29 \frac{h}{L_{Ob}}\right)\right) \quad (2.17)$$

The scaling potential temperature is given by

$$\theta_* = \frac{\theta - \theta_0}{\ln(h_r/h_0) - \Psi_h(L_{Ob})} \quad (2.18)$$

where θ_0 is the air temperature at h_0 and Ψ_h is diabatic influence function of temperature. Substituting Eq. 2.13 and Eq. 2.18 in Eq. 2.12 one could determine L_{Ob} using measurements of u , θ and θ_0 . However, Usually the latter is difficult to predict because it does not occur at a specific surface. Rather, it is representative of the equivalent effects of the surface temperatures of the bare ground and foliage (leaf, stem, and twig) surfaces. Moreover the problem of observationally evaluating L_{Ob} is also related to temperature and wind measurements, generally difficult to perform practically in the field, and normally, one does not take measurements at more than one atmospheric level. To circumvent this difficulty Tofsted et al. proposed an iterative scheme through which L_{Ob} is refined. Three parameters are needed as inputs: wind speed u , temperature T and a C_n^2 value all at the same reference height h_r . If one is considering daytime or nighttime conditions is also required as well as the roughness height h_0 . A diagram of this iterative process is represented in figure 2.5.


 Figure 2.5: Block diagram - L_{Ob} iterative process

First of all one needs to relate L_{Ob} to C_n^2 , u and T . Considering the following expression of C_T

$$C_T^2 = T_*^2 h^{-2/3} 4.9 \times \left\{ \begin{array}{l} \left[1 - 7.0 \left(\frac{h}{L_{Ob}} \right) \right]^{-2/3}, \quad L_{Ob} < 0 \\ 1 + 2.4 \left(\frac{h}{L_{Ob}} \right)^{2/3}, \quad L_{Ob} > 0 \end{array} \right\} \quad (2.19)$$

and the following mean to convert C_T^2 to C_n^2 and vice-versa:

$$C_n^2 = C_T^2 \frac{A^2 P^2}{T^4} \quad (2.20)$$

where $A = 79 \times 10^{-6} K/mb$.

An initial guess of L_{Ob} is obtained by eliminating C_T^2 from Eq. 2.20 for the neutral atmospheric conditions:

$$L_{Ob} \sim \pi_s \frac{k u^2}{g [\ln(h_r/h_0)]^2} \frac{AP}{T} \frac{1}{\sqrt{C_n^2 h_r^{1/3}}} \sqrt{4.9} \quad (2.21)$$

where $\pi_s = \pm 1$, (-1 for daytime i.e. unstable atmospheric conditions and +1 for nighttime i.e. stable atmospheric conditions). π_s can be predicted using local sunrise/sunset times and offsets to estimate neutral event transitions. Then, along with the values of C_n^2 and u at the reference height h_r , L_{Ob} is used in the evaluation of T_* and u_* . A new value of L_{Ob} is eventually computed using

$$L_{Ob} = \frac{u_*^2 T}{k g T_*} \quad (2.22)$$

This iteration procedure normally stabilizes in less than ten steps.

2.2.3.2 Boundary Layer

The remainder of the boundary layer model above the surface is developed only for daytime conditions. The primary assumption concerning the diurnal variations of the turbulence is that they are due to the dominance of convective action. It is often called the mixed layer because it features both upward and downward air motion associated with convective cell development. Within the layer a nearly constant potential temperature vertical profile prevails. The profile developed by Tofsted et. al. is inspired by the work of Kukharets and Tsvang [21]. However it is modified according to the data presented by Kunkel et. al. [24] characterizing desert regions. The final expression of the boundary layer is given by:

$$\begin{aligned}
 X_K(h) &= \log_{10}(C_T^2) \\
 &= \log_{10}(C_{TS}^2) + 0.775 \exp \left[-\frac{(h - 0.95h_i)^2}{2(h_i/7)^2} \right] \\
 &\quad + \left[\frac{1}{3} + \frac{4}{3} \log_{10} \left(\frac{h}{h_i} \right) \right] \sigma \left[\frac{h_i - h}{h_i/8} \right]
 \end{aligned} \tag{2.23}$$

where C_{TS}^2 is the C_T^2 value produced by the surface layer equation (Eq. 2.19) and $\sigma(h) = \frac{1}{1+e^h}$ (it has the properties $\sigma(h) \rightarrow 0$ as $h \rightarrow +\infty$ and $\sigma(h) \rightarrow 1$ as $h \rightarrow -\infty$). The net effect of these expressions is that the first term on the right-hand side of Eq. 2.23 generates the surface layer effect when near the ground. The second term is a Gaussian characteristic of the inversion level. The third term has the effect of neutralizing the general height dependence above the inversion layer.

The parameter h_i is the height of the elevated inversion base also corresponding to the height of the mixed layer itself. This height varies according to meteorological conditions. However general trends over a day and over seasons can be observed in this variations. The height of the mixed layer appears to rise following sunrise and fall prior to the evening neutral event. This behavior appears to contradict the behavior illustrated in figure 1.3 where the mixed layer abruptly develops into the residual layer around the time of the evening neutral event. Apparently the true behavior is that the residual layer develops gradually, starting at the entrainment zone and building gradually downward toward the surface. This is due to the surface heating gradually diminishing throughout the afternoon as the solar zenith angle increases. The solar input therefore can only support a diminished mixed layer thickness as the zenith angle increases. Also, the slope of the increase in the layer thickness is more gradual in the morning than the rate of height collapse in the afternoon. These constations were made by Tofsted et al. after analyzing sets of aggregated h_i data generated for the WSMR region. A numerical model was then developed to provide approximated mixed layer depths over the year as shown in figure 2.6.

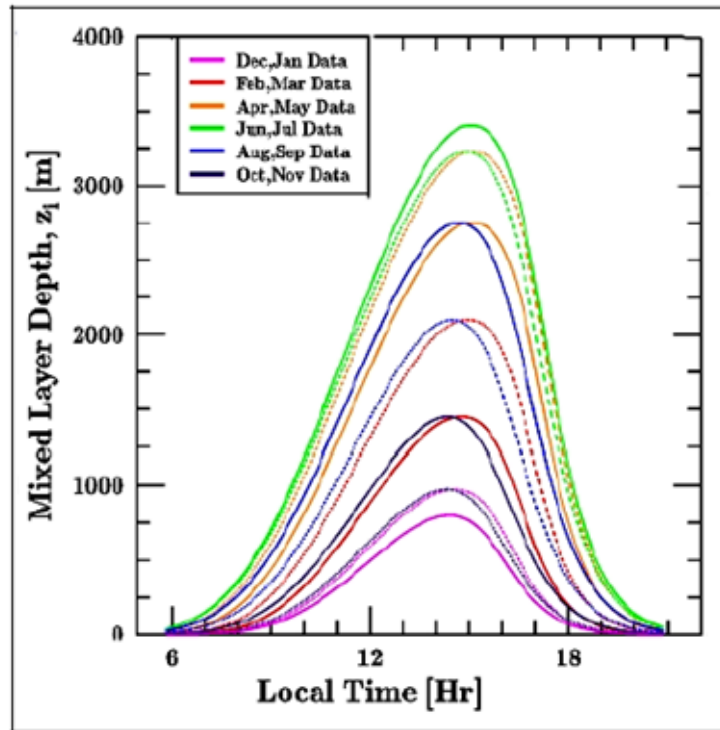


Figure 2.6: Depth of the daytime boundary layer (convective mixed layer)

The results of this model for daytime mixed layer depth therefore provides the missing parameter needed for the boundary layer model given in Eq. 2.23. Finally, for heights below 3 km, C_n^2 is modeled by:

$$N_K(h) = X_K(1000h) + \log[A^2 P^2 / T^4] \quad (2.24)$$

Pressure and temperature profiles are approximated by adiabatic atmospheric profiles:

$$T(h) = T(0) - 6.455h \quad (2.25)$$

and

$$P(h) = P(0) \exp(-h/8) \quad (2.26)$$

The next step is to link the boundary layer model to an upper troposphere model based on the CLEAR I study.

2.2.3.3 Troposphere

To model the upper atmospheric C_n^2 structure, Tofsted et. al. considered mainly two non-parametric models: the AFGL AMOS and the CLEAR I (both described in section 2.3.6 and section 2.3.7). These two models are identical above an altitude of 11km. However they present major differences below this height. Since the authors are primarily interested

in desert/land "wargaming scenarios", CLEAR I (the third expression in Eq. 2.59 ; starting at about 10km) was chosen and linked to the boundary layer model starting at about 3km (AGL) using an approximation of CLEAR I starting in the mid troposphere (5km ASL). A conversion from ASL to AGL was also implemented. The new "CLEAR I" expression, combining both mid-level and upper-level original CLEAR I functions is given by:

$$N_{mu}(h) = N_{mid}\sigma\left[\frac{h-7.8}{2.4}\right] + N_{upper}(h)\sigma\left[\frac{7.8-h}{2.4}\right] - 1.3\sigma\left[\frac{h-9.2}{1.6}\right]\sigma\left[\frac{9.2-h}{1.6}\right] \quad (2.27)$$

where $N_{mid} = -16.23$ and

$$N_{upper}(h) = -17.0577 - 0.0449h - 0.0005h^2 + 0.6181 \exp\left(-\frac{(h-15.5617)^2}{2 \times 3.4666^2}\right) \quad (2.28)$$

It is used for heights above 10km. Finally the boundary layer and the upper atmosphere profiles can be combined, smoothly modeling the transition between the boundary layer and the upper atmosphere, using again sigmoid functions as:

$$N(h) = \sigma(h-7)N_{mu}(h) + \sigma(7-h)N_K(h) \quad (2.29)$$

where $N(h)$ now represents the log-base-10 mean C_n^2 ; h is in km.

2.2.3.4 Nighttime conditions

A useful boundary layer equivalent of Eq. 2.23 does not exist (lack of measurements) for stable conditions. Therefore one must postulate that the C_T^2 behavior in surface layer continues to the top of boundary layer:

$$X_X(h) = \log_{10}(C_{TS}^2) \quad (2.30)$$

This functional form ensures that C_n^2 will decrease with height primarily due to pressure and temperature decreases with height. However this remains only a rough estimation of the general behavior. Analogously to the unstable case one can write

$$N_X(h) = X_X(1000h) + \log_{10}[A^2 P^2 / T^4] \quad (2.31)$$

Finally, the boundary layer model is linked to the CLEAR I model using

$$N_N(h) = \sigma\left(\frac{h-1.5h_i}{h_i/3}\right)N_{mu}(h) + \sigma\left(\frac{1.5h_i-h}{h_i/3}\right)N_X(h) \quad (2.32)$$

where h_i is the depth of the total boundary layer from the surface to the base of the capping inversion.

2.2.3.5 Final profile

The vertical structure model then consists of equations combining effects of each layer combined into a total form in the following equation

$$C_n^2(h) = 10^{N(h)} \tag{2.33}$$

Figure 2.7 represents the total profile for both night and day time conditions for the same input parameters at reference height of 1 m.

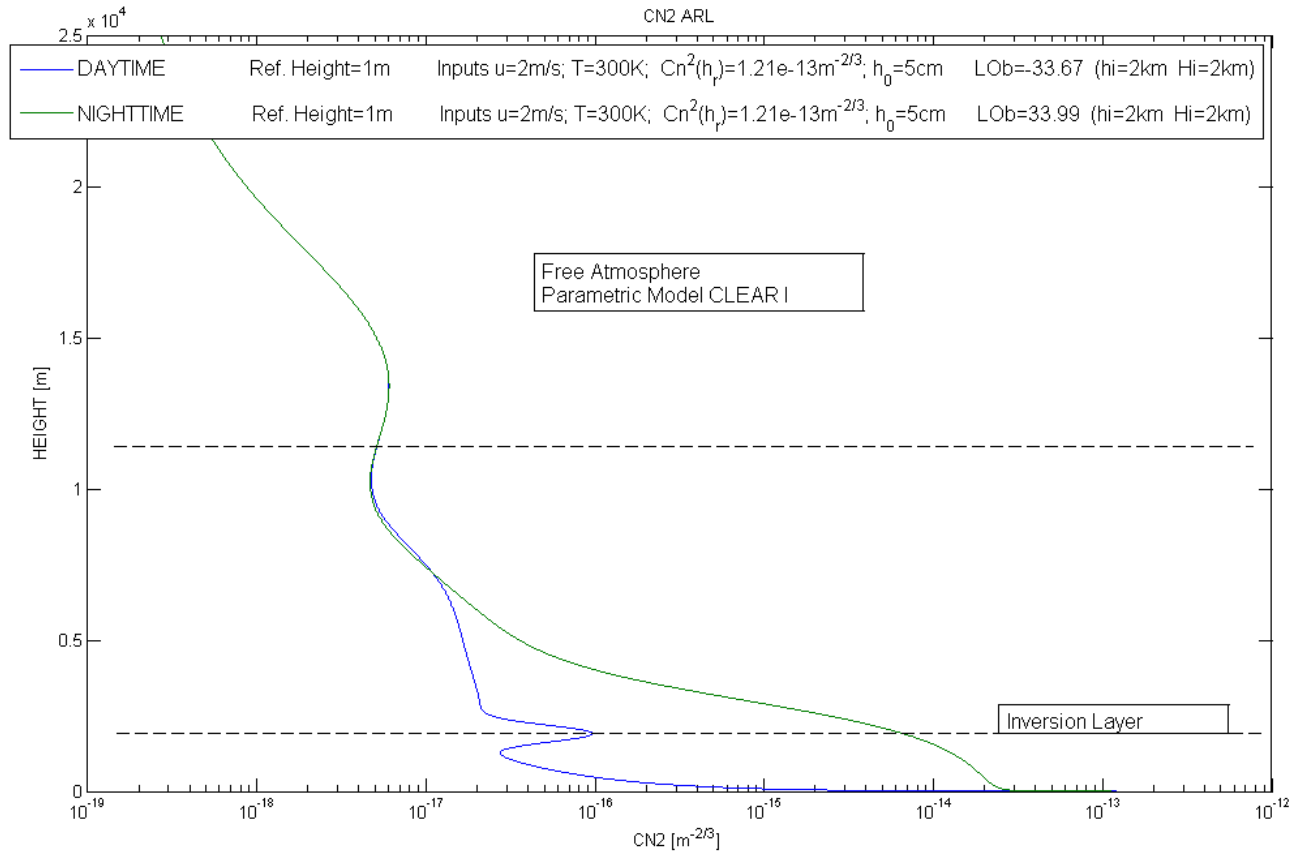


Figure 2.7: ARL profiles for daytime (blue) and nighttime (green) conditions

Application case: This parametric model can be applied to the whole atmosphere. It results from the combination of three different models describing the surface layer, the boundary layer and the free atmosphere layers. A nighttime/daytime differentiation exists for the surface layer model. The latter is based on Monin-Obhukov similarity theory that constitutes a landmark of modern micrometeorology. However the boundary layer term is derived from measurements made in desert regions as well as the free atmosphere profile which is derived from a parametric model (CLEAR I) developed for the New Mexico desert. It is therefore expected that the ARL profile is best suited for desert regions. Moreover the nighttime conditions are not properly modeled in the boundary layer according to the authors themselves. Thus, it should be carefully used in such conditions.

2.2.4 Aeronomy Laboratory Model (NOAA) [9, 10]

The "NOAA model" was developed by VanZandt et. al. in 1978 for estimating mean values C_n^2 in the free atmosphere (only). It is based on a statistical treatment of the fine structure of the vertical wind shears, the fine structure of the potential temperature (defined in terms of the Brunt-Vaiala frequency N) and the statistics of encountering a turbulent layer of thickness L . Therefore the profiles can be derived from meteorological data available from standard radiosonde observations.

The authors started by considering a slab of the atmosphere of 150m or greater thickness. Embedded in the large-scale laminar flow of the slab are many fine-scale turbulent flows, called "layers" with outerscale L . Initially, three quantities are of interest: the mean stability, wind shear, and gradient of humidity of the slab respectively noted as N^2 , S and q' all of which computable from rawinsonde measurements.

For a thin turbulent layer, assuming that the turbulence is homogeneous and isotropic, C_n^2 is estimated by Tatarskii expression[33]:

$$C_n^2 = 2.8M^2L^{4/3} \quad (2.34)$$

where M is the vertical gradient of generalized potential refractive index for the turbulent layer given by:

$$M = -77.6 \times 10^{-6} \frac{P}{T} \frac{N^2}{g} \left[1 + 15500 \frac{q}{T} - 7750 \frac{q'/T}{N^2/g} \right] \quad (2.35)$$

with P the pressure in mbar, T temperature in K and g the gravitational acceleration. Ideally, one could compute the "total" $\overline{C_n^2}$ simply by adding the C_n^2 for all the layers in the slab. However this would require a tremendous amount of measurements. Furthermore, it would imply that all turbulent layers in the slab are identical, thence justifying the probability approach. Considering such a formalism and as a first stage, C_n^2 can be expressed as:

$$\overline{C_n^2} = \int_{L_{min}}^{L_{max}} dL \iint_{R_i \leq R_{ic}} dS dN^2 \int_{-\infty}^{\infty} dq' p_4 C_n^2 \quad (2.36)$$

In this equation, p_4 would be a multivariate probability density function depending on fine-scale as well as large-scale parameters of a point in the layer. R_i is called the gradient Richardson number a dimensionless ratio related to the buoyant production or consumption of turbulence divided by the shear production of turbulence used to indicate dynamic stability and the formation of turbulence. Therefore, in the present formulation a given fine-scale layer in the slab is considered turbulent if its R_i is less than or equal to critical value R_{ic} .

Making use of statistical theory features and by factoring some of the probability density functions of Eq. 2.36, it can be shown that finally (see [9] for the full derivation and formalism of the model), the profile is expressed as

$$C_n^2 = 2.8M_0^2 \int_{L_{min}}^{L_{max}} dL p_L L^{4/3} \int_0^{\infty} dS p_S \int_{-\infty}^{S^2 R_{ic}} dN^2 p_N (N^2)^2 \quad (2.37)$$

where $M_0 = -77.6 \times 10^{-6} \frac{P}{T} \frac{1}{g}$, and p_L , p_S and p_N are probability densities for the outer scale of the layer, shear, and Brunt-Vaisala frequency. Note that the profile has to be

computed/estimated numerically: for solving Eq. 2.37, given mean values of P , T , q , S , N^2 or other relevant parameters, the integrals can be estimated for instance by a gaussian quadrature method as detailed in [9] where a full description of such a procedure and even a program is given. Figure 2.8 shows the NOAA model as well as the Hufnagel profiles compared to thermosondes data.

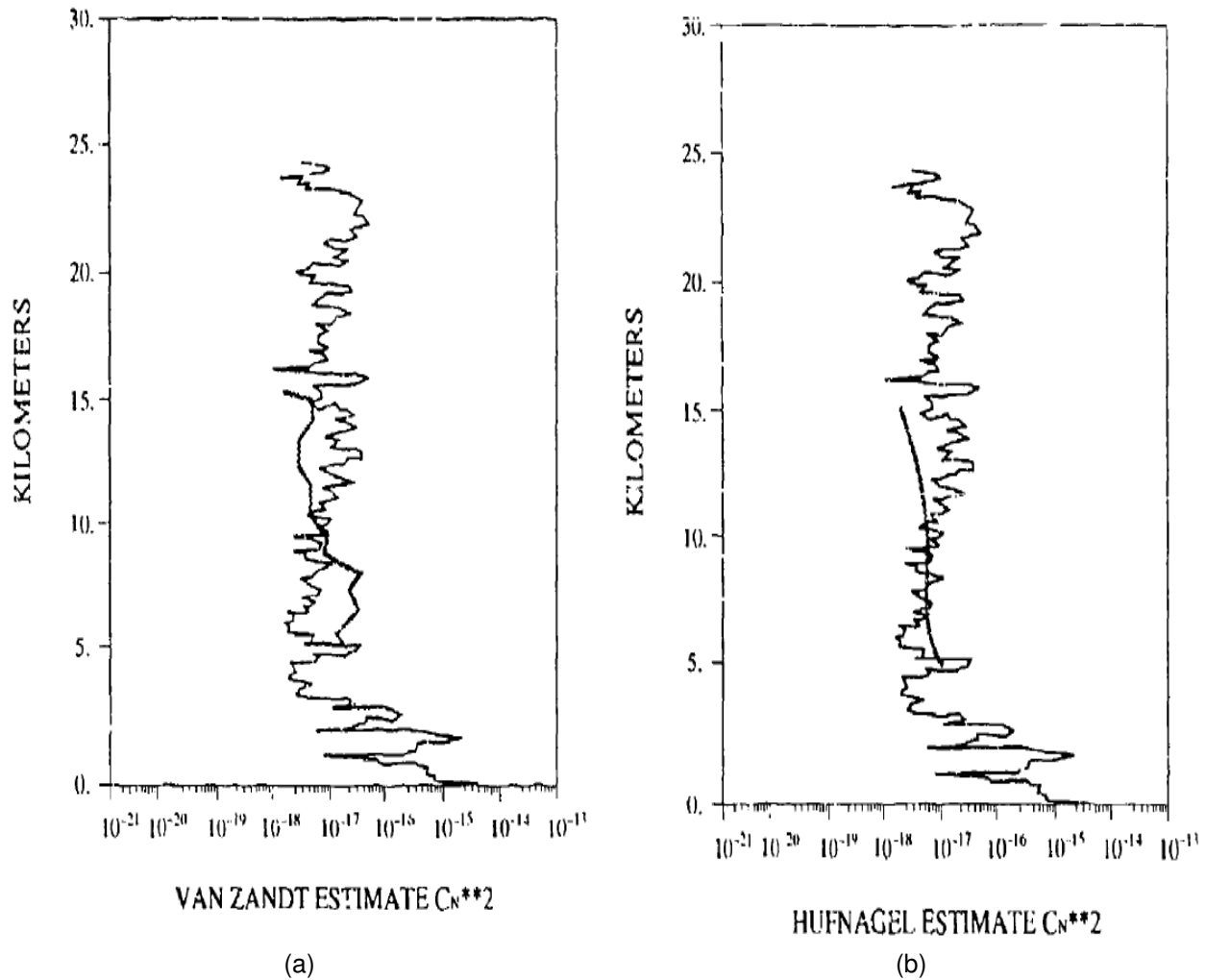


Figure 2.8: (a) NOAA (or VanZandt) model and data comparison; (b) Hufnagel model and data comparison. Taken from [11]

Application case: The model is intended to the free atmosphere only. Based on a statistical formalism, C_n^2 can be computed numerically only. All the input parameters of the model can be acquired from (or derived from) radiosonde data.

2.2.5 AFGL Radiosonde Model [11]

The AFGL Radiosonde Model provides profile for the free atmosphere (only) using as starting point the same formalism as the NOAA model: Tatarskii expression given anew here by

$$C_n^2(h) = 2.8M(h)^2L^{4/3} \quad (2.38)$$

where M is defined this time as a function of temperature T , pressure P and the temperature gradient $\frac{dT}{dh}$:

$$M^2(h) = \left[\left(\frac{79 \times 10^{-6} P}{T^2} \right) \left(\frac{dT}{dh} + \gamma \right) \right]^2 \quad (2.39)$$

With γ defined as the dry adiabatic lapse rate of $9.8 \times 10^3 K/m$. L , in Eq. 2.38, is "the outer length" (as defined by the authors), that is the largest scale of inertial range turbulence. The AFGL model relies on the determination of L from radiosonde data. It is generally known that above the convective boundary layer, atmospheric turbulence occurs in thin layers shaped like pancakes that are miles in width and tens of meters thick (the "slabs" in the NOAA model). A shear type of instability leads to the formation of the layers, and the shears are generally caused by gravity waves [34].

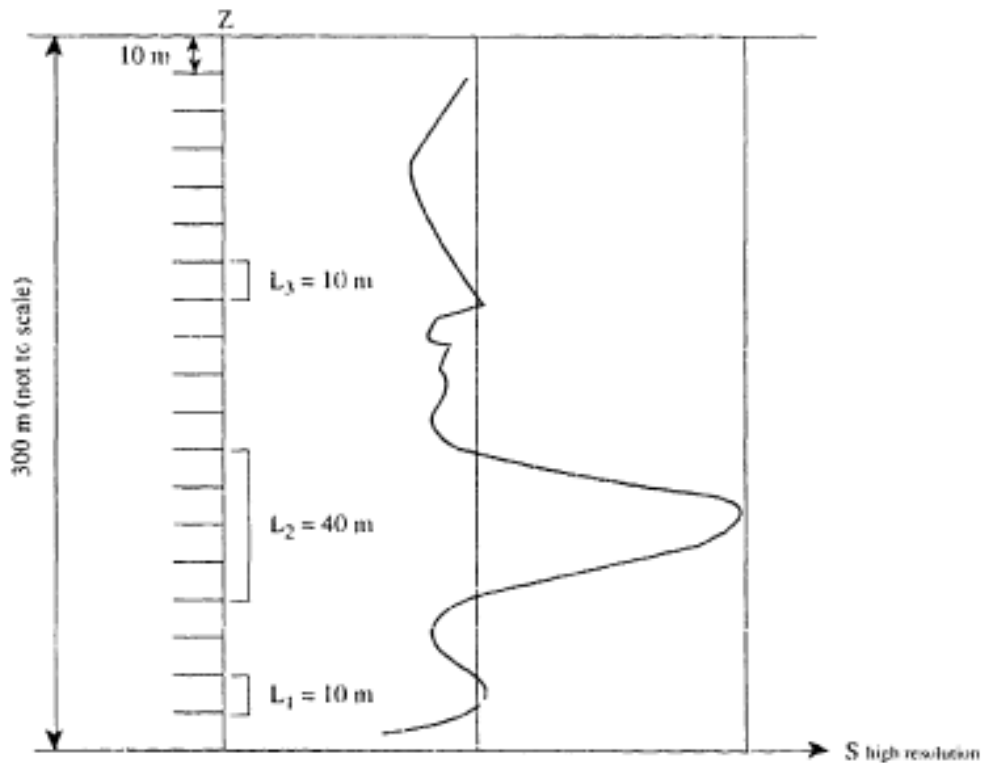


Figure 2.9: Taken from [11]. Method for assigning S_{raw} to $\langle L^{4/3} \rangle$. Uses weighted average Eq. 2.43

Standard radiosondes, at the time the model was proposed (in 1993), reported data such as velocity at intervals of 300m minimum. However, it is presumed that the turbulent layers are of order 1/10 of such radiosondes resolution. Therefore, the shears responsible have to be on that same scale. To overcome the limitations in the measurements, (as for NOAA) a statistical treatment, more precisely, an association between the large scale shears (S_{raw}) and the average of $L^{4/3}$ contained within the 300m height range must be determined. The procedure followed by Dewan et. al. in order to develop such a model are described in the following with reference to figure 2.9. As a first step, in order to achieve such a statistical association, high resolution (10m) stratospheric wind velocity profiles were used to obtain high resolution shears using the following equation:

$$S \equiv \left[\left(\frac{dV_N}{dh} \right)^2 + \left(\frac{dV_E}{dh} \right)^2 \right]^{1/2} \quad (2.40)$$

where V_N and V_E are the north and east horizontal wind components. The instability criterion that was used is the following:

$$(S_c)^2 > (N)^2(0.5)^{-1} \quad (2.41)$$

All shear region exceeding $S_c = 0.015s^{-1}$ for the troposphere or $0.03s^{-1}$ for the stratosphere are supposed turbulent. Moreover, from a rule of thumb (as explained previously) arises the fact that the outer length L is of the order of one tenth the thickness of a turbulent layer. This is expressed by the following relation:

$$L = 1/10\mathcal{L} \quad (2.42)$$

which is in fact taken into account only when the model is applied to the radio-sonde data (Eq. 2.45). Finally, the weighted average of $(\mathcal{L})^{4/3}$ is simply obtained by:

$$\langle (\mathcal{L})^{4/3} \rangle \equiv \sum \mathcal{L}^{4/3}(\mathcal{L}/290) \quad (2.43)$$

The next step consisted in plotting S_{raw} data against $\langle (\mathcal{L})^{4/3} \rangle$ in order to obtain the following final model using a straight line regression:

$$\begin{aligned} \langle (\mathcal{L})^{4/3} \rangle &\equiv Y = 1.64 + 42.0S_{raw} && \text{Troposphere} \\ Y &= 0.51 + 50.0S_{raw} && \text{Stratosphere} \end{aligned} \quad (2.44)$$

Finally, the profile is:

$$C_n^2(h) = 2.8(0.1)^{4/3}M(h)^210^{Y(h)} \quad (2.45)$$

Therefore, in this model of the free atmosphere, data for the tropopause and the stratosphere have to be treated separately. It is important to ascertain the altitude of the tropopause on site. In matching thermosondes observations the NOAA and the AFGL models were comparable however, the latter is obviously computationally simpler. Figure 2.10 shows the AFGL Radiosonde model profile compared to thermosondes data.

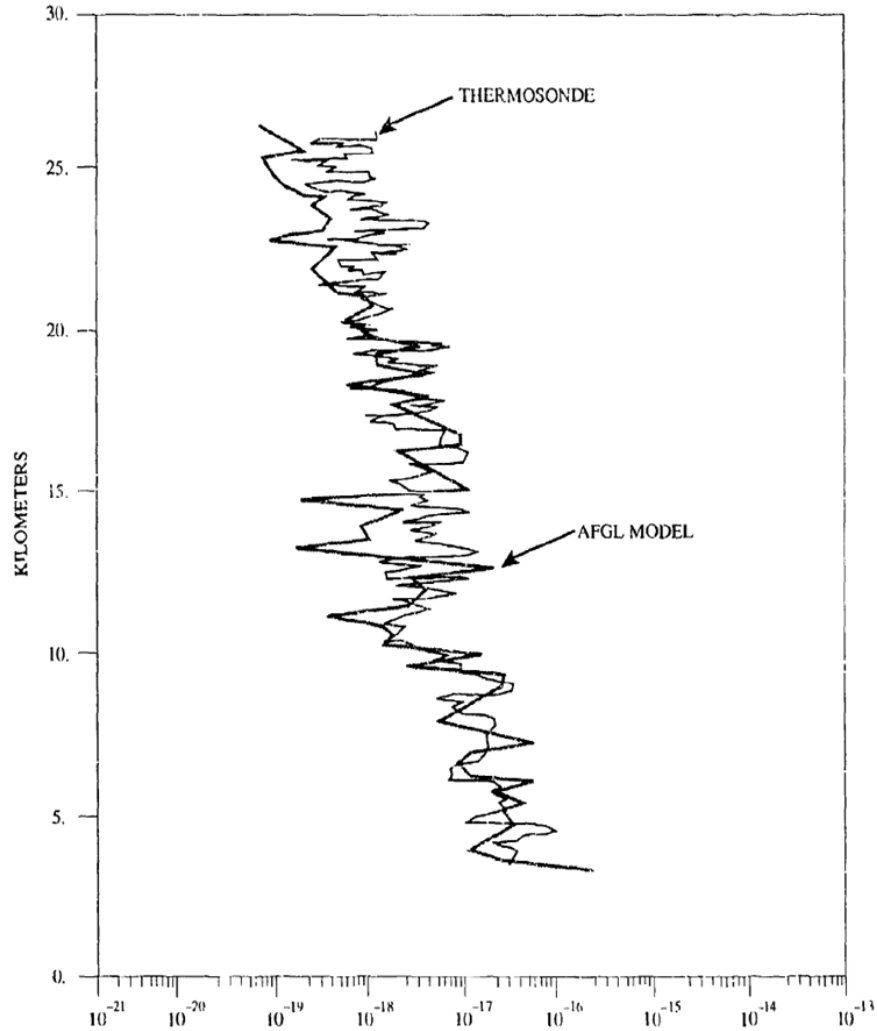


Figure 2.10: AFGL Radiosonde model and data comparison. Taken from [11]

Application case: This model is based on the same "physics" than the NOAA model. However the statistical treatment is simpler and the results are similar to those obtained with NOAA. The resulting model equation can take data for tropopause and the stratosphere separately only. It is therefore primordial to ascertain the altitude of the tropopause on site. The input data required can be collected by radiosondes.

2.2.6 PAMELA [12, 13, 14]

The PAMELA model is one of the most developed model providing C_n^2 values within the surface boundary layer (up to several hundreds of meters). It requires a large set of input parameter such as latitude, longitude, date, time of day, percent cloud cover, terrain type (roughness), as well as a single measurement (or estimate) of atmospheric temperature

, pressure and wind speed at the height of the desired C_n^2 estimate. This model therefore does not constitute an actual profile modeling for satellite-to-ground links as it does not include the free atmosphere. However it provides an interesting insight on how the boundary layer could be properly described which is the main weakness of most of the parametric models presented.

A complete description of the theory and algorithm upon which the PAMELA model is based are provided in [12]. It leads to the following set of equations required to estimate the refractive index structure parameter

$$C_n^2 = \frac{bK_h}{\epsilon^{1/3}} \left(\frac{\partial n}{\partial h} \right)^2 \quad (2.46)$$

where

$$\frac{\partial n}{\partial h} \simeq \frac{(-77.6 \times 10^{-6} Pa) T_* \Phi_h (\frac{h}{L})}{k_v h T^2} \quad (2.47)$$

and where

ϵ is the energy dissipation rate

K_h is the turbulent exchange coefficient for heat

b is a constant commonly approximated by 2.8

n the refractive index

h the reference height

T_* is the characteristic temperature

Φ_h is the dimensionless temperature gradient

L is Monin-Obukhov length

k_v is von Karman's constant taken to be 0.4

T the temperature

Application case: Applicable only to the boundary layer (more precisely the surface layer i.e. few hundred meters maximum). Measurements of some of the input parameters such as pressure and wind speed, corresponding to the height of the laser receiver, have to be used for the most accurate C_n^2 estimate.

2.2.7 Sadot and Kopeika Model [15, 16]

Most of the C_n^2 models' general approaches of development rely on micrometeorology involving point measurements of local gradients, wind shear, etc. However, for a long line of sight, micrometeorological data are often difficult to obtain and are not readily available opposed to macroscale weather parameters such as air temperature, wind speed and direction, relative humidity etc., which do not vary too greatly with distance and are much more readily available. Kopeika has been really active in developing such (empirical) models solely based on meteorological relations for diverse sites (for instance a variation of the model presented here exists for coastal environments [16]). Sadot and Kopeika's model, published in 1992, represents an attempt to provide C_n^2 from macroscale meteorology measurements (i.e. available from standard weather forecast). It includes also the effect of solar flux and total cross-area (TCSA) of the aerosol particulates per cubic meter,

two parameter that have a significant effect on beam scintillation. These meteorological data (air temperature, relative humidity, wind speed, wind direction, and temporal hour) were input to a computer, together with C_n^2 values evaluated from scintillation measurements. The data were analyzed and several regression models, based on least-square error, were developed to obtain the best estimation of C_n^2 (regression coefficients see table 2.2). The correlation between estimated and measured values was up to 93.4%. The model is described by:

$$C_n^2 = A_1W + B_1T + C_1RH + C_1RH^2 + C_3RH^3 + D_1WS + D_2WS^2 + D_3WS^3 + E_1flux + F_1TCSA + F_2TCSA^2 + G \quad (2.48)$$

where

W is temporal hour weight (see table 2.1)

T is temperature (K)

RH is relative humidity (%)

WS is wind speed ($m.s^{-1}$)

$flux$ is the solar flux ($Cal.cm^{-2}.min^{-1}$)

$TCSA$ is total cross-sectional area of particles per cubic meter (cm^2/m^3)

A_1, B_1, C_1, \dots, G are regression coefficients (see table 2.2)

The dynamic range of meteorological conditions valid for this model are temperature range from 9 to 35°C, relative humidity from 14 to 92%, and wind speed dynamic range between 0 and 10 $m.s^{-1}$. The effect of solar flux on C_n^2 is understood through its contribution to the temperature gradient. Although the temporal hour parameter, gives information about solar flux as well, using the precise data, if available, is better as it provides quantitative information concerning cloudiness for instance. As for the temperature coefficient itself, the solar flux should be positive as it induces higher temperatures usually leading to larger temperature gradient and hence to stronger turbulence. Relative humidity, and wind speed coefficients are negative since that high relative humidity is usually related to low-temperature and low-humidity gradients and, wind causes air mixing and therefore decreases the inhomogeneity of temperature and humidity producing overall a decrease in C_n^2 . Finally, large TCSA increases beam scintillations therefore the overall contribution of the TCSA coefficients to the regression model is positive, i.e., to increase the predicted value of C_n^2 .

	Temporal Hour Interval	Relative Weight (W)
Sunrise	until -4	0.11
	-4 to -3	0.11
	-3 to -2	0.07
	-2 to -1	0.08
	-1 to 0	0.06
	0 to 1	0.05
	1 to 2	0.1
	2 to 3	0.51
	3 to 4	0.75
	4 to 5	0.95
	5 to 6	1.00
	6 to 7	0.90
	7 to 8	0.80
	8 to 9	0.59
Sunset	9 to 10	0.32
	10 to 11	0.22
	11 to 12	0.10
	12 to 13	0.08
	over 13	0.13

Table 2.1: Temporal hour weight function (S-K model)

A_1	5.9E-15
B_1	1.6E-15
C_1	-3.7E-15
C_2	6.7E-17
C_3	-3.9E-19
D_1	-3.7E-15
D_2	1.3E-15
D_3	-8.2E-17
E_1	2.8E-14
F_1	-1.8E-14
F_2	1.4E-14
G	-3.9E-13

Table 2.2: Regression coefficient values (S-K model)

The model presented here was obtained from horizontal path measurements (variation of few meters of the beam elevation) and therefore does not constitute by itself a profile model. Nevertheless, it gives an interesting point of view on how one could take into account the effect of uncommon parameters (such as aerosols concentration). Moreover Kopeika suggested that this value of C_n^2 , calculated using Eq. 2.48, can be scaled up to about 100m

according to

$$C_n^2(h) = C_{n0}^2 h^{-p} \quad (2.49)$$

where C_{n0}^2 is the refractive-index structure coefficient at the the surface.

Application case: Applicable to the boundary layer only (more precisely surface layer few tens of meters using any scaling relation). It requires a large set of input parameters, some of them not so common, such as relative humidity, solar radiation and aerosol loading in the atmosphere. It is not an actual profile.

2.3 Non-Parametric Models

Non-parametric models are described in the following sections. The H-V 5/7 and H-V Night models are simply well-known application cases of the generic H-V model. The Greenwood model is often used for astronomical measurements from mountaintops. The Gurvich model is a phenomenological model developed in order to take into account different regime of turbulence strength. Finally, the SLC the AFGL AMOS and CLEAR I models were developed by the U.S. military. The former ones from measurements on a mountaintop and the latter in the desert. Figure 2.11 shows the C_n^2 profiles according to each non parametric model detailed in the following.

2.3.1 H-V 5/7

A standard use of the HV model is to set its parameters in order to yield particular values of coherence length (or Fried's seeing parameter r_0) and isoplanatic angle (θ_0). For instance, one can assume values of $A = 1.7 \times 10^{-14} m^{-2/3}$ and $v = 21 m/s$ such that the C_n^2 profile yields a value of coherence length of $5cm$ and isoplanatic angle of $7\mu rad$ ($\lambda = 0.5\mu m$). This is known as the HV-5/7 model. It is a model for which the integrated coherent length and isoplanatic angle values are assumed for nighttime conditions in the field of astronomy (i.e. assuming a vertical path integration and a propagation wavelength of $0.5\mu m$).

2.3.2 H-V Night [17]

Another "HV model" for nighttime use has been developed by Parenti and Sasiela in 1993 for a special use in subtropical climate since the HV model was initially intended for mid-latitude climates. This version of HV was adapted from experiments conducted at Air Force Maui Optical Station. This site, characterized as a "good astronomical site" by the authors, offers nighttime viewing conditions for which the seeing defined as

$$\theta_s = 1.22 \frac{\lambda}{r_0} \quad (2.50)$$

is often better than 0.5 arcsec. The model developed to fit these particular experimental observations is a typical HV profile yielding a 20 cm r_0 and 20 μrad θ_0 for 0.55 μm radiation

at zenith.

$$C_n^2(h) = 8.16 \times 10^{-54} h^{10} e^{\frac{-h}{1000}} + 3.02 \times 10^{-17} e^{\frac{-h}{1500}} + 1.9 \times 10^{-15} e^{\frac{-h}{100}} \quad (2.51)$$

It has to be noted that a standard Bufton wind profile was chosen in that case.

2.3.3 Greenwood [18]

The Greenwood model was developed by D. P. Greenwood in 1976. It is a "nighttime model" suited for mountaintop type of sites originally intended to be used for astronomical imaging. The model relies on data collected for three nights at the ARPA Maui Optical Station (AMOS)

$$C_n^2(h) = [2.2 \times 10^{-13} (h \sin \theta + 10)^{-1.3} + 4.3 \times 10^{-17}] \times e^{-\frac{h \sin \theta}{4000}} \quad (2.52)$$

where θ is the elevation angle.

2.3.4 Gurvich [19, 20]

A phenomenological model proposed by Gurvich et. al. taking into account the strength of the turbulences. As previously explained, in the boundary layer C_n^2 follows a general law described as $C_n^2 \propto h^{-p}$ where p is $4/3$, $2/3$ or 0 for unstable, neutral, or stable atmospheric conditions, respectively. Initially, Four different profiles were developed depending on the estimated value of C_n^2 at the height $h = 2.5m$, thus corresponding to different turbulent regimes ("strong" or "weak"). Later, these analytical expressions were refined thanks to the acquisition of more experimental data. The model developed by Gurvich and Gracheva is descibed by the following expressions, classified according to the turbulence strength. In weak turbulence regime:

$$\begin{aligned} \log_{10} [C_{n \min}^2(h) - 5.19 \times 10^{-16} \times 10^{-0.00086h}] \\ = -18.34 + 2.9 \times 10^{-4}h - 2.84 \times 10^{-8}h^2 + 7.43 \times 10^{-13}h^3 \end{aligned} \quad (2.53)$$

In strong turbulence regime:

$$\begin{aligned} \log_{10} [C_{n \max}^2(h) - 9.5 \times 10^{-14} \times 10^{-0.00209h}] \\ = -14.39 + 1.7 \times 10^{-4}h - 3.48 \times 10^{-8}h^2 + 9.59 \times 10^{-13}h^3 \end{aligned} \quad (2.54)$$

In "average" turbulence regime (i.e. a mean value of the previous profiles):

$$\log_{10} [C_{n \text{ av}}^2(h)] = \frac{1}{2} \{ \log_{10} [C_{n \min}^2(h)] + \log_{10} [C_{n \max}^2(h)] \} \quad (2.55)$$

2.3.5 Submarine Laser Communications Day [21]

The SLC model is one of the first empirical model developed from (averaged) data collected around the AMOS telescope site at the top of MT. Haleakala in Hawaii. It does not incorporate any parametric dependencies other than altitude. It was obtained from fitting experimental data obtained from scintillation measurements, acoustic sounders, aircrafts etc. The C_n^2 values obtained and the median profile related cannot really be applied to sites other than the AMOS site since it is situated in a subtropical climate (i.e high tropopause, 17 km MSL) at the top of a dormant volcano 3 km ASL. A model for nighttime conditions was developed as well.

SLC Daytime

<i>Altitude range</i>	C_n^2	
$h < 18.5m$	1.70×10^{-14}	
$18.5 < h < 240m$	$3.13 \times 10^{-13}/h$	(2.56)
$240 < h < 880m$	1.30×10^{-15}	
$880 < h < 7200m$	$8.87 \times 10^{-7}/h^3$	
$7200 < h < 20000m$	$2.00 \times 10^{-16}/h^{0.5}$	

SLC Nighttime

<i>Altitude range</i>	C_n^2	
$h < 18.5m$	8.40×10^{-15}	
$18.5 < h < 110m$	$2.87 \times 10^{-12}/h^2$	(2.57)
$110 < h < 1500m$	2.5×10^{-16}	
$1500 < h < 7200m$	$8.87 \times 10^{-7}/h^3$	
$7200 < h < 20000m$	$2.00 \times 10^{-16}/h^{0.5}$	

The principal limitation of this non parametric model resides in its mathematical derivation. It was developed using the logarithmic averaging of data and therefore represents in fact the median of the values instead of their mean.

2.3.6 AFGL AMOS (Air Force's Maui Optical Station) model [21]

The AFGL AMOS constitutes simply an improvement of the SLC model. More precisely, based on a series of high-resolution balloon measurements from the top of Mt. Haleakala, a refinement of the nighttime SLC model was developed for the AMOS Observatory. The model was developed by piecewise fitting the arithmetic average of a large number of measurements under a wide range of meteorological conditions. The fit models the arithmetic average C_n^2 and not the logarithmic average and therefore will yield more realistic

NIGHT		SUNRISE		DAY		
3.052<h<5.2	h>5.2	3.052< h<5.78	h>5.78	3.052<h<3.54	3.54<h<5.1	h>5.1
a=-12.412	a=-17.1273	a=-14.0245	a=-16.7545	a=0.0482	a=-17.4778	a=-16.5589
b=-0.4713	b=-0.0301	b=-0.4809	b=0.0259	b=-2.3416	b=0.0320	b=-0.1424
c=-0.0906	c=-0.0010	c=-0.0144	c=-0.0022	c=-0.7211	c=0.0078	c=0.0030
	d=0.5061		d=-0.6693		d=1.5066	d=1.5694
	e=15.0866		e=7.0330		e=4.4603	e=16.6300
	f=3.2977		f=2.8558		f=0.0968	f=4.8757

Table 2.3: Regression coefficient values (AFGL AMOS model)

values for moments such as isoplanatic angle and scintillation.

$$\log_{10}(C_n^2) = a + bh + ch^2 \quad \text{Log quadratic: applicable to the boundary layer}$$

$$\log_{10}(C_n^2) = a + bh + ch^2 + de^{-0.5\left[\frac{(h-e)}{f}\right]^2} \quad \text{Log quadratic with gaussian: applicable above the boundary layer} \quad (2.58)$$

where h is the altitude above mean sea level (MSL) in km. The coefficients are given by the following table 2.3.

2.3.7 CLEAR (Critical Laser Enhancing Atmospheric Research) model [22]

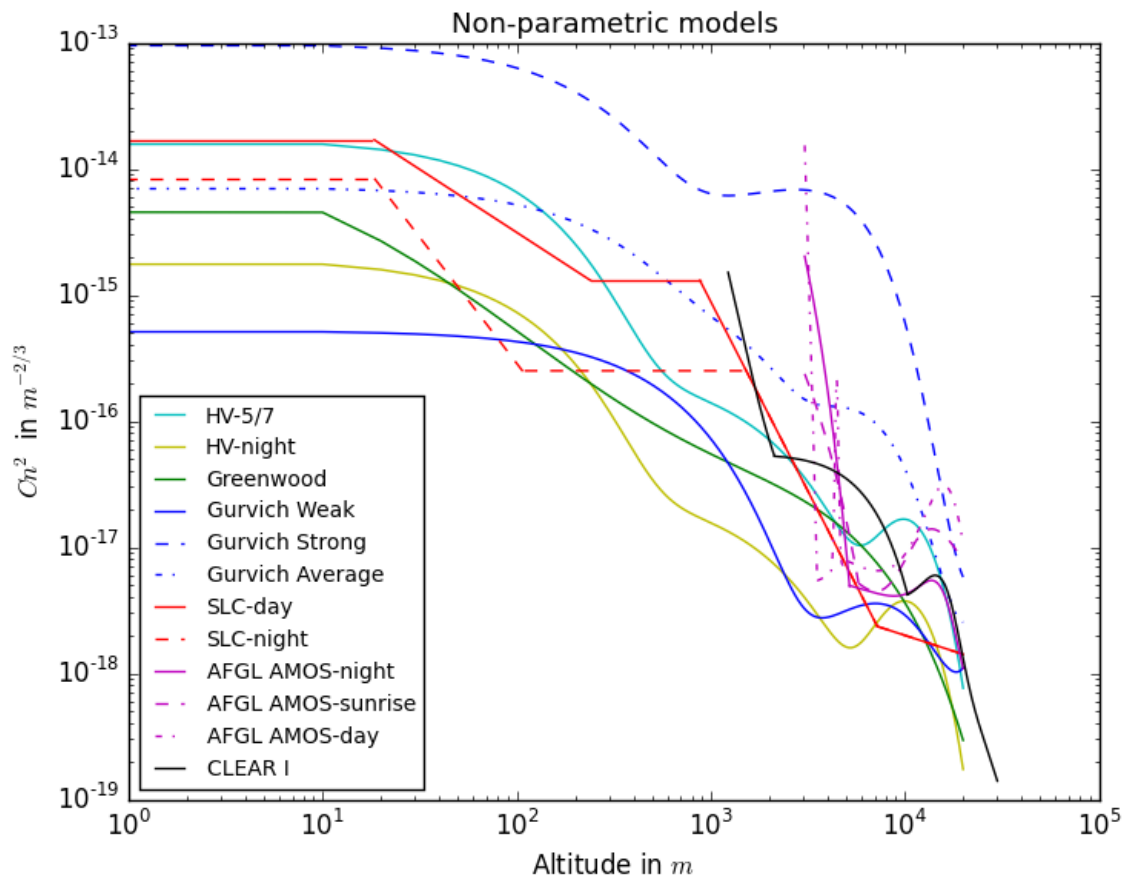
The CLEAR I model has been developed in way similar of that of the AFGL AMOS but for the New Mexico desert in the summer.

$$\log_{10}(C_n^2) = -10.7025 - 4.3507h + 0.8141h^2 \quad \text{for } 1.23 < h < 2.13$$

$$\log_{10}(C_n^2) = -16.2897 + 0.0335h - 0.0134h^2 \quad \text{for } 2.13 < h < 10.34$$

$$\log_{10}(C_n^2) = -17.0577 - 0.0449h - 0.0005h^2 + 0.6181e^{-0.5\left[\frac{(h-15.5617)}{3.4666}\right]^2} \quad \text{for } 10.34 < h < 30 \quad (2.59)$$

where h is the altitude above mean sea level (MSL) in km. The CLEAR I model was developed in 1984. In 1985 two other measurements campaigns were conducted at the White Sands Missile Range facilities.

Figure 2.11: Non-parametric C_n^2 profiles

	Model	Expression	Input Parameter(s)	References
Parametric Models	HV	$C_n^2(h) = 0.00594(v/27)^2(10^{-5}h)^{10}e^{-\frac{h}{1000}}$ $+ 2.7 \times 10^{-16}e^{-\frac{h}{1500}}$ $+ Ae^{-\frac{h}{100}}$	$A = C_n^2(0)$ and v the high altitude rms wind speed	[12, 21]
	HAP	$C_n^2(h) = M \left[0.00594(v/27)^2(10^{-5}(h+h_s))^{10}e^{-\frac{(h+h_s)}{1000}} \right.$ $\left. + 2.7 \times 10^{-16}e^{-\frac{(h+h_s)}{1500}} \right]$ $+ C_n^2(h_0) \left(\frac{h_0}{h} \right)^p$	$h_0, h_s, C_n^2(h_0), M$ and p	[5, 6, 4, 7]
	ARL Model	$X_K(h) = \log_{10}(C_T^2) = \log_{10}(C_{TS}^2) + 0.775 \exp \left[-\frac{(h - 0.95h_i)^2}{2(h_i/7)^2} \right]$ $+ \left[\frac{1}{3} + \frac{4}{3} \log_{10} \left(\frac{h}{h_i} \right) \right] \sigma \left[\frac{h_i - h}{h_i/8} \right]$ $N_K(h) = X_K(1000h) + \log[A^2 P^2 / T^4]$ $N_{mu}(h) = N_{mid} \sigma \left[\frac{h - 7.8}{2.4} \right] + N_{upper}(h) \sigma \left[\frac{7.8 - h}{2.4} \right]$ $- 1.3 \sigma \left[\frac{h - 9.2}{1.6} \right] \sigma \left[\frac{9.2 - h}{1.6} \right]$ $N(h) = \sigma(h - 7)N_{mu}(h) + \sigma(7 - h)N_K(h)$	C_n^2 , wind speed, temperature values at reference height h_r ; roughness length, daytime/nighttime	[4]
	Aeronomy Laboratory Model NOAA (Free atmosphere only)	$C_n^2 = 2.8M_0^2 \int_{L_{min}}^{L_{max}} dL p_L L^{4/3} \int_0^\infty dS p_S \int_{-\infty}^S dN^2 p_N (N^2)^2$	Mean values of P, T, q, q', N^2 and S	[9, 10]
	AFGL Radiosonde Model (Free atmosphere only)	$C_n^2(h) = 2.8(0.1)^{4/3} M(h)^2 10^{Y(h)}$ $Y = 1.64 + 42.0S_{raw} \quad \text{Troposphere}$ $Y = 0.51 + 50.0S_{raw} \quad \text{Stratosphere}$	P and T and S_{raw} directly from radiosondes	[11]
	PAMELA (Boundary Layer only)	$C_n^2 = \frac{bK_h}{\epsilon^{1/3}} \left(\frac{\partial n}{\partial h} \right)^2$	Latitude, longitude, date, time of day, percent cloud cover, and terrain type, as well as a single measurement (or estimate) of atmospheric temperature, pressure and wind speed at the desired height h	[13, 14, 12]
	Sadot and Kopeika Models (Boundary Layer only)	$C_n^2 = A_1W + B_1T + C_1RH + C_1RH^2 + C_3RH^3$ $+ D_1WS + D_2WS^2 + D_3WS^3$ $+ E_1flux + F_1TCSA + F_2TCSA^2 + G$	$W, T, RH, WS, flux,$ and $TCSA$	[15, 16]

Non-parametric Models	HV-Night	$C_n^2(h) = 8.16 \times 10^{-54} h^{10} e^{\frac{-h}{1000}}$ $+ 3.02 \times 10^{-17} e^{\frac{-h}{1500}}$ $+ 1.9 \times 10^{-15} e^{\frac{-h}{100}}$	[17]										
	Greenwood	$C_n^2(h) = [2.2 \times 10^{-13} (h \sin \theta + 10)^{-1.3} + 4.3 \times 10^{-17}] \times e^{-\frac{z \sin \theta}{4000}}$	[18]										
	Gurvich	<p><i>Weak turbulence</i></p> $\log_{10} [C_n^2 \min(h) - 5.19 \times 10^{-16} \times 10^{-0.00086h}]$ $= -18.34 + 2.9 \times 10^{-4} h - 2.84 \times 10^{-8} h^2 + 7.43 \times 10^{-13} h^3$ <p><i>Strong turbulence</i></p> $\log_{10} [C_n^2 \max(h) - 9.5 \times 10^{-14} \times 10^{-0.00209h}]$ $= -14.39 + 1.7 \times 10^{-4} h - 3.48 \times 10^{-8} h^2 + 9.59 \times 10^{-13} h^3$ <p><i>Average turbulence</i></p> $\log_{10} [C_n^2 \text{av}(h)]$ $= \frac{1}{2} \{ \log_{10} [C_n^2 \min(h)] + \log_{10} [C_n^2 \max(h)] \}$	[19, 20]										
	Submarine Laser Communications Day	<p><i>Altitude range</i></p> <table style="margin-left: auto; margin-right: auto;"> <tr> <td>$h < 18.5m$</td> <td>1.70×10^{-14}</td> </tr> <tr> <td>$18.5 < h < 240m$</td> <td>$3.13 \times 10^{-13}/h$</td> </tr> <tr> <td>$240 < h < 880m$</td> <td>1.30×10^{-15}</td> </tr> <tr> <td>$880 < h < 7200m$</td> <td>$8.87 \times 10^{-7}/h^3$</td> </tr> <tr> <td>$7200 < h < 20000m$</td> <td>$2.00 \times 10^{-16}/h^{0.5}$</td> </tr> </table>	$h < 18.5m$	1.70×10^{-14}	$18.5 < h < 240m$	$3.13 \times 10^{-13}/h$	$240 < h < 880m$	1.30×10^{-15}	$880 < h < 7200m$	$8.87 \times 10^{-7}/h^3$	$7200 < h < 20000m$	$2.00 \times 10^{-16}/h^{0.5}$	[21]
	$h < 18.5m$	1.70×10^{-14}											
	$18.5 < h < 240m$	$3.13 \times 10^{-13}/h$											
$240 < h < 880m$	1.30×10^{-15}												
$880 < h < 7200m$	$8.87 \times 10^{-7}/h^3$												
$7200 < h < 20000m$	$2.00 \times 10^{-16}/h^{0.5}$												
AFGL AMOS	<p><i>Log quadratic : applicable to the boundary layer</i></p> $\log_{10}(C_n^2) = a + bh + ch^2$ <p><i>Log quadratic with gaussian : applicable above the boundary layer</i></p> $\log_{10}(C_n^2) = a + -bh + ch^2 + de^{-0.5 \left[\frac{(h-e)}{f} \right]^2}$	[21]											
CLEAR I	<p>for $1.23 < h < 2.13$</p> $\log_{10}(C_n^2) = -10.7025 - 4.3507h + 0.8141h^2$ <p>for $2.13 < h < 10.34$</p> $\log_{10}(C_n^2) = -16.2897 + 0.0335h - 0.0134h^2$ <p>for $10.34 < h < 30$</p> $\log_{10}(C_n^2) = -17.0577 - 0.0449h - 0.0005h^2$ $+ 0.6181e^{-0.5 \left[\frac{(h-15.5617)}{3.4666} \right]^2}$	[22]											

Table 2.4: C_n^2 profile models synthesis

2.4 Characteristic Scales Models

The characteristic scales define the inertial domain that is, in the statistical description of atmospheric turbulence, the domain within which the turbulence is fully developed. In the turbulent flow, this domain is limited by the size of largest eddies L_0 (of the order of several tens of meters) and the size of the smallest eddies l_0 (of the order of several millimeters). Considering turbulence spectrum models, the influence of the former raises at low spatial frequency therefore inducing non negligible seeing limitations for (future) large aperture telescopes. The inner scale of turbulence, being the scale at which energy is dissipated by atmospheric turbulence convection, is of fundamental importance in determining surface fluxes of heat and momentum.

Several measurements techniques allow to infer the values of these scales. The Generalized Seeing Monitor (GSM) uses the angle of arrival fluctuations of the wavefront to determine L_0 . The outer scale can also be deduced from interferometric measurements and adaptive optic systems data. The inner scale is usually determined using either angle of arrival fluctuations or intensity fluctuations measurements or both.

However very few profile models of the characteristic scales exist as compared to C_n^2 models. Tatarskii showed in [33] that the inner scale is given by

$$l_0 = 7.4 \left(\frac{\nu^3}{\varepsilon} \right)^{1/4} \quad (2.60)$$

where ν is the kinematic viscosity.

The whole difficulty in determining l_0 then resides in finding the average dissipation rate of the turbulent energy per unit mass of the "fluid", ε (in units of m^2/s^3). This inverse dependence of inner scale on the average rate of dissipation ε shows that strong turbulence has smaller inner scales and weak turbulence has larger inner scales. On the other hand, the outer scale L_0 is proportional to $\varepsilon^{1/2}$ therefore, unlike the inner scale, L_0 increases and decreases directly with the strength of turbulence[23].

2.4.1 Inner-scale Models

The inner scale of turbulence, being the scale at which energy is dissipated by atmospheric turbulence convection, is of fundamental importance in determining surface fluxes of heat and momentum. Two types of method for determining l_0 can be classified depending on whether phase or amplitude related quantities are needed for their application. The most standards methods are based on laser scintillation (i.e. amplitude related) applicable for path length of a hundred meters or more whereas for shorter path lengths, phase related methods are necessary [35].

However, to measure the inner scale on intermediate distance, both methods can be combined in a "mixed method" [36] using scintillation measurements as well as angle of arrival measurements from which Consortini et. al. derived expressions for the inner-scale for plane as well as spherical waves. These formulas are summarized in table 2.5 and depend on the mean square of angle of arrival fluctuations $\langle \alpha^2 \rangle$, the normalized mean square

of the intensity fluctuations σ_I^2 , L the path length and λ the wave length.

	Plane waves	Spherical waves
$L \ll \frac{l_0^2}{\lambda}$	$l_0 = 1.97L \left(\frac{\langle \alpha^2 \rangle}{\sigma_I^2} \right)^{1/2}$	$l_0 = 1.08L \left(\frac{\langle \alpha^2 \rangle}{\sigma_I^2} \right)^{1/2}$
$L \gg \frac{l_0^2}{\lambda}$	$l_0 = 2.37k^{-7/2}L^{-5/2} \left(\frac{\sigma_I^2}{\langle \alpha^2 \rangle} \right)^3$	$l_0 = 1.37k^{-7/2}L^{-5/2} \left(\frac{\sigma_I^2}{\langle \alpha^2 \rangle} \right)^3$

Table 2.5: Inner-scale expressions for spherical and plane waves

Another model of l_0 can be derived directly from Eq. **2.60** if one is able to estimate the rate of dissipation of turbulent kinetic energy ε and the kinematic viscosity ν . This can be achieved by using measurements of the transverse velocity structure functions made for instance with vertically spaced hot-wire anemometer probes as Ochs and Hill did[37]. The measured transverse-velocity structure function is divided by the two-thirds power of the spacing between the hot-wire anemometers; this gives the transverse-velocity structure parameter:

$$C_{V_T}^2 = \frac{8}{3}\varepsilon^{2/3} \quad (2.61)$$

The kinematic viscosity is given by

$$\nu = \frac{\mu}{\rho} \quad (2.62)$$

where μ is the coefficient of viscosity of air and ρ is the mass density of air. The former is obtained using:

$$\mu = \frac{\beta T^{3/2}}{T + S} \quad (2.63)$$

where T is the absolute temperature, β is a constant ($1.458 \times 10^{-6} kg \cdot sec^{-1} \cdot K^{-1/2}$) and S is Sutherland's constant (110.4 K). To obtain ρ from known temperature and pressure one can use the ideal gas law

$$\rho = \frac{M_0 P}{RT} \quad (2.64)$$

where M_0 is the gram molecular weight of air, P is atmospheric pressure and R is the universal gas constant. Combining Eq. **2.61** to Eq. **2.64** yields the following expression of the inner-scale:

$$l_0 = 10.7 \left(\frac{\beta R}{M_0} \right)^{3/4} \frac{T^{15/8}}{[(T + S)P]^{3/4}} (C_{V_T}^2)^{-3/8} \quad (2.65)$$

However, Ochs and Hill conducted these measurements at 1.5m above ground only. Later, Eaton and Nastrom [38], relying on Eq. **2.60** as a starting point as well, developed a $l_0(h)$ model extending from 5 to 20km (MSL) using VHF radar observations to estimate ε . These values were based on widths of the Doppler spectra which were corrected for beam broadening, shear broadening, and gravity wave effects through the parameter σ_{turb}^2 :

$$\varepsilon = A^{-3/2} N \sigma_{turb}^2 \quad (2.66)$$

where $A^{-3/2} = 1.6$ is a Kolmogorov constant and N is the Brunt-Vaisala frequency. The kinematic viscosity (Eq. 2.62) was calculated by choosing a value of 2×10^{-5} N for μ and standard atmosphere values at $30^\circ N$ were used for the profile calculations of ρ . The inner-scale was found to range from about 1cm at 5km to about 7 cm at 19km altitude. More details about this profile features (especially seasonal variations since the VHF data was acquired during 5 years) can be found in the original article.

2.4.2 Outer-scale Models

Beland and Brown developed in 1988 a deterministic temperature model for the optical turbulence in the troposphere (i.e. from 17 to 30 km MSL), using thermosondes data [39]. L_0 was evaluated as the fitting parameter for the C_n^2 measurements using Tatarskii's equation (Eq. 2.38 for instance with $L = L_0$), as a result the following average L_0 estimation was found:

$$L_0(h) = 0.307 - 0.0324(h - 17) + 0.00167(h - 17)^2 + 0.000476(h - 17)^3 \quad (2.67)$$

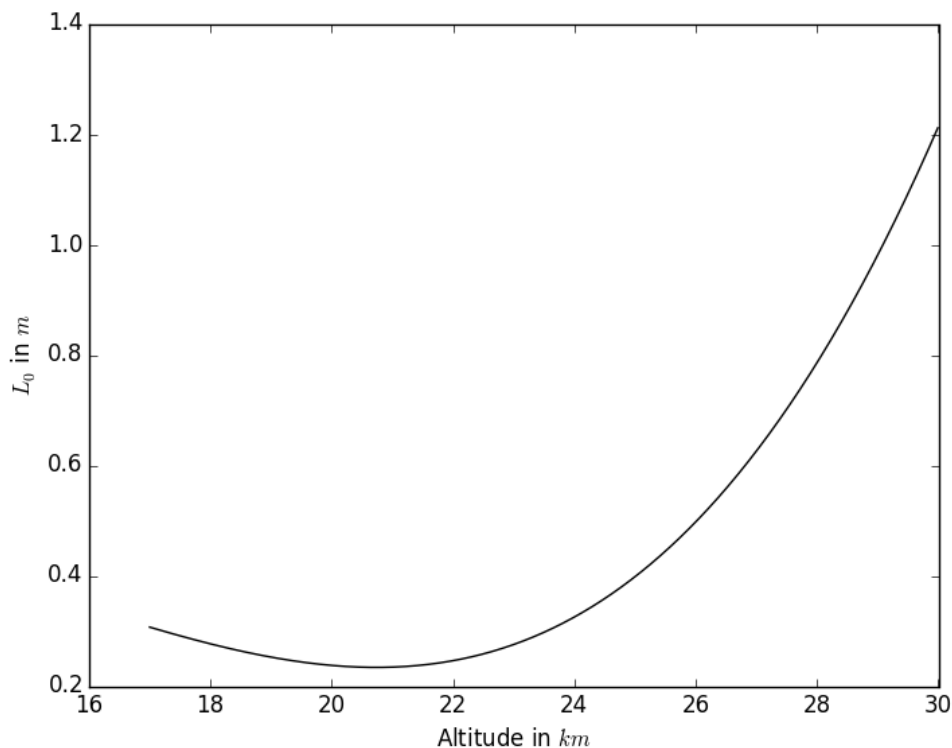


Figure 2.12: L_0 profile determined by Beland and Brown

This average fit shows that L_0 is about 0.25m and approximatively constant from 17 to 23km MSL and then increases monotonically to about 1m at 30 km MSL.

Coulman et. al. calculated L_0 from values of C_n^2 obtained from spatio-angular correlation measurements of stellar scintillation (SCIDAR) [40]. The starting point of the model is once more Tatarskii's equation from which, given the necessary meteorological radiosonde data, L_0 can be determined. Simultaneous measurements of C_n^2 (using SCIDAR) and M^2 (using radiosondes) profiles at a given site were done. Several campaigns were conducted in France and U.S.A. Examining the correlation between C_n^2 and M^2 in light of Tatarskii's relationship the authors obtained, at first, a cloud of points not justifying to fit any kind of regression expression. However it was noticed that a well-marked upper limit to the data existed suggesting that L_0 does not exceed approximatively 5m. Moreover, some of the variance observed were attributed to a dependence of L_0 on altitude. Therefore the data was segregated into sets which relate to 1-km thick slices of atmosphere in the 2-17 km range. A simple analytic relationship was then fitted yielding the following variation of the outer-scale with altitude:

$$L_0(h) = \frac{4}{1 + \left(\frac{h-8500}{2500}\right)^2} \quad (2.68)$$

The same experiments were later conducted at the European Southern Observatory, La Silla, Chile giving an altitude dependance $L_0(h)$ not so different from Eq. 2.68:

$$L_0(h) = \frac{5}{1 + \left(\frac{h-7500}{2000}\right)^2} \quad (2.69)$$

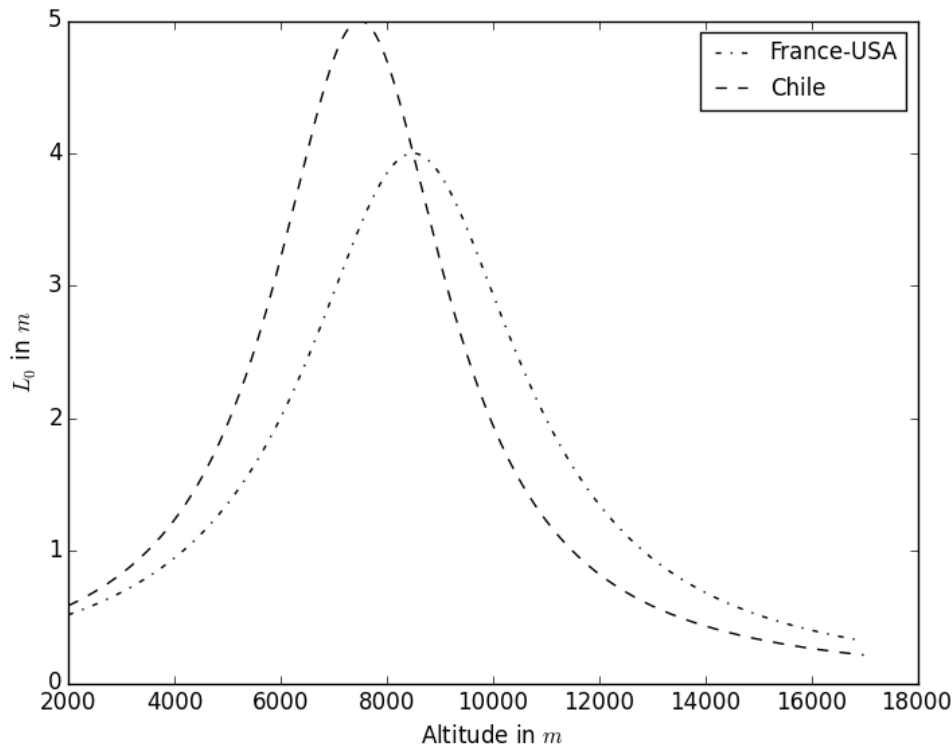


Figure 2.13: L_0 profiles determined by Coulman et. al. from measurements performed in France-USA and Chile

Using instrumented meteorological balloons, Abahamid et. al. [41] extended the L_0 profiles to the ground. In the boundary layer, their experimental results fitted well the following function as well as with the Coulman profile:

$$L_0(h) = 3.78h^{-0.27} \quad (2.70)$$

Notice that this profile cannot, in reality extend completely to the ground as L_0 would become infinite. Instead it is commonly assumed in the literature that up to 25m the outer scale follows the following Tatarski relationship:

$$L_0 = Kh \quad (2.71)$$

where K is the vonKarman constant, roughly equal to 0.4. Previously to Beland and Brown and Coulman et. al. models, Barat and Bertin used in situ simultaneous observations of the turbulent and velocity fields in the stratosphere in order to obtain an estimation of ε [42]. Their results shown that the outer length values range from 10 to 50 m. These results are obviously much bigger than the Beland and Coulman's ones and one interpretation is that L_0 calculated in the first cases represent volume averaged values. Using the observations that about 5 percent of any given volume is turbulent, these L_0 values should be scaled up a factor 20 to represent the outer lengths observed by Barat.

Eaton and Nastrom in [38] also provided a method to determine $L_0(h)$ from the same VHF observations used for the $l_0(h)$ profile. The eddy dissipation rate (ε) is also required as well as wind shear measurements. The outer-scale was estimated using the following relationship provided by Tatarskii in [33]:

$$L_0(h) = \varepsilon^{1/2} \left| \frac{\partial \bar{\mathbf{u}}_{\text{horizontal}}}{\partial h} \right|^{-3/2} \quad (2.72)$$

Where $\bar{\mathbf{u}}_{\text{horizontal}}$ is the horizontal wind speed. Once more, for more details about this profile features the reader should refer to the original article. The general trend in $L_0(h)$ consists in a decrease from about 60m at 5 km altitude for all seasons to a range of 12-60m (depending on season) at 15km and finally an increase to 22m at 19km altitude.

2.4.3 Characteristic scales determined from scintillation measurements (using the HAP model)

Andrews et. al. [8, 7, 5], in the framework of the HAP C_n^2 model development, inferred as well inner and outer scales of turbulence from the same scintillation measurements. Their models for l_0 and L_0 are simply based on Coulman's empirical formula, however slightly modified:

$$L_0(h) = \frac{10L_0(h_0)}{1 + \left(\frac{h-7500}{2500}\right)^2} \quad (2.73)$$

where $L_0(h_0)$ is the outer scale at the height of the instruments. Their modification essentially limits the outer scale to $10L_0(h_0)$ m in the vertical direction. The choice of such a parameter seems arbitrary, even more if one considers that in a layered atmosphere and at high altitudes, the outer scale along a slant path can be significantly larger than $10L_0(h_0)$ m particularly at low elevation angle.

Concerning the inner scale, Andrews et. al. chose to assume that its profile follows the general behaviour of $L_0(h)$ and therefore wrote:

$$l_0(h) = \frac{10l_0(h_0)}{1 + \left(\frac{h-7500}{2500}\right)^2} \quad (2.74)$$

where $l_0(h_0)$ is the inner scale at the height of the instruments. The whole problem is therefore related to obtaining the correct values of the characteristic scales at the height of the instruments. To do so it is necessary to calculate the scintillation index with the inclusion of both inner and outer scales as (Chapter 9, Eq.(83) in [23]):

$$\sigma_I^2(L) = \exp \left[\sigma_{lnX}^2(l_0) - \sigma_{lnX}^2(L_0) + \frac{0.51\sigma_{SP}^2}{\left(1 + 0.69\sigma_{SP}^{12/5}\right)^{5/6}} \right] - 1 \quad (2.75)$$

where $\sigma_{lnX}^2(l_0)$ and $\sigma_{lnX}^2(L_0)$ are large scale irradiance fluctuations and σ_{SP}^2 is the weak fluctuation Rytov expression for the spherical wave scintillation index with inner scale.

This model is based on the modified atmospheric spectrum given by:

$$\Phi_n(\kappa, h) = 0.33C_n^2(h)\kappa^{-11/3} \left[1 + 1.802 \left(\frac{\kappa}{\kappa_l(h)} \right) - 0.254 \left(\frac{\kappa}{\kappa_l(h)} \right)^{7/6} \right] \underbrace{\left[1 - e^{-\frac{\kappa^2}{\kappa_0^2(h)}} \right]}_{\text{Outer Scale Term}} \underbrace{e^{-\frac{\kappa^2}{\kappa_l^2(h)}}}_{\text{Inner Scale Term}} \quad (2.76)$$

with

$$0 \leq \kappa < \infty, \quad \kappa_l(h) = \frac{3.3}{l_0(h)}, \quad \kappa_0(h) = \frac{8\pi}{L_0(h)} \text{ or } \frac{2\pi}{L_0(h)}$$

The calculation of the SI necessitates the use of the path-average C_n^2 , path-average inner and outer scales values in the modified spectrum. Comparing the results with that produced by the HAP $C_n^2(h)$ model together with the expression of $L_0(h)$ and $l_0(h)$, the ground level values of inner and outer scales can be estimated.

2.5 Conclusion - Selected Models

The bibliographic work regarding the status quo of C_n^2 profiles led to the first conclusion that a primary characteristic differentiate all the models in two categories. Parametric models, depending on a set of input parameters and non-parametric models based solely on site measurements. The former present the advantage to be by definition applicable to different sites and atmospheric conditions in some extent. The latter may be used on sites and for conditions highly similar to the ones they were originally developed for. Such a transposition would need to be done with a lot of caution. Therefore it was decided to select only parametric models.

Only three of them describe the evolution of C_n^2 in the whole atmosphere. The HV model is the most commonly used one. Although some minor modifications can be undertaken to render it more realistic (e.g. inclusion of additional terms for describing additional characteristic layers of turbulence) it presents the major default of being erroneous when describing the C_n^2 behavior in the boundary layer. The HAP model, consisting in a highly enhanced version of the HV model, presents a corrected description of the C_n^2 behavior in the boundary layer. Moreover it includes the effects of a diurnal evolution of the turbulence near the ground and high altitude background turbulence. It has nevertheless the default of necessitating an estimation of C_n^2 at a reference level near the ground.

The ARL model presents a realistic treatment of the surface layer turbulence based on MOST, constituting a landmark of modern micrometeorology, for which a nighttime/daytime differentiation exists. The inputs parameters to the surface layer model establish the inputs for the whole model. The boundary layer treatment for daytime conditions is based on several measurements campaigns undertaken in desert regions (namely the yearly variations of the depth of the boundary layer at White Sands). It is therefore probably best suited for applications in such regions. An equivalent relationship does not exist for nighttime conditions. Therefore the behavior of $C_n^2(h)$ in the surface layer is simply prolonged in the boundary layer. This is highly questionable and the validity of such a profile

is argued by Tosfted et al themselves. Finally the free atmosphere layer is described by a non parametric model, an adaptation of the CLEAR I profile. Nevertheless the ARL model present an interesting example of how one could link different profiles, describing different atmospheric layers, in order to develop an average profile adapted to specific requirements (for instance the authors of the ARL model were asked to develop a profile in the framework of wargaming application in desert regions focusing on the C_n^2 behavior at a low altitude).

Chapter 3

SELECTED MODELS - TESTS AND DISCUSSION

In order to assess the realism, applicability, advantages and drawbacks of the parametric models pre-selected, their input parameters were in a first step, varied for estimating the impact of said parameters on the average profile generated. The characteristic channel parameters that are the Fried parameter (r_0) and the scintillation index (SI) were computed for each one of these variations and for different elevation angles so that their effects could be quantified in a practical perspective. This step highlighted serious defaults in the ARL model. The remainder of the analysis focused therefore on the HAP model compared to the HV model. The model profiles were compared to experimental profiles obtained from radiosonde data acquired at the Izana Observatory. The computations of the channel parameters r_0 and SI were compared for the cases of the HAP and the HV models to data acquired during the KIODO (Klari's Optical Downlink to Oberpfaffenhofen) experiment that took place in 2006. The HAP profile generated parameters that were closer to the experimental data than the parameters generated by the HV model. Finally, a practical implementation of the HAP model is given in section 3.5.

3.1 HAP computations

Three parameters determine the HAP profile.

The power law parameter, depending on the local time through the temporal hour empirical relationship 2.9 describing the C_n^2 variations in the boundary layer. Its impact can be seen on figure 3.1 (b). Because this parameter depends on temporal considerations, according to the time of the day, not only the power law behavior as a function of altitude changes but as well does the ground value of C_n^2 . In other words, it would not make sense if one chose a power law parameter corresponding to nighttime conditions (e.g. $p = 0.67$) and a value of C_n^2 at ground level of $10^{-13} m^{-2/3}$ corresponding to highly unstable atmospheric conditions (i.e. daytime conditions).

Figure 3.1 (a) presents the changes in the HAP profile with respect to the variations of the input parameter M , the random background turbulence. This parameter is said to have a sensitive effect on the profile from and above 1 km according to Andrews. However one can see that in fact, a noticeable effect occurs at much lower altitude (about 100 m) when varying it.

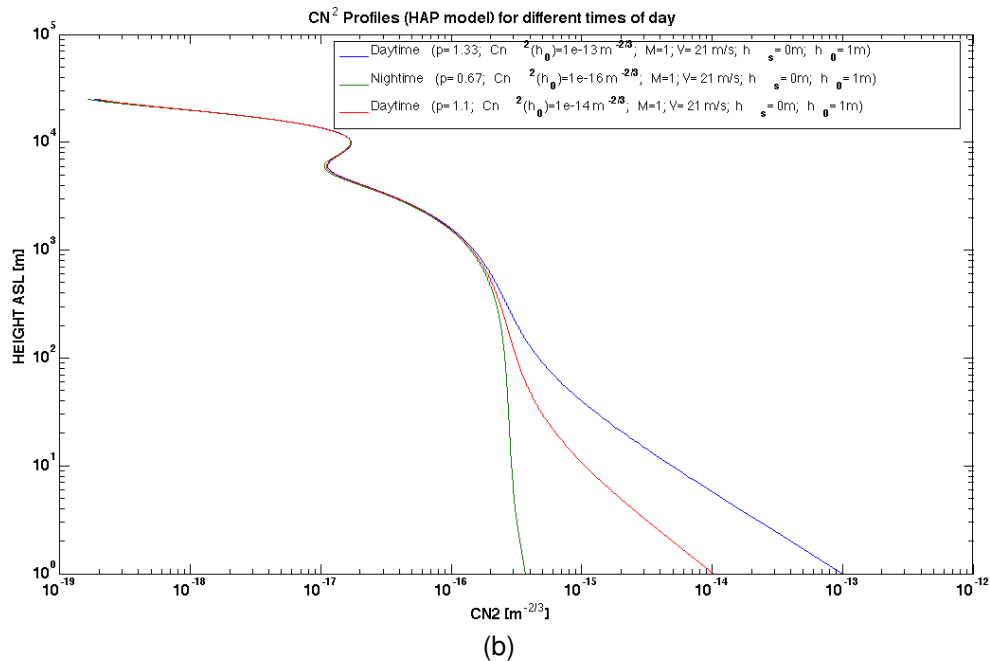
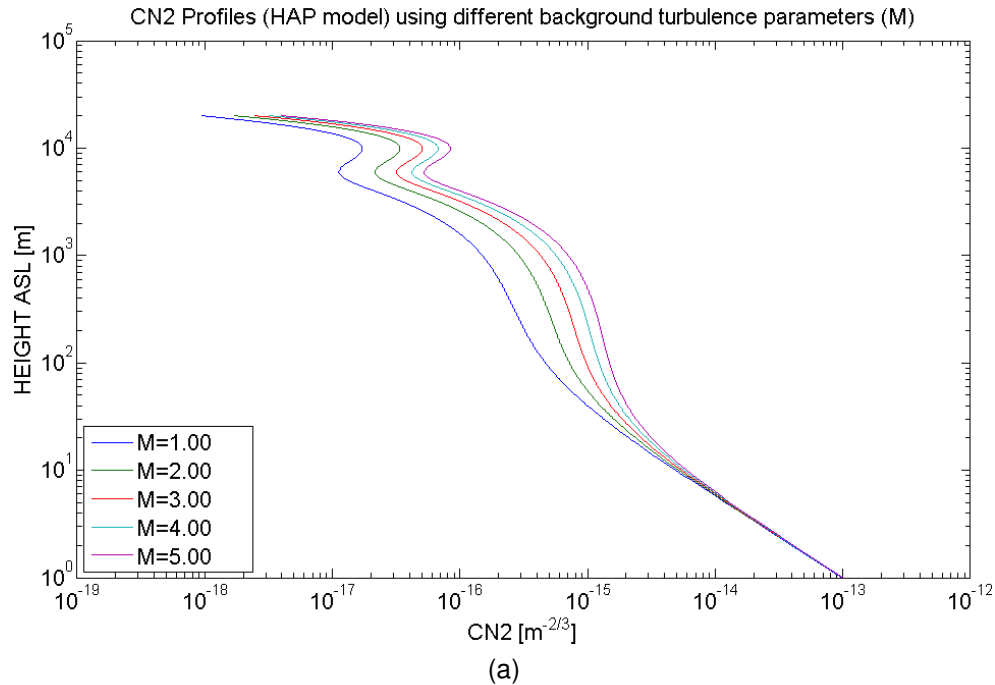
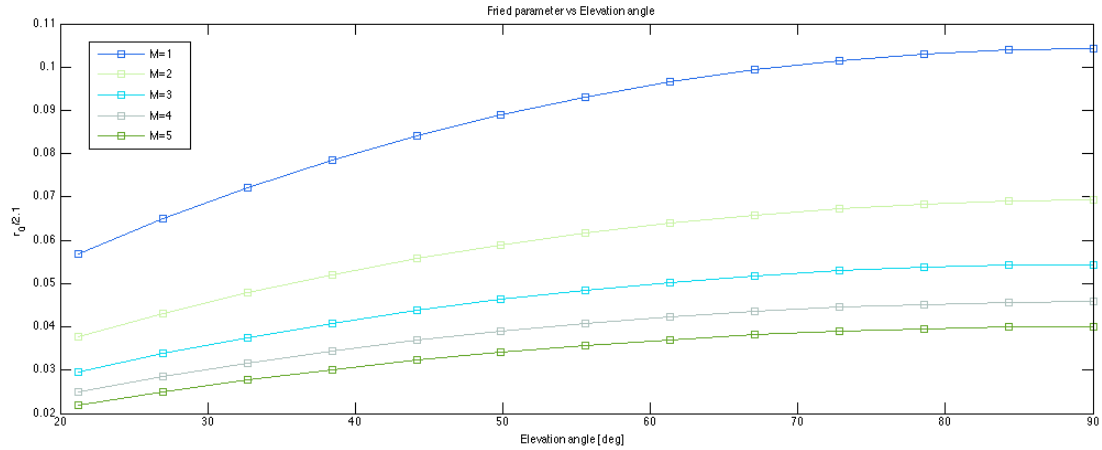
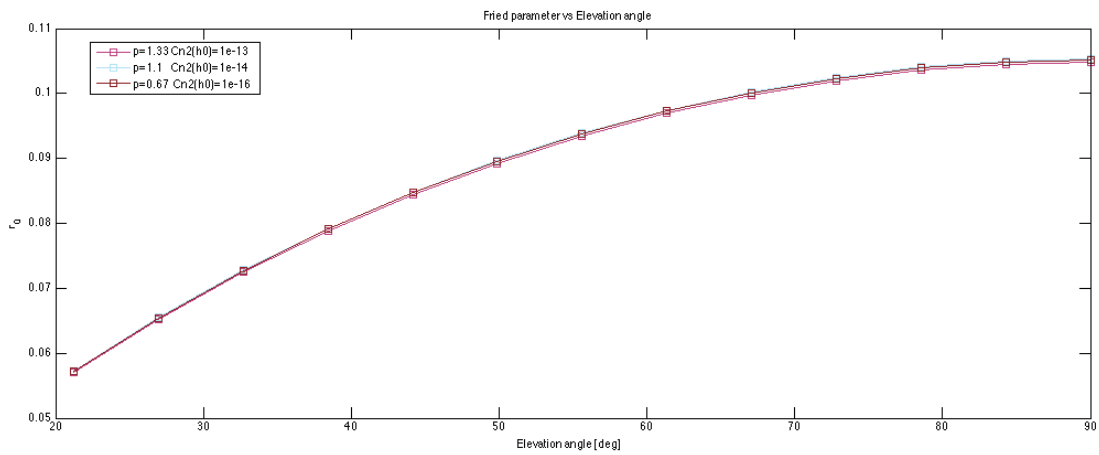


Figure 3.1: Effect of the background random turbulence parameter M on the HAP profile; Three HAP profiles at different time of the day (b)

Figure 3.2 and figure 3.3 present the computations of the Fried parameters and the scintillation indices given by Eq. 1.16 and Eq. 1.23 for the input parameters cases corresponding to figure 3.1.



(a)



(b)

Figure 3.2: Fried parameters computed using the HAP profiles corresponding to different cases of (a) input parameter M and (b) input parameter p

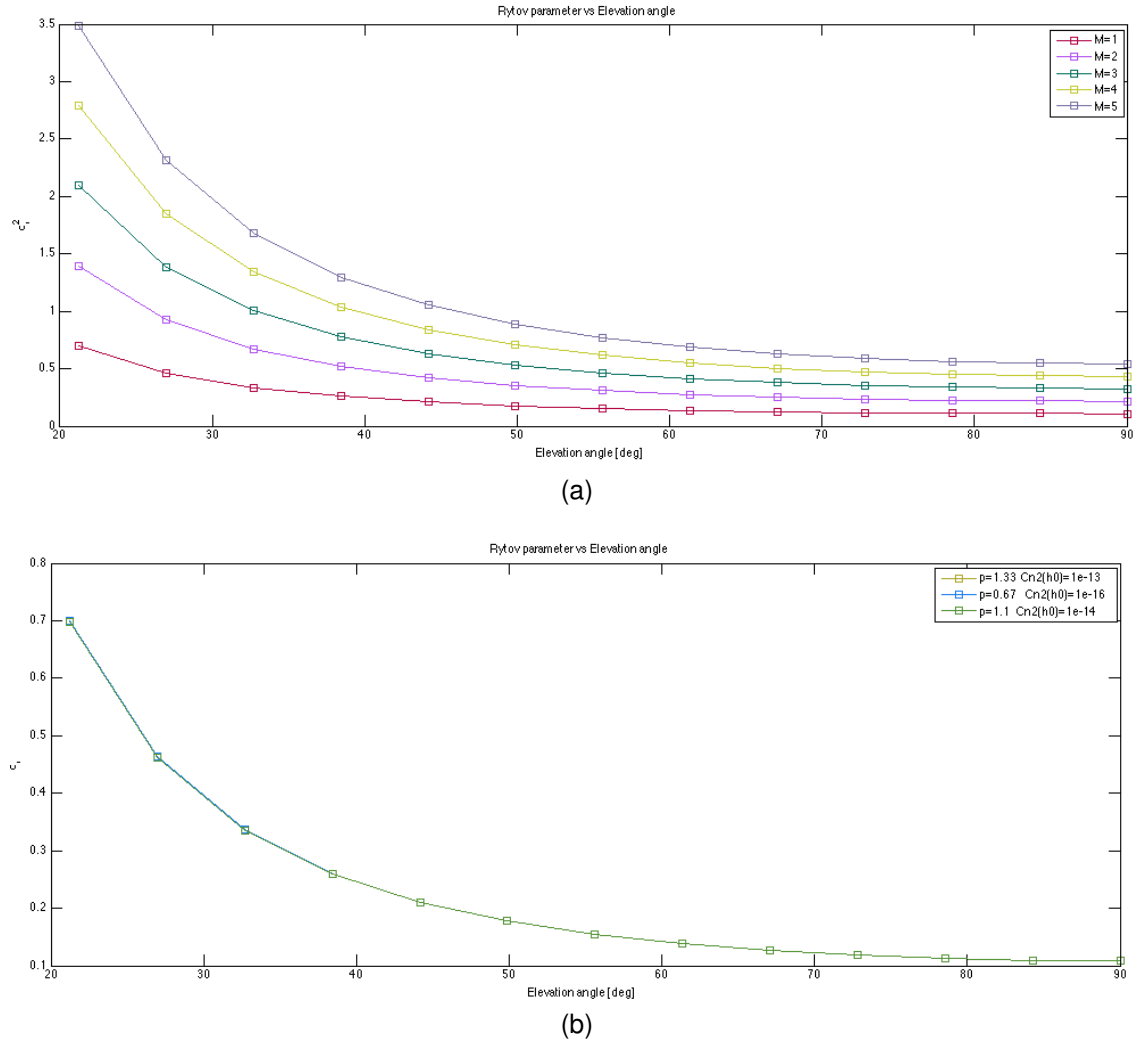


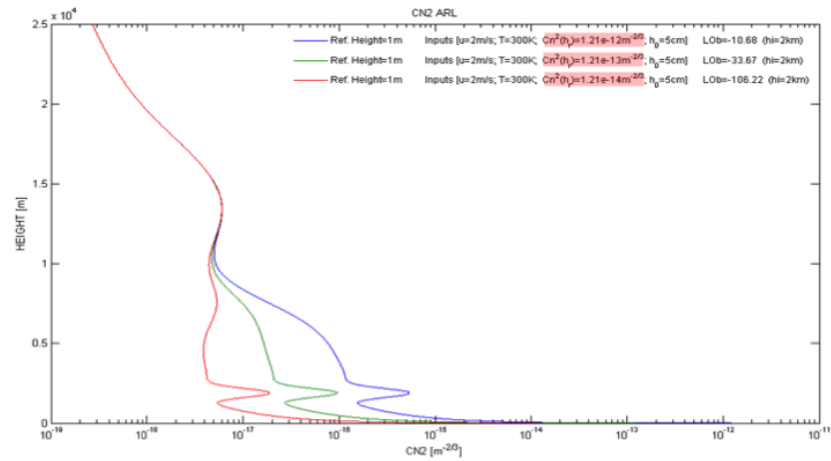
Figure 3.3: Scintillation indices computed using the HAP profiles corresponding to different cases of (a) input parameter M and (b) input parameter p

The choosing of the appropriate random background turbulence parameter can have an important effect on both channel parameters computations. Whereas the variations in the combination of the power law and C_n^2 value on the ground inputs have an almost unnoticeable effect on the Fried parameter and none on the scintillation index computations. This

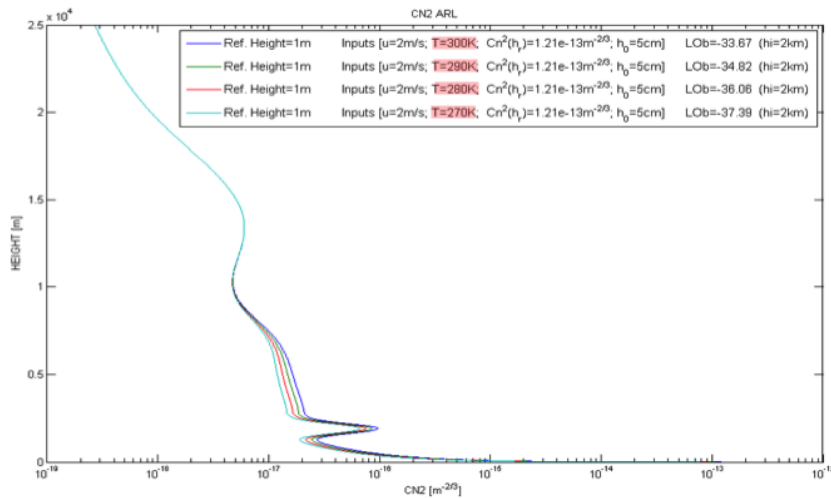
Because of the different weighting functions involved, $r_0(h)$ will tend to be affected by the turbulence closest to the receiver (i.e. in the case of a downlink, closest to the ground). On the other hand, systems affected most by scintillation will be most impacted by turbulence near the center of the path and the end. However the differences in the profiles corresponding to different cases of p inputs are located in the first 100m. The profiles are almost identical above this height and up to 20 km. This explains the similarity in the Fried parameters obtained.

3.2 ARL computations

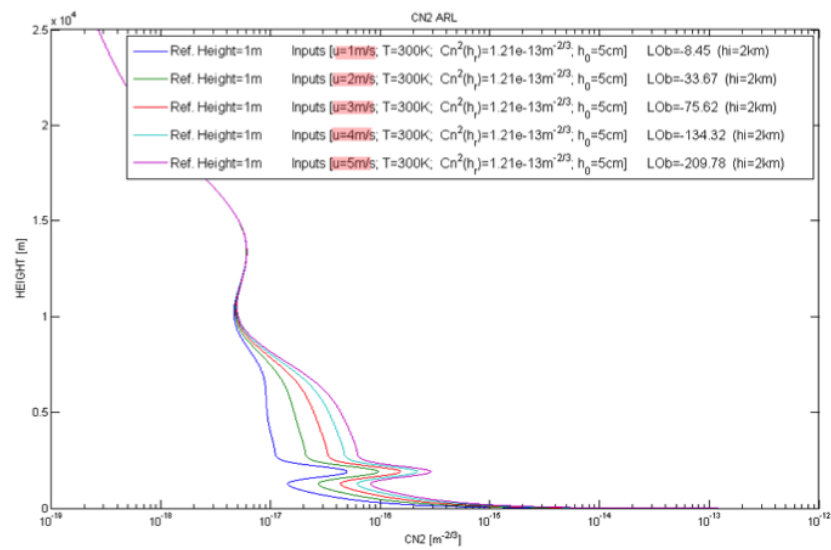
Three main input parameters define the ARL profile model: an estimate of C_n^2 at reference height (h_r) close to the ground, the average air temperature and the average wind speed at the same reference height. Figure 3.4 shows the impact on the profile of the variations of each one of these parameters. A quick overview of these graphs allows one to state that the input temperature may not have such an important effect on the profile generated as compared to the average wind and C_n^2 inputs. Indeed, varying the ground C_n^2 from typical values of about 10^{-12} to 10^{-14} induces significant variations in the profiles up to 10 km. More precisely the peak corresponding to the inversion layer is shifted from about $2 \cdot 10^{-17} m^{-2/3}$ for $C_n^2(h_r) = 1.21 \cdot 10^{-14} m^{-2/3}$ to $5 \cdot 10^{-16} m^{-2/3}$ for $C_n^2(h_r) = 1.21 \cdot 10^{-12} m^{-2/3}$. Varying average ground wind speed inputs from typical values of 1 m/s to 5 m/s induce as well an important variation in the profiles generated up to 10 km. On the other hand different ground temperatures (in the 270-300K range) inputs have almost no effects up to the inversion layer and induce slight differences from the top of the inversion layer up to 10 km ($10^{-16} m^{-2/3}$ to $3 \cdot 10^{-16} m^{-2/3}$).



(a)



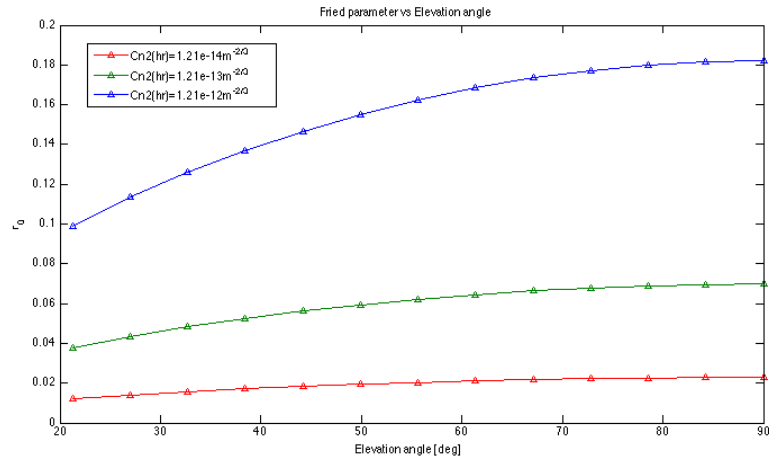
(b)



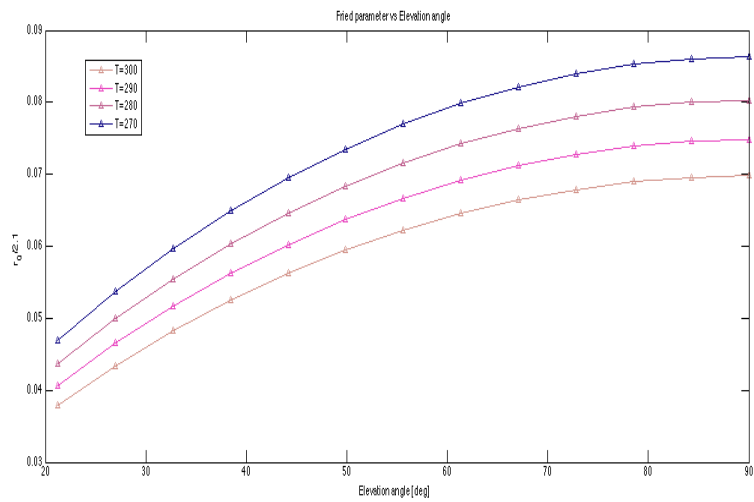
(c)

Figure 3.4: Effect on the ARL profile of the variation of its input parameter; (a) Ground $C_n^2(h_r)$ variations; (b) Air temperature at h_r variations; (c) Average wind velocity at h_r variations

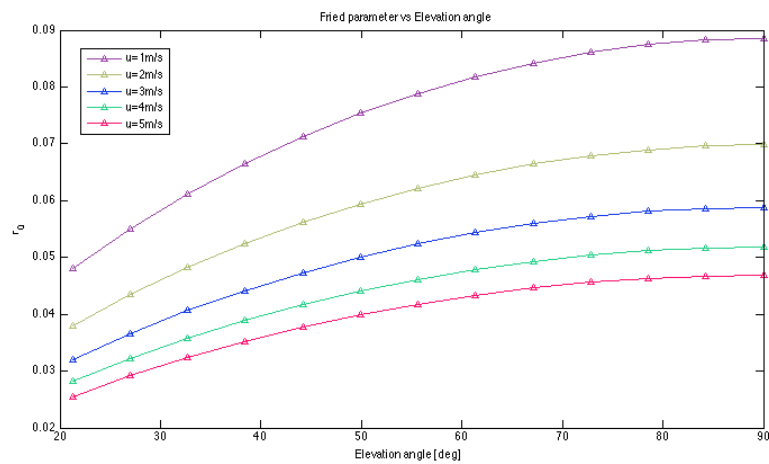
As for the HAP study case, a rigorous and relevant way to highlight such characteristics is achieved by computing the Fried parameter and scintillation index for each variation. Figure 3.5 and figure 3.6 present the computations of the Fried parameters and the scintillation indices for the different input cases. As expected the temperature variations induce roughly negligible difference in the Fried parameter computations (spanning from 0.07 m to 0.085 m at 90° elevation). The wind speed inputs have a sensitive impact, producing r_0 ranging from 0.048 m to almost 0.09 m at 90° elevation whereas $C_n^2(h_r)$ inputs have a considerable effect: the corresponding r_0 span from 0.02 m to 0.18 m. The ARL model presents in the free atmosphere layer (above roughly 10 km) a fixed profile (based on the non-parametric model CLEAR I). This means that whatever the atmospheric conditions close to the ground and in the boundary layer are, the upper atmosphere part is never affected. This constitutes a major flaw of the model especially when one intends to use such a model for other sites than the New Mexico desert. This default is further highlighted by the results of the computations of the scintillation indices corresponding to all the different input cases which have exactly the same evolution with respect to the elevation angle.



(a)

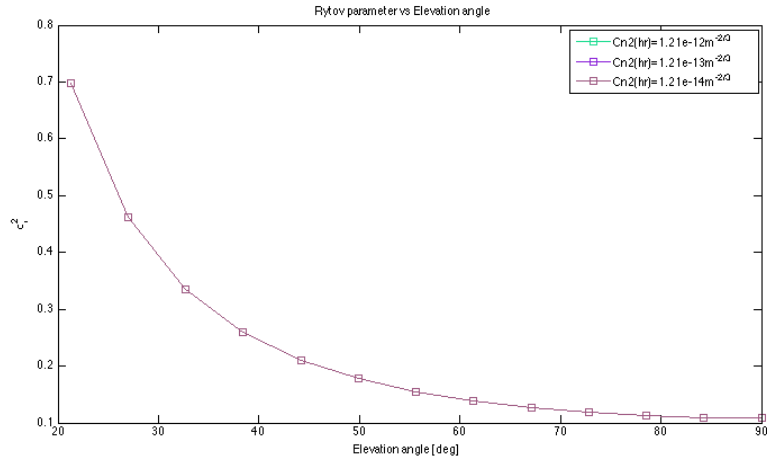


(b)

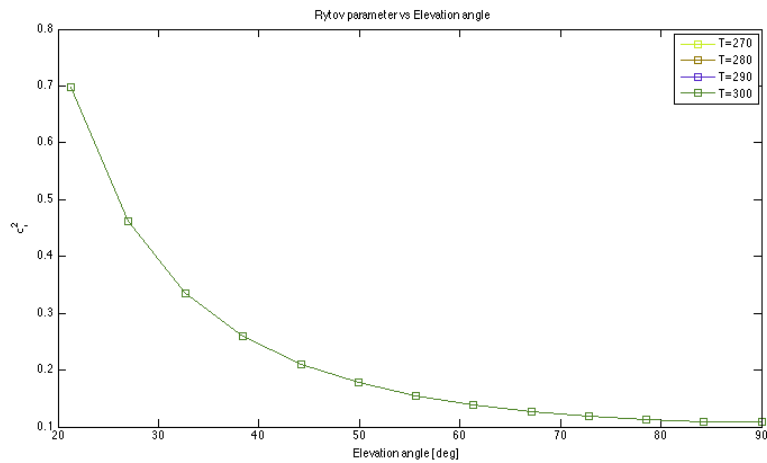


(c)

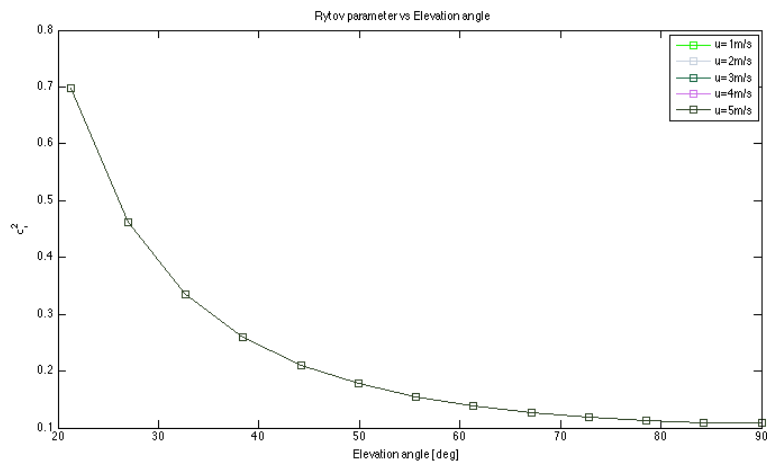
Figure 3.5: Fried parameters computed using the ARL profiles corresponding to different cases of: (a) Different Ground $C_n^2(h_r)$ values; (b) Different air temperature at h_r values ;(c) Different average wind velocity at h_r values



(a)



(b)



(c)

Figure 3.6: Scintillation indices computed using the ARL profiles corresponding to different cases of: (a) Different Ground $C_n^2(h_r)$ values; (b) Different air temperature at h_r values ;(c) Different average wind velocity at h_r values

3.3 Comparison to Radiosondes Data - Izana Observatory

Two main categories of measurement techniques exist to obtain data allowing to infer C_n^2 : remote sensing techniques, such as radar backscatter and optical correlation methods, as opposed to direct point measurements using temperature structure as a tracer for turbulence structure.

The C_n^2 depends on meteorological parameters that are pressure, temperature and humidity. The former one has negligible variations as compared to the latter in the atmosphere. Moreover, optical wavelengths are not sensibly affected by humidity fluctuations and therefore only temperature fluctuations are relevant. A direct relationship exists between C_n^2 and the temperature fluctuations structure constant C_T^2 depending on altitude:

$$C_n^2(h) = \left[\frac{a_d(\lambda)P(h)}{T(h)^2} \times 10^{-6} \right]^2 C_T^2(h) \quad (3.1)$$

where $a_d(\lambda) = 79 \times 10^{-8} K/Pa$ for visible and near-infrared wavelengths. The thermosonde system provides $C_T^2(h)$ data and thus $C_n^2(h)$ data by measuring mean square temperature fluctuations as a function of altitude using the definition of the structure function of the (potential) temperature in the inertial subrange:

$$C_T^2(h) = \langle (T_1 - T_2)^2 \rangle R^{-2/3} \quad (3.2)$$

Hence, using thermosondes (thermal sensor radiosonde), a balloon-borne instrument, one can infer C_n^2 profiles since that the data acquired provide the quantitative link between theory and propagation statistics. The thermosondes are composed of a pair (or more depending on design) of high resolution thermal sensors and the associated electronics that report temperature statistics by telemetry (along with the standard meteorological data: temperature, pressure, humidity, wind speed and direction sensed by the radiosonde) during ascent and/or descent. The sensors are very fine resistance wire probes measuring the root mean square temperature difference across a given horizontal distance in Eq.3.1. The temperature structure constant can then be calculated and therefore C_n^2 as well using Eq.3.2

The main advantage of such a technique resides in the altitude resolution obtained. Scintillometers and some low-resolution radars cannot resolve the narrow layers of turbulence. Balloon-borne instruments possess the highest resolution but measure along a vertical path determined by the wind. Thus, due to the slow ascension of the balloon, this method is not completely adapted to providing the temporal evolution of the turbulence statistical properties. Moreover this technique remains costly since that usually the instruments cannot be retrieved after the measurements. Therefore balloon-borne techniques are adequate for specific site testing but inadapted for long term measurements or real time turbulence estimations.

In 1975, a campaign of C_T^2 profile measurements took place at the observatory of Izana (among other sites). Four launches were performed at Izana. The C_n^2 values at predefined heights corresponding to relevant turbulence layers for astronomical applications were reported. Ground values C_n^2 were given as well. A copy of the original report was available at the DLR site in Oberpfaffenhofen. Figure 3.7 shows, in red, the average of the four experimental profiles that were obtained at approximately the same hour. The green profile corresponds to a modified HV model that takes into account the height above sea level of the ground. The HAP profile is in blue.

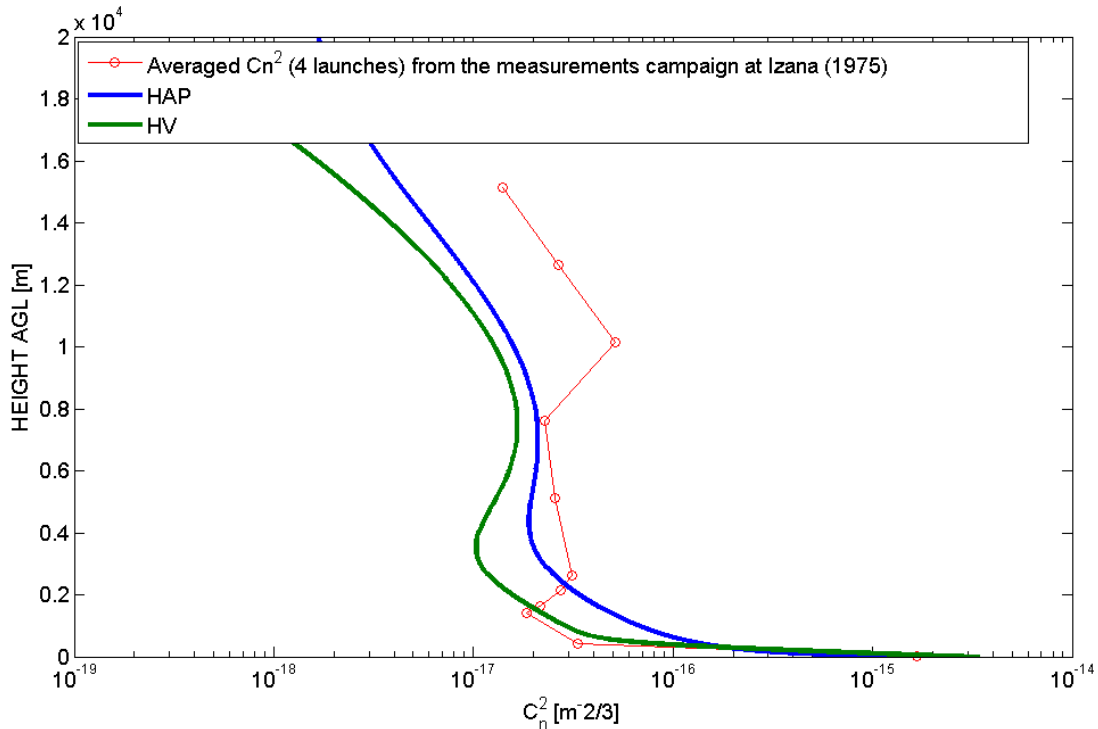
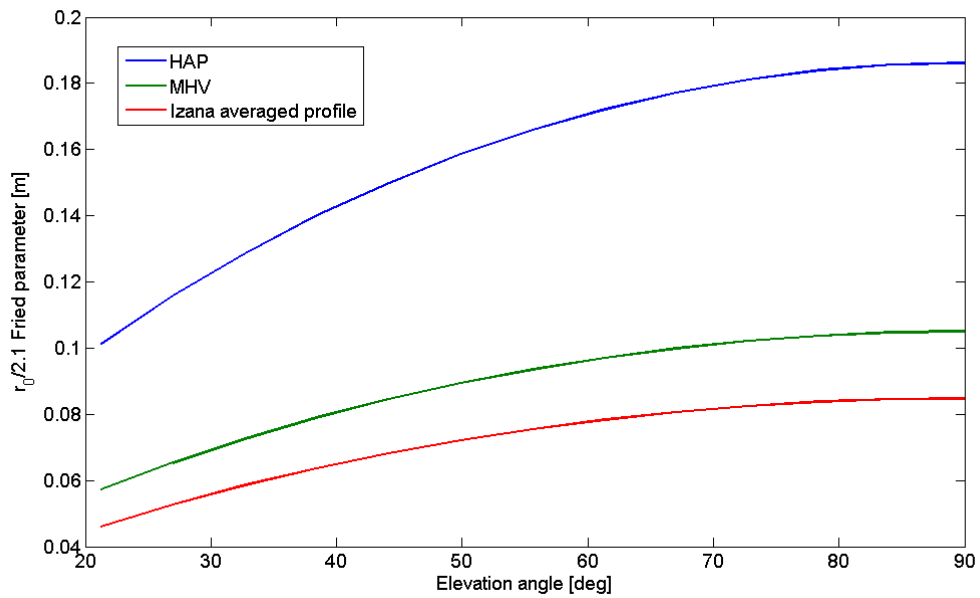
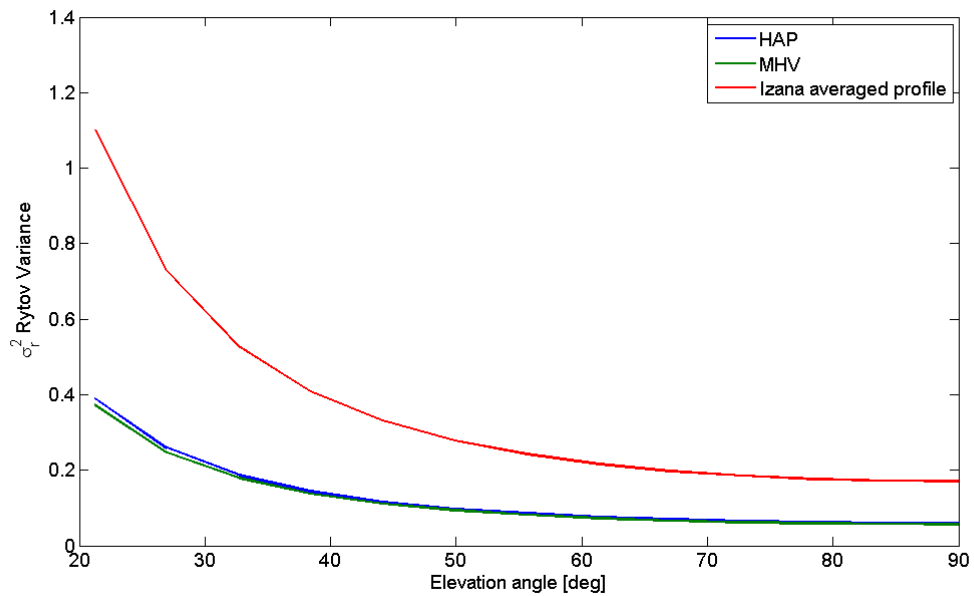


Figure 3.7: Comparison of the HAP profile (in blue) and HV profile (in green) to the experimental data obtained from radiosonde measurements at Izana in 1975 (in red)

In order to assess the performance of the HAP model compared to the HV, the Fried parameters and scintillation indices for different elevation angles are represented on figure 3.8 (a) and (b) respectively. The HAP performs clearly less well than the HV model on the basis of the comparison to the experimental data for the r_0 computations. The SI computations make no significant difference. Nevertheless, it should be noted that due to the fact that very few points characterize the experimental profile near the ground it does not seem rigorous to conclude on that the HV is better suited than the HAP model in that case.



(a)



(b)

Figure 3.8: Fried parameters (a) and scintillation indices (b) computed using the HAP and HV profile corresponding to figure 3.7 and compared to that of the Izana experimental profile

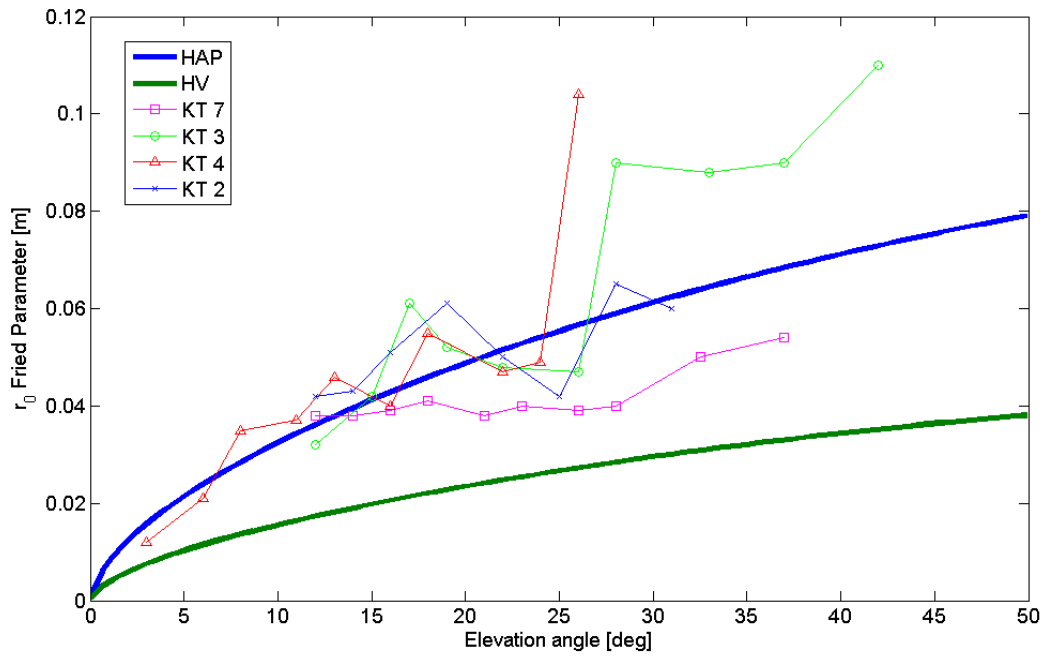
KIODO Trial	Day of June 2006	Time (UTC) of Pass Start	Maximum Pass Elevation	Measurement Elevation Span	Weather	Remark
KT 1	7 th	1:13	45.5°	10 - 35°	90% clear sky, 8°C	No scintillation / DIMM measurement
KT 2	9 th	0:02	33.5°	10 - 32°	90% clear sky, 10°C	No BER measurement
KT 3	14 th	1:04	55.6°	10 - 45°	clear sky, 10°C	
KT 4	15 th	23:54	28.0°	2 - 27°	80% clear sky, 12°C	
KT 5	21 st	0:56	68.2°		Cloudy	No Link
KT 6	23 rd	1:21	38.4°		Cloudy	No Link
KT 7	28 th	0:47	83.2°	4 - 43°	Thunder clouds 1 h before trial, 18°C	
KT 8	30 th	1:12	46.5°		Cloudy	No Link

Table 3.1: Overview of the downlink parameters of the KIODO campaign

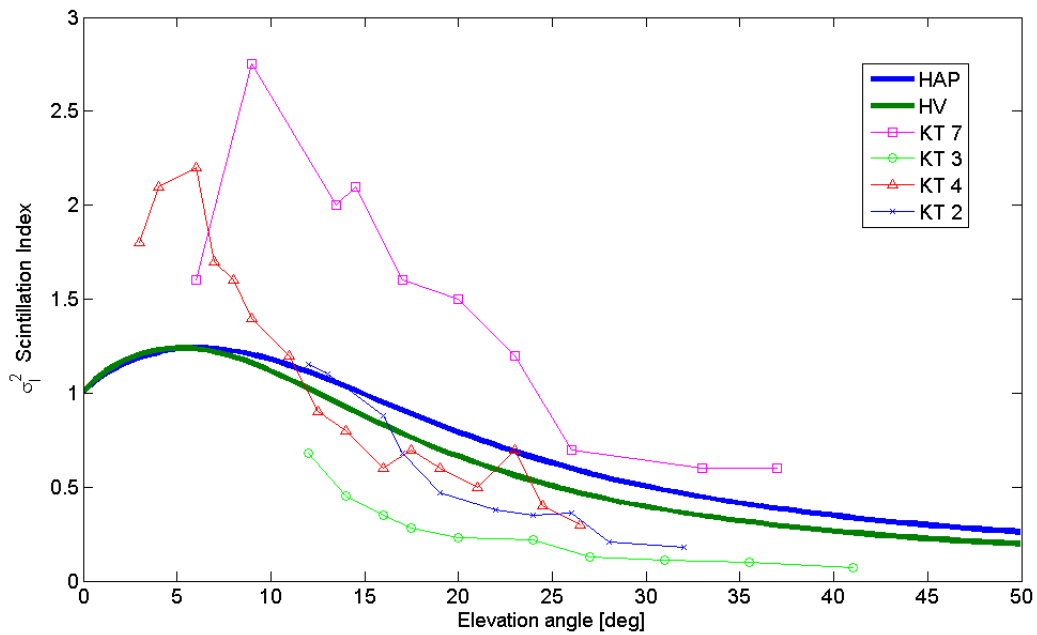
3.4 Comparison to the Results of the Optical Downlink Experiment KIODO

The KIODO (Klrari's Optical Downlink to Oberpfaffenhofen) experiment took place in June 2006. An optical link was established between the OICETS satellite and a DLR ground station located in Oberpfaffenhofen. OICETS is a LEO satellite owned by JAXA with a sun-synchronous orbit and an altitude of 610 km. This was the first optical LEO downlink on European grounds. The ground station received a 50-Mbit/s. Five trials out of eight were successfully performed while the other three were hindered by cloud blockage. The elevation angle above the horizon ranged between 2° and 45°. The Fried parameter and the scintillation index were measured for four of the successful trials for the corresponding elevations reported in table 3.1 along with other parameters relevant to the downlink characteristics.

Figure 3.9 (a) and (b) present, respectively, the Fried parameters and scintillation indices measured during the four trials compared to the ones obtained from the HAP and the HV models. The r_0 evolution with the elevation angle of the satellite obtained from the HAP model is clearly closer to the experimental case than that computed from the HV model.



(a)



(b)

Figure 3.9: Fried parameters (a) and scintillation indices (b) measured during the four trials (KT2, KT3, KT4, KT7) of the KIDO campaign and compared to the ones obtained from the HAP (in blue) and the HV (in green) models

The SI computations are comparable for both models. They seem very far from real values for low elevation angles. It should be noted that the KT7 data are unusually high, probably because of the atmospheric conditions prior to the trial (thunder clouds 1h before trial). Nevertheless, a poor comparison of the SI modeled to the experimental data at low elevations angle was expected. Indeed, the theoretical hypotheses that are weak to moderate turbulence conditions, using the Kolmogorov spectrum (zero inner scale and infinite outer scale) and considering a plane wave, for which the SI is defined (Eq.1.23) bound its maximum value to roughly 1.2. These hypothesis do not hold at low elevation angles for which for instance the turbulence conditions cannot be considered moderate anymore. Using a more realistic turbulence spectrum, including for instance a realistic inner scale parameter could have led to more comparable results. However it would necessitate the identification of an adequate theoretical model of the inner scale. Section 2.4 introduced potential leads for the development of such models.

3.5 HAP Model - A functional implementation

3.5.1 Overview

Although some features of the HAP model still need to be studied further, for instance the range of validity of the power parameter empirical relationship, and confronted to more experimental data, it seemed interesting to provide at the end of this work a method to readily use it in practice. For rendering it practical, the challenge resides in providing a simple and straightforward way to infer its input parameters. These latter are the power law parameter p , given by Andrews empirical relationship (Eq. 2.9); the value of C_n^2 near the ground; and the random background parameter M . Figure 3.10 presents a diagram summarizing the inputs to the model and the means to potentially infer them.

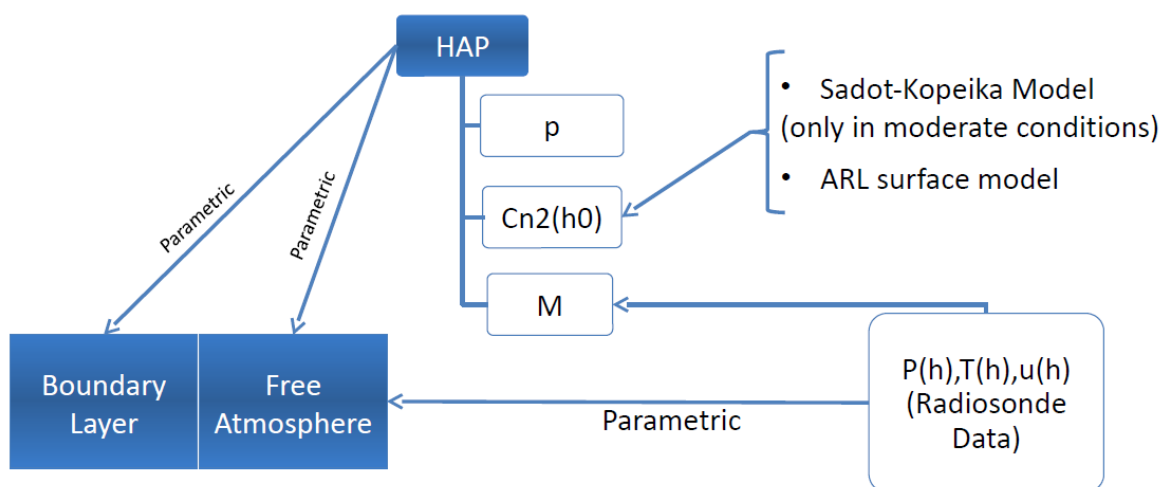


Figure 3.10: Overview diagram of potential practical implementation of the HAP model

3.5.2 Ground-level C_n^2 Estimation

The $C_n^2(h_0)$ value near the ground needs to be inferred in the simplest way possible. It also needs to be as precise as possible given the excursions one can find in the computed profiles for slightly different $C_n^2(h_0)$. The most reliable way to do so seems to be using the Sadot-Kopeika model described in section 2.2.7. This model has been tested in various conditions and in various sites and gave very good agreement with experimental data. Its input parameters are simple meteorological parameters at the considered height such as air temperature, relative humidity, wind speed, in its simplest version. A more complete version includes as well the effect of solar flux and the total cross-sectional area of particles per cubic meter. Each one of these parameters can be measured precisely with quite standard equipments. However the model is valid in moderate conditions (9 to 35°C, relative humidity from 14 to 92%, and wind speed dynamic range between 0 and 10 m/s). An alternative would be to consider using a MOST based model such as the one used in the surface layer profile of the ARL model. Instead of using the iterative process described in section 2.2.3.1, one could try to directly infer the scaling potential temperature, hence allowing for the direct computation of the Monin-Obukhov length. Several methods exist in boundary layer meteorology to do so (e.g. [43]).

3.5.3 Random background turbulence estimation (HAP)

The random background turbulence is a term that has apparently been coined by Andrews et al since no definitions or equivalent of it were found in the literature. However analysing radiosonde data over an year from the radiosonde station of München-Oberschleissheim (WMO: 10868) north of Munich, lead to the conclusion that the mathematical introduction of such a parameter in the profile model was justified. Radiosonde data were acquired using NOAA RAOB database website (<http://esrl.noaa.gov/raobs/>). The station performs launches at 00Z, 12Z and some times 18Z. The sounding data comprises primarily pressure, altitude and temperature readings. The readings are done predefined arbitrary pressure level. Therefore from one launch to another a pressure level does not correspond to the same altitude. Wind speed is also given but for fewer levels. Because each set of data by launch had few readings, it was decided to concatenate all the data sets by month. This provided average monthly pressure and temperature profiles with a high resolution for daytime conditions (12Z data) and nighttime conditions (00Z). Obtaining C_n^2 profiles from there can be done with the subsequent reasoning. Tatarskii provided us with the following relationship [33]

$$C_n^2 = 2.8L_0(h)^{4/3}M(h)^2 \quad (3.3)$$

where M is the potential refractive index and L_0 the outer scale. The models used for the outer scale profile are the ones described in section 2.4.2. The potential refractive index was approximated by:

$$M(h) = \frac{-77.6 \times 10^{-6} \times P(h)N(h)}{gT(h)} \quad (3.4)$$

with g the standard gravity constant, $P(h)$ and $T(h)$ the pressure and temperature profiles. $N(h)$ is called the Brunt-Vaisala frequency [22] and is given by

$$N(h) = \frac{g}{\theta(h)} \frac{d\theta}{dh} \quad (3.5)$$

$\theta(h)$ is the potential temperature profile given by:

$$\theta(h) = \left(\frac{p_0}{P(h)} \right)^k \quad (3.6)$$

where p_0 is the standard pressure typically 100 kPa, and k is the Poisson constant, often assumed to be $2/7$, the ratio of the gas constant to the specific heat capacity at constant pressure for an ideal diatomic gas. Once monthly C_n^2 profiles were obtained, they were fitted with HAP profiles using a least mean square method for values of the random background turbulence parameter M spanning from $M = 1$ to $M = 5$; the power law parameter was computed by considering monthly average sunset and sunrise times, the ground $C_n^2(h_0)$ was computed using the radiosonde data which always provided pressure and temperature ground values.

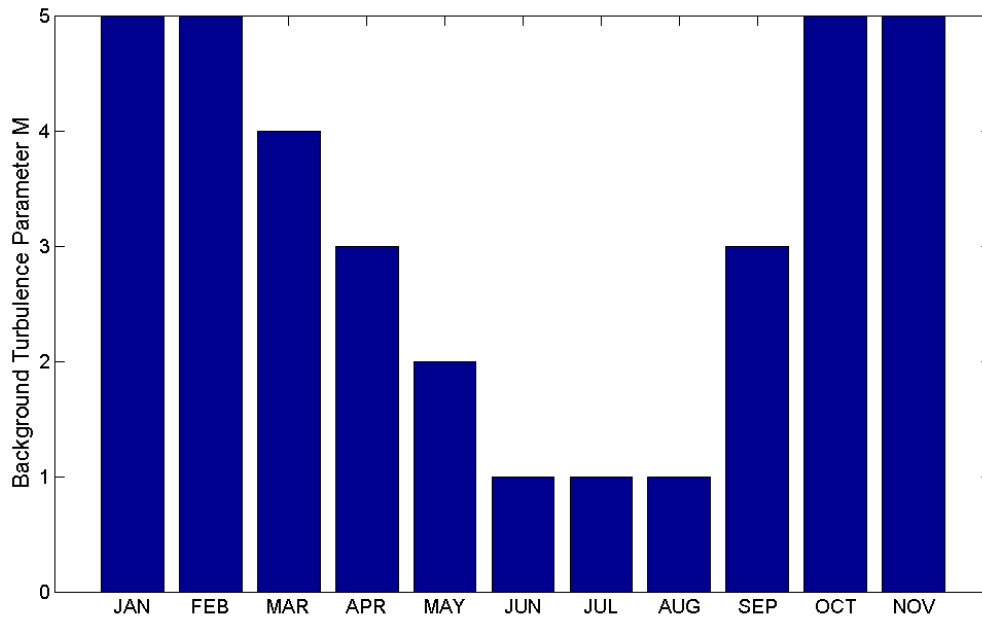


Figure 3.11: Monthly distribution of the random background turbulence parameter M obtained from a LMS fit of the HAP model to radiosonde data gathered over one year. Daytime data (12Z launches).

Figure 3.11 represents the distribution of M over an year for the daytime data. A clear seasonal trend appears: the random background turbulence is greater in winter than in

summer. The parameter M seems to be related to the evolution of a background level of wind at moderate to high altitudes. This evolution seems to correspond to the polar jet stream trends. It is said to "follow the sun" i.e. as the sun's elevation increases each day in the spring, the average latitude of the jet stream shifts poleward. As autumn approaches and the sun's elevation decreases, the jet stream's average latitude moves toward the equator. Moreover jet stream winds either increases as the jet lowers or decreases as the jet rises [44]. A similar trend was not observed for the nighttime data. The monthly distribution of M seemed completely random. Nevertheless, this method could constitute a simple way to infer M as an input parameter for the HAP model. Analyzing the radiosonde data over several years could be a track to deepen.

CONCLUSION

The main objective of this thesis was to set the theoretical framework of turbulence modeling and lend the first elements for an assessment of the most relevant refractive index structure constant profiles models in the framework of satellite to ground optical communications. Therefore the following tasks were completed:

- Bibliographic work on the profile modeling of the C_n^2 parameter, inner and outer scale. The status quo of the available models has therefore been established.
- Comparison of the selected models with respect to their applicability, realism, accuracy and needed input parameters. An overview table was established providing input parameter and relevant modeling equations for each profile. A technical note was redacted for DLR at the end of this step.
- After pre-selection of two relevant models the Fried parameter and the scintillation index were computed and compared to experimental data. The results were discussed and led to the selection of the HAP model as the most suited one.
- Analyzing rawinsonde data gathered over an year at the station of München-Oberschleissheim highlighted the potential correlation between the random background turbulence parameter M (input to the HAP model) and the seasonal trends of the polar jet-stream. With the estimation of the C_n^2 value at the ground level by means of the Sadot-Kopeika model, a practical implementation of the HAP model was given

Because the aim of the work undertaken was mainly to establish the status quo of the modeling options for the C_n^2 and characteristic scales profiles, the steps that can be performed as future work following this thesis would mainly involve the experimental testing of the relevance of the HAP model. Indeed, the confrontation to experimental data presented here could be deepened. Additional channel parameters could be computed as for instance the intensity correlation width and isoplanatic angle. The latter is particularly for the design of adaptive optics, it is the angular distance (from a reference such as a guide star) over which atmospheric turbulence is essentially unchanged. The former describes the average speckle (i.e. intensity pattern produced by the mutual interference of the distorted propagating wavefronts) size in the pupil plane of the receiver. If the receiver aperture is larger than the correlation width, some aperture averaging is likely to occur. On the other hand, the receiver acts like a "point receiver" when its aperture size is comparable to or smaller than the correlation width of intensity fluctuations. The computations of the scintillation index in the present report were done considering a point receiver.

Obviously, the data from KIODO were obtained with a finite aperture receiver. Therefore for a more rigorous comparison one could use a more realistic model of the scintillation index. One could consider as well using a more realistic turbulence spectrum (including the effect of characteristic scales) making the results more comparable to the data at low elevation angles.

BIBLIOGRAPHY

- [1] C. Valley. Isoplanatic degradation of tilt correction and short-term imaging systems. *Opt. Soc. of Am.*, 19(4), 1980.
- [2] R.E. Hufnagel. Propagation through atmospheric turbulence. In *The Infrared Handbook*, chapter 6. USGPO, 1974.
- [3] Arun K. Majumdar. Free-space laser communication performance in the atmospheric channel. In *Free-Space Laser Communications Principles and Advances*. Springer, 2008.
- [4] Sean G. O'Brien David H. Tofsted and Gail T. Vaucher. An atmospheric turbulence profile model for use in army wargaming applications i. Technical report, Army Research Laboratory, The address of the publisher, 2006.
- [5] R. Crabbs D. Wayne T. Leclerc L.C. Andrews, R.L. Phillips and P. Sauer. Creating a cn_2 profile as a function of altitude using scintillation measurements along a slant path. *Proc. of SPIE*, 2012.
- [6] D. Wayne T. Leclerc P.Sauer R. Crabbs L.C. Andrews, R.L. Phillips and J. Kiriazes. Near-ground vertical profile of refractive-index fluctuations. *Proc. of SPIE*, (2), 2009.
- [7] R. Crabbs T. Leclerc L.C. Andrews, R.L. Phillips and P. Sauer. Channel characterization for free space optical communications. Technical Report 2, UCF DARPA Project ID: 66016010, 2012.
- [8] R. Crabbs D. Wayne T. Leclerc L.C. Andrews, R.L. Phillips and P. Sauer. Atmospheric channel characterization for orca testing at ntr. *Proc. of SPIE*, 2010.
- [9] J.M. Warnock and T.E. VanZandt. A statistical model to estimate the refractivity turbulence structure constant cn_2 in the free atmosphere. Technical report, National Oceanic and Atmospheric Administration, 1985.
- [10] K.S. Gage T.E. VanZandt, J.L. Green and W.L. Clark. Vertical profiles of refractivity turbulence structure constant: comparison of observations by the sunset radar with a new theoretical model. *Radio Science*, 13(5):819–829, 1978.
- [11] R. Beland E.M. Dewan, R.E. Good and J. Brown. A model for cn_2 (optical turbulence) profiles using radiosonde data. Technical report, Phillips Laboratory Directorate of Geophysics US Air Force, Hanscom Air Force Base, MA 01731-3010, 1993.
- [12] Frank D. Eaton Jennifer C. Ricklin, Stephen M. Hammel and Svetlana L. Lachinova. Atmospheric channel effects on free-space laser communication. In *Free-Space Laser Communications Principles and Advances*. Springer, 2008.

- [13] F. Eaton C. Gilbreath S. Doss-Hammel C. Moore J. Murphy Y. Han Oh M. Stell Eun Oh, J. Ricklin. Estimating optical turbulence using the pamela model. *Proc. of SPIE*, 2004.
- [14] Eun Oh S. Doss-Hammel-F. Eaton Y. Han Oh, J. Ricklin. Estimating optical turbulence effects on free space laser communication: modeling and measurements at arl s alot facility. *Proc. of SPIE*, 2004.
- [15] N.S. Kopeika D. Sadot. Forecasting optical turbulence strength on the basis of macriscale meteorology and aerosols: models and validation. *Opticla Engineering*, 31(2), 1992.
- [16] N. S. Kopeika S. Bendersky and N. Blaunstein. Atmospheric optical turbulence over land in middle east coastal environments: prediction modeling and measurements. *Optical society of America*, 43(20), 2004.
- [17] Ronald R. Parenti and Richard J. Sasiela. Laserguide-star systems for astronomical applications. *J. Opt. Soc. Am.*, 11(1), 1994.
- [18] D.P. Greenwood. Bandwidth specification for adaptive optics systems. *Optical Society of America*, 67(3), 1977.
- [19] E. Ryznar and J.A. Bartlo. Dependence of $cn^2(ct^2)$ in the atmospheric boundary layer on cenventional meteorological variables. Technical report, Air Force Geophysics Laboratory Air Force Systems Command US Air Force, Hanscom Air Force Base, MA 01731-3010, 1986.
- [20] V.L. Mironov A.S. Gurvich, A.I. Kon and S.S. Khmelevtsov. *Lazernoe Izluchenie v Turbulentnoi Atmodfere (Laser Radiation in a turbulent atmosphere)*. SSSR Intstitut of the Physics of the Atmosphere, 1976.
- [21] E.A. Murphy J.H. Brown R.E Good, R.R. Beland and E.M. Dewan. Atmospheric models of optical turbulence. *SPIE*, 1988.
- [22] R.R. Beland. Propagation through atmospheric optical turbulence. In Frederick G. Smith, editor, *Atmospheric Propagation of Radiation- The IF/EO Systems Handbook*, volume 2, chapter 2. SPIE Press and ERIM, 1993.
- [23] Larry C. Andrews and Ronald L. Phillips. *Laser Beam Propagation through Random Media*. SPIE Press, 2005.
- [24] D. L. Walters and K. E. Kunkel. Atmospheric modulation transfer function for desert and mountain locations: the atmospheric effects on r_0 . *J. Opt. Soc. Am.*, (71):397–405, 1981.
- [25] L. F. Richardson. *Weather Prediction by Numerical Process*. Cambridge Mathematical library, 2007.
- [26] L.C. Andrews. An analytical model for the refractive index power spectrum and its application to optical scintillations in the atmosphere. *J. Mod. Opt.*, (39):1849–1853, 1992.
- [27] J. C. LaRue F. H. Champagne, C. A. Friehe and J. C. Wyngaard. Flux measurements, flux-estimation techniques, and fine-scale turbulence measurements in the unstable surface layer over land. *J. Atmosp. Sci.*, (34):515–530, 1977.

- [28] R. M. Williams and C. A. Paulson. Microscale temperature and velocity spectra in the atmospheric boundary layer boundary layer. *J. Fluid Mech.*, (83):547–567, 1977.
- [29] D. A. Haugen-O. R. Cote J. C. Kaimal, J. C. Wyngaard and Y. Izumi. Turbulence structure in the convective boundary layer. *Journal of the Atmospheric Sciences*, 1976.
- [30] R. R. Beland and J. H. Brown. Optical turbulence measurements in jet streams. *Annual Review Conf. on Atmospheric Transmission Models*, 1987.
- [31] J. W. Hardy. *Adaptive optics for astronomical telescopes*. NY Oxford University Press, 1998.
- [32] John C. Wyngaard. *On Surface Layer Turbulence in Workshop on Microceteorology*. American Meteorological society, 1973.
- [33] V.I. Tatarskii. *The effects of the turbulent atmosphere on wave propagation*. Israel Program for Scientific Translations Ltd, 1971.
- [34] E.M. Dewan and R.E. Good. Saturation and the universal spectrum for vertical profiles of horizontal scalar winds in the atmosphere. *J. Geophys. Res.*, (3), 1986.
- [35] Reginald J Hill. Review of optical scintillation methods of measuring the refractive-index spectrum, inner scale and surface fluxes. In Frederick G. Smith, editor, *Waves in Random Media 2*, chapter 2:3, pages 179–201. Taylor and Francis, 1992.
- [36] A. Consortini et. al.i. Measuring inner scale of atmospheric turbulence by angle of arrival and scintillation. *Elsevier Science B. V.*, 2002.
- [37] G.R. Ochs and R.J. Hill. Optical-scintillation method of measuring turbulence inner scale. *Applied Optics*, 24(15), 1985.
- [38] F.D. Eaton and G.D. Nastrom. Preliminary estimates of the vertical profiles of inner and outer scales from white sands missile range, new mexico, vhf radar observations. *Radio Science*, 33(4):895–903, 1998.
- [39] R.R. Beland and J.H. Brown. A deterministic temperature model for stratospheric optical trubulence. *Physica Scripta*, 1988.
- [40] C.E. Coulman et. al. Outer scale of turbulence appropriate to modeling refractive-index structure profiles. *Applied Optics*, 27(1), 1988.
- [41] A. Abahamid et. al. Optical turbulence modeling in the boundary layer and free atmosphere using instrumented meteorological balloons. *Astronomy and Astrophysics*, 2003.
- [42] J. Barat and F. Bertin. Simultaneous measurements of temperature and velocity fluctuation within clear air turbulence layers: analysis of the estimate of dissipation rate by remote sensing techniques. *American Meteorological Society*, 1984.
- [43] J.F. Louis. A parametric model of vertical eddy fluxes in the atmosphere. *Boundary Layer Meteorology*, (17):187–202, 1979.
- [44] C.L. Archer and K. Caldeira. Historical trends in the jet streams. *Geophysical research letters*, (35), 2008.